ANISOTROPIC INTERMOLECULAR FORCES IN RARE GAS - HYDROGEN HALIDE SYSTEMS

Jeremy M. Hutson

A thesis submitted for the degree of
Doctor of Philosophy
in the University of Oxford

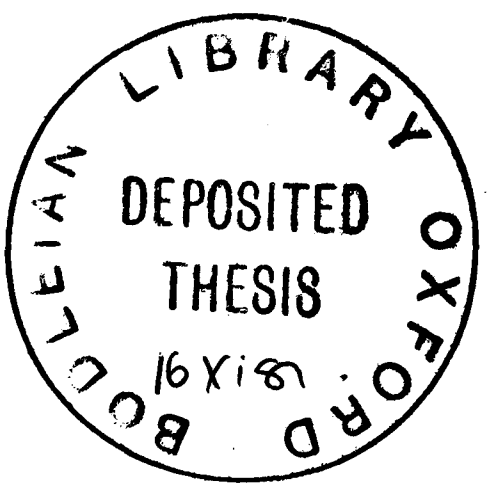

Hertford College

Trinity Term 1981

ANISOTROPIC INTERMOLECULAR FORCES IN RARE GAS - HYDROGEN HALIDE SYSTEMS

Abstract of a thesis submitted for the degree of
Doctor of Philosophy in the University of Oxford

Jeremy M. Hutson
Hertford College
Trinity Term 1981

The thesis is concerned with the derivation of anisotropic intermolecular potentials from experimental data. For the rare gas - hydrogen halide systems the most useful experimental results are those from molecular beam rotational spectra of van der Waals complexes and from pressure broadening of hydrogen halide rotational spectra by rare gases. Intermolecular potentials for the Ar.HCl system had previously been obtained from each of these experiments separately, but none of the potentials proposed succeeded in reproducing all the available data.

In the present work, improved theoretical methods are developed for the calculation of molecular beam spectra and line broadening cross sections from a proposed intermolecular potential. The methods developed are substantially faster than those previously available, allowing their use in a least squares procedure to determine potential parameters. Several possible parameterisations of the intermolecular potential are then considered for Ar.HCl, and least squares fits of potential parameters to experimental results are performed for this system. Measurements of total differential cross sections and second virial coefficients are included in the least squares fits, in addition to the experiments mentioned above. The experimental data demonstrate conclusively that the equilibrium geometry of Ar.HCl is linear, with the atomic arrangement as written. The equilibrium intermolecular distance is 400±3 pm, with an absolute well depth of 180±10 cm^{-1}. The only feature of the potential which is not well determined by the experimental results is the behaviour around the linear Ar.Cl-H geometry.

The results for Ar.HCl are then extended to the systems Ne.HCl, Kr.HCl and Xe.HCl, allowing the dependence of the intermolecular potential on the rare gas to be considered. The molecular beam spectra for Ne.HCl can be fitted only by a potential with a secondary minimum at the linear Ne.Cl-H geometry, in addition to the primary minimum at the linear Ne.H-Cl geometry. The experimental results for the other rare gas - HCl systems are not very sensitive to this feature of the potential, and the potentials for these are constrained to be similar to that for Ne.HCl in this region. The potential surfaces for all the rare gas - HCl systems have similar shapes, and appear to be nearly conformal.

Finally, intermolecular potentials are obtained for the systems Ar.HF, Kr.HF and Xe.HF from molecular beam spectra. The experimental data for these systems are less extensive than for the HCl systems, and the potentials obtained are reliable only in the region of the absolute minimum. The HF systems are considerably more anisotropic than the HCl systems, and it is suggested that this is principally due to greater induction forces in the HF systems. Experiments are suggested which would provide further information on the intermolecular potentials for both HF and HCl systems, and predictions of the results are made using the current best fit potentials.

Acknowledgements

I should like to thank Brian Howard for sowing the seeds from which this thesis grew, and for his constant interest and advice throughout the last three years. I have also learnt much from the other members of the group, particularly Colin Western and Jeremy Frey, who battled with me against the computer. James Prout let me badger him into getting experimental results for Ne.HCl, which helped enormously.

I should like to thank Prof. M. Shapiro and Dr. G.G. Balint-Kurti for providing me with their program for performing artificial channel calculations, and Dr. F.A. Baiocchi for supplying his experimental results on the Xe.HF complex in advance of publication. I have also benefitted from discussions with many other people, notably Mark Child, Chris Ashton and Robert Le Roy.

Finally, I should like to thank Mrs. M. Palmer for her excellent typing, and Chris and Helen for operating the bring-to.

CONTENTS

CHAPTER 1

INTRODUCTION

CHAPTER 1

INTRODUCTION

A knowledge of intermolecular forces is important in many areas of chemistry. The physical properties of solids, liquids and dense gases depend sensitively on the intermolecular forces involved, and such forces are also important in the early stages of chemical reactions. However, although much is known about intermolecular forces in isotropic systems such as the rare gas atom pairs, reliable anisotropic intermolecular potentials are available for very few systems.

The purpose of the present work is to investigate intermolecular forces in atom-diatom systems, which provide the simplest examples of anisotropic interactions. In particular, anisotropic potentials will be obtained for several rare gas - hydrogen halide systems, using all available experimental information. The most detailed information on the potential energy surfaces is obtained from molecular beam spectra of van der Waals complexes, but information from gas imperfections, rotational relaxation phenomena and molecular beam scattering is also included where available. The rare gas - hydrogen halide systems are much more anisotropic than the rare gas - H_2 systems investigated by Le Roy et al. [1], but it is shown that the bonding in these systems can be adequately explained without invoking incipient chemical bonding as suggested by Klemperer [2].

Before proceeding to the methods used to determine potential energy surfaces in the present study, a brief review of previous work in the field will be given. More comprehensive descriptions can be found in a recent book on intermolecular forces by Maitland et al. [3], and in reviews by Le Roy and Carley [4]and Loesch [5] on methods for determining anisotropic intermolecular forces.

1.1 Isotropic systems

Experimental information on van der Waals forces between atoms has been available for a long time, and reliable potential curves are now available for many systems. The earliest attempts to determine such potentials made use of deviations from ideal behaviour in gases; in particular, the second virial coefficient B(T), defined by

$$\frac{P}{nRT} = 1 + nB(T) + n^2C(T) + \ldots$$

is related to the intermolecular pair potential V(R) by the expression

$$B(T) = 2\pi N \int_0^\infty [1 - \exp(-V(R)/k_BT)]\ R^2\ dR$$

where N is the Avogadro number and k_B is the Boltzmann constant. At low temperatures the second virial coefficients are determined mainly by the potential well, and at high temperatures by the excluded volume (i.e. by the repulsive well of the potential). Methods for the direct inversion of second virial coefficients to obtain potential curves have recently been developed [6], although these require high quality experimental information over a wide temperature range.

Gas transport properties, particularly viscosities, have also been used extensively as a source of information on intermolecular potentials. At high temperatures, viscosities are again sensitive to the repulsive wall of the potential, but at low temperatures they are dominated by the long range attractive region. Methods for the direct inversion of viscosity measurements are available [7], and work well for simulated data. As for second virial coefficients, however, the potential recovered is very sensitive to systematic errors in the experimental data, so that very high

quality data are required to obtain a reliable potential curve.

Molecular beam scattering results have also provided a rich source of information on intermolecular forces. If fully resolved differential cross sections are observed, showing both rainbow and diffraction oscillations, it is possible to recover the potential by direct inversion [8], and an iterative inversion method is sometimes also feasible when there are no rainbow oscillations [9]. Potentials obtained from inversion of differential cross sections are less susceptible to systematic errors than those obtained from measurements of thermophysical properties, since potential information is extracted from the structure of the differential cross sections rather than from exact numerical values of gas phase properties.

Differential cross sections at a resolution high enough to permit direct inversion are available for only a few systems; more commonly, rainbow oscillations are resolved but the fast diffraction oscillations are not. Under these circumstances, limited information on the potential is still available, and is usually obtained by fitting the parameters of an assumed potential form to the experimental data. To a first approximation, the rainbow angle determines the well depth ε, while the positions of supernumary rainbows determine the position of the minimum R_m. Useful information is also available from glory oscillations in the integral cross sections, which allow the product εR_m to be determined.

Spectroscopic information has long been an important source of information on potential curves for chemically bound diatomic molecules, and has recently been applied to intermolecular potentials also. The van der Waals well between a pair of atoms is almost invariably deep enough to support bound vibrational states, and vibrational and

rotational spectroscopic constants for these bound states may be inverted to yield a potential curve using the RKR method [10]. This is probably the most reliable method of obtaining intermolecular potentials for atom-atom systems, but at present it is limited by the lack of experimental data. The only rare gas dimer for which such rotationally resolved spectra are available is Ar_2 [11]; however, high quality data on other rare gas pairs are likely to become available over the next few years. If only vibrational levels are resolved, as is the case at present for Kr_2 and Xe_2, one of the RKR equations may still be applied to obtain the well width as a function of energy, and this provides a useful constraint in interpreting other experimental data [12].

Ab initio calculations of intermolecular forces have not yet achieved accuracy comparable with experimental determinations, except for systems of very few electrons, such as $He \cdot H_2$ [13]. The method usually used is the "supermolecule" approach, in which the total energy of the separated molecules is compared with the energy of the "supermolecule" formed by the interacting species at a finite separation. This method has three major drawbacks:

1) The intermolecular energy is very small compared to the total electronic energy, except in the strongly repulsive region , so that small errors in the individual total energies can have a large effect on the calculated energy of interaction.

2) The calculated interaction energy is often very strongly dependent on the basis set used for the calculations, since the basis functions required to describe the wavefunction of the supermolecule are not necessarily the same as those needed for the component monomers. "Basis set superposition error" arises when orbitals on one submolecule compensate for deficiencies in the basis set of the

other, giving an anomalously low energy for the supermolecule and a correspondingly large binding energy. Conversely, "basis set truncation error" arises when basis functions necessary to describe the intermolecular interaction are absent from the basis sets used for the monomers. Both these sources of error may be reduced using the counterpoise method [14], but they are still a major source of inaccuracy.

3) Attractive intermolecular forces are dominated by dispersion forces, which do not appear in self-consistent field (SCF) calculations. Extensive configuration interaction is required to account for the dispersion forces accurately, and this is computationally very expensive.

The supermolecule approach is thus not adequate except for systems of very few electrons or in the highly repulsive region of the potential.

More success has been achieved with perturbative methods for very long range and very short range forces, but such methods are generally not adequate in the region of the potential well. Semiempirical methods have been very successful in calculating the coefficients of the long range attractive terms in atom-atom potentials. Long range C_6 coefficients, for example, may be accurately estimated using sum rules for dipole oscillator strengths [15], and similar methods have also been applied to C_8 and C_{10} coefficients [16]. One semiempirical approach which has proved very useful is to represent the potential as the sum of an SCF repulsion and a damped dispersion series [17], modelling the higher order dispersion and exchange forces on the known behaviour in the $^3\Sigma_u^+$ state of the H_2. Douketis et al. [18] have obtained excellent results for several rare gas pairs using this approach, and similar methods have recently been applied to the weakly anisotropic rare gas -

H_2 systems [19]. However, no success has yet been achieved for more strongly anisotropic systems of the type considered here.

1.2 Anisotropic systems

As seen in the last section, theoretical methods for determining isotropic intermolecular forces from experimental data are well developed, although many direct inversion methods require data better than are currently available. For anisotropic systems, however, the situation is much less satisfactory, from the point of view of both experimental results and theoretical methods.

1.2.1 Thermophysical properties

For anisotropic systems, thermophysical properties do not provide enough information to determine the complete potential surface, although it is still possible to recover an effective isotropic potential from the experimental results. Smith et al. [20] have inverted simulated second virial coefficients, viscosities and self-diffusion data for a model anisotropic potential resembling $N_2 \cdot N_2$, and recovered an effective isotropic potential which was about 15% deeper than the true spherically averaged potential. The potentials recovered from the three different properties studied were strikingly similar, raising the interesting possibility of an effective isotropic potential capable of reproducing a wide range of thermophysical properties. Further work is required to establish in what way this effective potential curve is related to the full anisotropic potential surface.

1.2.2 Molecular beam scattering

In the case of molecular beam scattering results, the presence of anisotropy tends to damp out rainbow and diffraction oscillations in the

total differential cross sections [21], so that it is difficult to obtain even an effective isotropic potential with any accuracy; it is not possible to obtain quantitative information on the potential anisotropy from total differential cross section data [22]. Fully resolved state-to-state inelastic differential cross sections would contain the necessary information, but are not yet experimentally accessible for most systems, and are also very difficult to invert. Gerber et al. [23] have recently proposed a direct inversion method for state-to-state cross sections, but their method assumes a two state model and uses the exponential distorted wave approximation, so that it is applicable only to systems in which the inelastic scattering is weak and the rotational energy spacing is large. The method has been used to obtain an anisotropic intermolecular potential for $Ne \cdot D_2$ [24], but for more strongly anisotropic systems, such as those containing the hydrogen halides, neither the experiment nor the inversion procedure is feasible, so that it seems unlikely that differential cross section results will provide reliable potential energy surfaces for such systems in the immediate future.

Useful information has also been obtained from integral cross sections for anisotropic systems. Zandee and Reuss [25] have investigated integral cross sections for scattering of oriented H_2 molecules by rare gas atoms: ortho-hydrogen in the $j = 1$ state was state-selected using an inhomogeneous magnetic field, and the difference in integral cross sections for molecules in the $m = 0$ and $m = 1$ states was measured. Experiments were carried out over a range of collision energies, allowing information to be extracted on the anisotropy at both long and short range. Similar work has been reported for the rare gas - NO systems, using electrostatic state selection [26], but extension of the method to

molecules whose rotational ground state is nondegenerate is likely to be difficult.

1.2.3 Rotational relaxation phenomena

Although high quality molecular beam measurements of inelastic processes are very difficult to obtain, there are a number of experiments which measure rotationally inelastic collisions in bulk gases. Some of the most important of these are

1) Pressure broadening and shifting of spectroscopic lines

2) NMR spin-lattice and spin-spin relaxation times

3) Sound absorption measurements.

These effects depend sensitively on the anisotropy of the intermolecular potential, and are zero for isotropic potentials, so that they are well suited to determining potential anisotropies. The exact quantum mechanical calculation of rotational relaxation phenomena for a proposed potential surface is computationally very expensive [27], but progress has recently been made with approximate methods [28]; these will be discussed in more detail in chapter 2.

Rotational relaxation phenomena in atom-diatom systems provide information mainly on the anisotropy of the repulsive wall of the intermolecular potential. Schafer and Gordon [27] have used experimental results of this type to determine a potential surface for the $He \cdot H_2$ system, where the potential well is very shallow. However, as will be seen in chapter 3, Ar·HCl potentials obtained from relaxation data alone were seriously in error in the region of the attractive well; it appears that relaxation data do not usually contain enough information to determine the anisotropy of the well region in atom-diatom systems. This may be contrasted with the situation in diatom-diatom systems,

where there are long range electrostatic forces, and linewidth measurements have frequently been used to determine molecular multipole moments [29].

The most useful relaxation experiment is usually the measurement of spectroscopic lineshapes, since this allows the investigation of inelastic processes involving specific rotational states. NMR relaxation times and sound absorbtion measurements involve an additional average over rotational states, and so provide less detailed information.

1.2.4 Spectroscopic studies

Van der Waals complexes are also formed between nonspherical molecules, but the interpretation of their spectra is much less straightforward than in the spherical case. Most work on anisotropic systems has been on atom-diatom complexes, in which only a single angular coordinate is required to describe the relative orientation of the interacting species.

1.2.4.1 Infrared spectroscopy

The most thorough spectroscopic studies of van der Waals complexes have been those of Welsh and coworkers [30] on $Ar \cdot H_2$ and the rare gas - H_2 series. These complexes have the major advantage that the fundamental mode of the isolated H_2 molecule is electric dipole forbidden, so that only pressure induced and electric quadrupole transitions of the monomer obtrude, and these are of intensity comparable to the spectrum of the complex. Welsh worked at temperatures around 85K, to increase the complex concentration, and found that pressures around

1 Atm or below were necessary to reduce pressure broadening to acceptable levels. Under these conditions, an absorbtion path length of 165 m was used, with a multipass absorbtion cell. Considerable fine structure due to rotational excitation of both the H_2 submolecule and the $Ar \cdot H_2$ complex was observed. Le Roy et al. [1] and Dunker and Gordon [31] have used these spectra to obtain anisotropic potential energy surfaces. The anisotropy in the well region ($\sim 6\ cm^{-1}$ for $Ar \cdot H_2$) is small compared to the rotational constant of H_2 ($\sim 60\ cm^{-1}$), so that there is nearly free rotation of H_2 within the complex, and the H_2 rotational quantum number is nearly a constant of the motion. The rare gas - H_2 potentials are the most accurately known of any anisotropic intermolecular potentials.

A somewhat different type of atom-diatom complex is exemplified by $Ar \cdot N_2$, which has also been studied by long path length infrared spectroscopy [32]. In this complex, the anisotropy in the well region is large compared to the rotational constant of N_2 ($\sim 20\ cm^{-1}$ compared with $2\ cm^{-1}$), so that the complex in its ground state is best considered to be undergoing torsional oscillations about a T-shaped geometry. In excited states correlating with rotationally excited N_2, the motion is again better described as a hindered rotation. The observed spectra for $Ar \cdot N_2$ are at a much lower resolution than those for the H_2 complexes; the height of the barrier to rotation of N_2 in the complex has been estimated assuming a simple sinusoidal model for the potential [32], but a detailed analysis analogous to those for the rare gas - H_2 complexes is not possible.

Infrared spectroscopy on van der Waals complexes containing polar molecules is experimentally more difficult, since there is usually a

strong monomer absorbtion which obscures the spectrum of the complex. Spectra of Ar·HCl and other rare gas - hydrogen halide complexes [33] have been observed in the "windows" between hydrogen halide vibration-rotation lines, but are not sufficiently detailed to allow a full interpretation. However, molecular beam techniques may make it possible to observe such spectra at much higher resolution, when they would provide valuable information on potential energy surfaces.

1.2.4.2 Microwave and radiofrequency spectroscopy

Microwave spectra of hydrogen bonded van der Waals complexes have been observed in the gas phase [34], but for less strongly bound complexes it has not yet been possible to achieve the necessary sensitivity. However, microwave and radiofrequency spectra of many complexes have been observed in molecular beams [35-39], and these spectra provide the most important source of information for the present work. A supersonic nozzle beam provides an ideal environment for observing weakly bound complexes for several reasons

1) Gases undergo considerable cooling in a supersonic expansion, and translational temperatures of a few degrees Kelvin are easily achieved. Rotational and vibrational temperatures are usually somewhat higher than this, but the low temperatures nevertheless lead to the formation of large amounts of van der Waals complexes.

2) Once past the expansion region, the molecular beam is essentially collision-free, so that the initial concentration of complexes is maintained into the region where spectra are observed.

3) Doppler broadening of spectroscopic lines can be virtually eliminated if spectra are observed perpendicular to the direction of

motion of the beam.

Several techniques have been used to obtain rotational spectra of van der Waals complexes in molecular beams; the most important of these for the present work are molecular beam electric resonance (MBER) spectroscopy [35] and pulsed Fourier transform (PFT) spectroscopy [36]. Both of these methods give rotational spectra of van der Waals complexes in their ground vibrational states, but it has not yet proved possible to obtain spectra of molecules in vibrationally excited states. The resolution obtainable with MBER spectroscopy ($\sim$2 kHz) is rather higher than that obtained by PFT spectroscopy ($\sim$6 kHz), and MBER spectroscopy has the additional advantage that Stark induced radio-frequency transitions may be observed; these provide valuable information on the dipole moments of van der Waals complexes.

1.3 Interpretation of rotational spectra

The rare gas - hydrogen halide complexes (collectively Rg·HX) all have linear equilibrium geometries, although they undergo wide amplitude bending motion even in their vibrational ground states. The coordinate system used is shown in figure 1. The vector from the halogen nucleus to the hydrogen nucleus is denoted $\underline{r}$, that from the diatom centre of mass to the rare gas nucleus is $\underline{R}$, and the angle between $\underline{R}$ and $\underline{r}$ is θ. The length of $\underline{R}$ is denoted by R. Throughout this thesis, the approximation is made that there is no coupling between the low frequency van der Waals vibrations and the stretching vibration of the diatomic molecule; in effect, the diatomic molecule is treated as a rigid rotor. The a-inertial axis of the complex lies very close to the $\underline{R}$ vector; the angle between the a axis and the $\underline{r}$ vector is denoted γ, but for most purposes γ and θ indistinguishable.

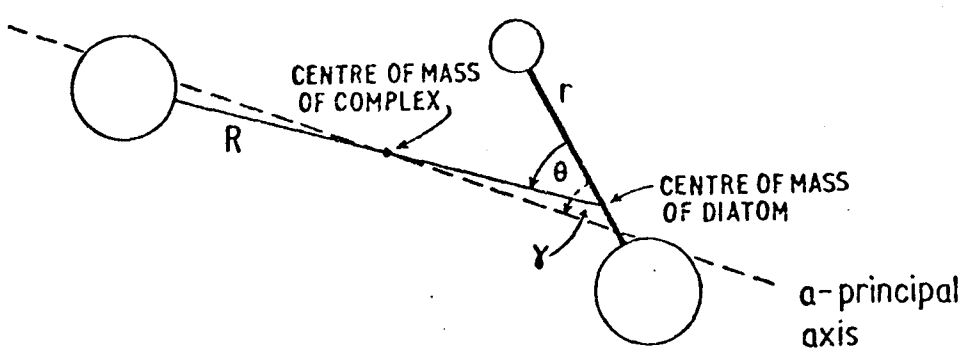

Figure 1.

The energy levels of Rg·HX complexes are most conveniently considered to be those of linear molecules with low frequency bending and stretching modes, although the excited states concerned are not

observed in the microwave region. The rotational energy levels are characterised by simple linear molecule expressions

$$E(J) = E(J=0) + BJ(J+1) - D_J J^2 (J+1)^2$$

with additional structure due to nuclear hyperfine interactions.

Both the rotational constants B and centrifugal distortion constants D_J provide important structural information, as will be seen in chapter 3. The rotational constants provide information on the vibrationally averaged moments of inertia of the complexes, and hence on the equilibrium geometry, while the centrifugal distortion constants measure how easily the intermolecular bond may be stretched by centrifugal forces, and hence provide information on the radial curvature of the potential near equilibrium.

The most important hyperfine splitting is that due to the nuclear electric quadrupole coupling, which occurs for all nuclei with spin $I \geq 1$; the largest quadrupole splittings in the spectra of the Rg·HX complexes discussed here are those for Cl and Br nuclei, although small deuterium quadrupole splittings are also observable. None of the rare gas isotopes considered here has a nuclear quadrupole.

The nuclear quadrupole coupling constants eQq are structurally important because they provide information on the bending motion of the complex in its ground vibrational state. If it is assumed that the electronic structure of the diatomic molecule is unperturbed on complex formation, the quadrupole coupling constant of the complex is just the projection of the monomer coupling constant onto the a-inertial axis of the complex

$$(eQq)^{complex} = (eQq)^{monomer} \langle P_2(\cos\gamma) \rangle$$

The expectation value of $P_2(\cos\gamma)$ is essentially a measure of the amplitude of the zero point bending motion of the complex; it is unity in the limit of a rigid linear complex, and zero if the potential is completely isotropic. Since the quadrupole coupling constants for the free hydrogen halide molecules are known, measurement of $(eQq)^{complex}$ allows $\langle P_2(\cos\gamma)\rangle$ to be calculated. In practice, $\langle P_2(\cos\gamma)\rangle$ is equated with $\langle P_2(\cos\theta)\rangle$, since the $\underline{R}$ axis and the a-inertial axis are almost coincident. The correction to the quadrupole coupling constant due to the difference between these two axes is calculated in chapter 2 and is found to be around 0.1%, which is small compared to the other approximations involved.

The assumption that eQq is unaffected by charge rearrangement on complex formation may be tested for complexes of DCl and DBr, which have two quadrupolar nuclei. A value of $\langle P_2(\cos\theta)\rangle$ may be obtained from each quadrupole coupling constant independently, and the two values should be the same if the model is valid. This comparison has been made for several complexes [37,38], and the agreement was in all cases within the experimental error for the deuterium coupling constant. This verifies that the assumption of the model is accurate to better than 1%.

A further check on the expectation value of $P_2(\cos\theta)$ is provided by the nuclear spin - nuclear spin coupling constant, which should also project in this way

$$d^{complex} = d^{monomer} \langle P_2(\cos\theta)\rangle$$

The expectation values derived from values of d are again in agreement to within their (rather large) error limits [37]. In the case of the

Ar·HF and Kr·HF complexes [39], discussed in chapter 5, the spin-spin coupling constant provides the only measure of $\langle P_2(\cos\theta)\rangle$, since there is no quadrupolar nucleus present.

Angular information of a slightly different type is available from the dipole moment of the complex μ. Since the dipole moment is a vector quantity, it projects as $\langle P_1(\cos\theta)\rangle$, but there are also important contributions from polarisation effects because the presence of a polar molecule induces a dipole moment on the rare gas atom

$$\mu^{\text{complex}} = \mu^{\text{monomer}} \langle P_1(\cos\theta)\rangle + \text{polarisation terms}\ .$$

The presence of the polarisation correction makes the expectation values of $P_1(\cos\theta)$ derived from dipole moments less reliable than those of $P_2(\cos\theta)$ derived from eQq.

The last important spectroscopic constant is the angular centrifugal distortion constant D_θ, which is obtained from the centrifugal distortion of eQq

$$(eQq)_J = (eQq)_{J=0} + D_Q J(J+1),$$

$$\langle P_2(\cos\theta)\rangle_J = \langle P_2(\cos\theta)\rangle_{J=0} + D_\theta J(J+1),$$

$$D_\theta = D_Q/(eQq)^{\text{monomer}}.$$

When the van der Waals complex rotates, the average intermolecular distance increases, so that the anisotropy felt by the HX molecule changes. This alters the expectation value of $P_2(\cos\theta)$, so that the observed quadrupole coupling constant depends on the total angular momentum J. The effect is only a few parts per million in eQq, but provides valuable information on the way in which the potential

anisotropy changes with intermolecular distance.

Most of the van der Waals complexes considered in this thesis can be observed in several isotopic forms, and the isotope shifts in the spectroscopic constants provide much important information. To a good approximation, the intermolecular potential is isotope independent, so that isotopic substitution affects the spectra only through changes in the reduced masses. The most important isotope effects are those observed when DX is substituted for HX in the van der Waals complex; this changes the spectroscopic constants of the complex considerably, since the rotational constant of the diatomic molecule is reduced almost by a factor of 2. This decreases the amplitude of the bending vibration, and has a large effect on the angular expectation values as measured by μ and eQq. Spectra of HX and DX complexes thus probe the intermolecular potential over significantly different angular ranges.

There is one case in which the change in the intermolecular potential with isotopic substitution is significant. The potentials considered in this thesis do not depend explicitly on the HX vibrational coordinate r, and should be interpreted as being averaged over the zero point motion of the diatomic molecule. However, since the amplitude of zero point motion is lower for DX than for HX, the repulsive intermolecular forces are expected to be smaller for deuterium complexes than for the corresponding hydrogen complexes near the linear Rg.D-X geometry. This will lead to a smaller equilibrium intermolecular distance in Rg.DX than Rg.HX, with a correspondingly larger rotational constant for DX complexes than would otherwise be expected. In order to fit potential parameters simultaneously to rotational constants for hydrogen and deuterium isotopic species it is necessary to correct for this effect, and the procedure used for this is described in chapter 4.

REFERENCES

1. R.J. Le Roy, J.S. Carley and J.E. Grabenstetter, Faraday Discus. Chem. Soc. 62, 169 (1977).

2. W. Klemperer, Faraday Discus. Chem. Soc. 62, 309 (1977).

3. G.C. Maitland, M. Rigby, E.B. Smith and W.A. Wakeham, Intermolecular Forces, Oxford University Press (1981).

4. R.J. Le Roy and J.S. Carley, Adv. chem. Phys. 42, 353 (1980).

5. H. Loesch, Adv. chem. Phys. 42, 421 (1980).

6. H.E. Cox, F.W. Crawford, E.B. Smith and A.R. Tindell, Molec. Phys. 40, 705 (1980).

7. D.W. Gough, G.C. Maitland and E.B. Smith, Molec. Phys. 24, 151, (1972).

8. U. Buck, J. chem. Phys. 54, 1923 (1971); U. Buck and H. Pauly, J. chem. Phys. 54, 1929 (1971).

9. R.B. Gerber and M. Shapiro, Chem. Phys. 13, 227 (1976); M. Shapiro and R.B. Gerber, Chem. Phys. 13, 235 (1976).

10. R.J. Le Roy, Semiclassical Methods in Scattering and Spectroscopy, ed. M.S. Child, Reidel, pp. 109-26 (1980).

11. E.A. Colbourn and A.E. Douglas, J. chem. Phys. 65, 1741 (1976).

12. J.A. Barker, R.O. Watts, J.K. Lee, T.P. Schafer and Y.T. Lee, J. chem. Phys. 61, 3080 (1974).

13. W. Meyer, P.C. Hariharan and W. Kutzelnigg, J. chem. Phys. 73, 1880 (1980).

14. S.F. Boys and F. Bernardi, Molec. Phys. 19, 553 (1970).

15. G. Starkschall and R.G. Gordon, J. chem. Phys. 54, 663 (1971).

16. G. Starkschall and R.G. Gordon, J. chem. Phys. 56, 2102 (1972); J. chem. Phys. 56, 2801 (1972).

17. R. Ahlrichs, R. Penco and G. Scoles, Chem. Phys. 19, 119 (1977); K.T. Tang and J.P. Toennies, J. chem. Phys. 66, 1496 (1977).

18. C. Douketis, G. Scoles, S. Marchetti, M. Zen and A.J. Thakkar, J. chem. Phys. to be published.

19. K.T. Tang and J.P. Toennies, J. chem. Phys. 68, 5501 (1978); J. chem. Phys. 74, 1148 (1981); W.R. Rodwell and G. Scoles, J. chem. Phys. to be published.

20. E.B. Smith, D.J. Tildesley, A.R. Tindell and S.L. Price, Chem. Phys. Lett. 74, 193 (1980).

21. R.T. Pack, Chem. Phys. Lett. 55, 197 (1978).

22. C.H. Becker, P.W. Tiedemann, J.J. Valentini and Y.T. Lee, J. chem. Phys. 71, 481 (1979).

23. R.B. Gerber, V. Buch and U. Buck, J. chem. Phys. 72, 3596 (1980).

24. R.B. Gerber, V. Buch, U. Buck, G. Maneke and J. Schleusener, Phys. Rev. Lett. 44, 1397 (1980).

25. L. Zandee and J. Reuss, Chem. Phys. 26, 327 (1977); Chem. Phys. 26, 345 (1977).

26. H.H.W. Thuis, Ph.D. thesis, Nijmegen (1979).

27. R. Schafer and R.G. Gordon, J. chem. Phys. 58, 5422 (1973).

28. W.B. Neilsen and R.G. Gordon, J. chem. Phys. 58, 4131 (1973); E.W. Smith, M. Giraud and J. Cooper, J. chem. Phys. 65, 1256 (1976); E.W. Smith and M. Giraud, J. chem. Phys. 71, 4209 (1979).

29. D.E. Stogryn and A.P. Stogryn, Molec. Phys. 11, 371 (1966).

30. A.R.W. McKellar and H.L. Welsh, J. chem. Phys. 55, 595 (1971); Can. J. Phys. 50, 1458 (1972); Can. J. Phys. 52, 1082 (1974); A.R.W. McKellar, J. chem. Phys. 61, 4636 (1974).

31. A.M. Dunker and R.G. Gordon, J. chem. Phys. 68, 700 (1978).

32. G. Henderson and G.E. Ewing, Molec. Phys. 27, 903 (1974).

33. D.H. Rank, B.S. Rao and T.A. Wiggins, J. chem. Phys. 37, 2511 (1962); D.H. Rank, P. Sitaram, W.A. Glickman and T.A. Wiggins, J. chem. Phys. 39, 2673 (1963); A.W. Miziolek and G.C. Pimentel, J. chem. Phys. 65, 4462 (1976); J. chem. Phys. 66, 3840 (1977).

34. A.C. Legon, D.J. Millen and S.C. Rogers, Proc. Roy. Soc. Lond. A 370, 213 (1980).

35. T.R. Dyke, B.J. Howard and W. Klemperer, J. chem. Phys. 56, 2442 (1972).

36. T.J. Balle, E.J. Campbell, M.R. Keenan and W.H. Flygare, J. chem. Phys. 72, 922 (1980).

37. K.C. Jackson, P.R.R. Langridge-Smith and B.J. Howard, Molec. Phys. 39, 817 (1980); A.E. Barton, T.J. Henderson, P.R.R. Langridge-Smith and B.J. Howard, Chem. Phys. 45, 429 (1980).

38. J.M. Hutson and B.J. Howard, J. chem. Phys. 74, 6520 (1981); A.E. Barton, D.J.B. Howlett and B.J. Howard, Molec. Phys. 41, 619 (1980).

39. T.A. Dixon, C.H. Joyner, F.A. Baiocchi and W. Klemperer, J. chem. Phys. 74, 6539 (1981); L.W. Buxton, E.J. Campbell, M.R. Keenan, T.J. Balle and W.H. Flygare, Chem. Phys. 54, 173 (1981).

CHAPTER 2

THEORETICAL METHODS

CHAPTER 2

THEORETICAL METHODS

The major part of this thesis will deal with least-squares fitting of the parameters of potential surfaces to experimental observables, principally those obtained from rotational spectra of van der Waals molecules and from pressure broadening of hydrogen halide rotational spectra by rare gases. In this chapter, the theoretical methods used to calculate these observables from a proposed potential surface are discussed.

2.1 Molecular beam spectra

As discussed in the Introduction, molecular beam rotational spectra are available for the ground vibrational states of several rare gas - hydrogen halide van der Waals complexes, and these provide the most precise information available on the anisotropic potentials. The spectra obtained are those of K=0 states of near-symmetric tops, which give the appearance of linear molecules; the spectra are interpreted in terms of a single rotational constant B, the corresponding centrifugal distortion constant D_J, and various hyperfine parameters: of particular importance is the nuclear quadrupole coupling constant eQq, since this gives precise information on the amplitude of the zero-point bending motion of the complex.

A suitable theoretical method will therefore give accurate rotational and centrifugal distortion constants and expectation values for the vibrational ground state of a van der Waals complex, starting from a proposed interaction potential. Since the procedure is to be used in performing least-squares fits to potential parameters, it is very

important that the method is computationally fast. Several methods have previously been used for performing calculations on van der Waals complexes, but none of these is suitable for the present purpose:

1) Dunker and Gordon [1] have performed close coupling calculations on Ar.HCl using the piecewise analytic method of Gordon [2], and have obtained rotational constants and angular expectation values for several vibrational states. However, their method is computationally very expensive, and subsequent work [3] had also shown that their ground state energy was significantly in error.

2) Le Roy et al. [3,4] have performed calculations on Ar.HCl using the same potential surface as Dunker and Gordon, expanding the total wavefunction as a sum of products of HCl free-rotor functions with radial functions obtained from the isotropic potential. This method is in principle accurate, but requires the diagonalisation of a very large Hamiltonian matrix in the case of Ar.HCl, so that it is computationally too expensive for use when performing least-squares fits. Nevertheless, the results of Le Roy et al. are useful for testing approximate methods.

3) Holmgren et al. [5] have proposed a method similar to the conventional Born-Oppenheimer approximation, in which the bending and stretching motions of the complex are factorised. This method (Born-Oppenheimer angular-radial separation method, BOARS) will be described in some detail below, since one of the methods used in the present work is an extension of it. However, the BOARS method itself is not sufficiently accurate to allow the full information content of the spectra to be extracted.

4) Kidd et al. [6] have performed close coupling calculations for Ar.HCl on more realistic potential surfaces than those used by Dunker and

Gordon, using the artificial channel method of Shapiro [7]. In its present form, the method provides only energies, not wavefunctions, so that angular expectation values are not available. The method is also too expensive for the present purpose, but provides useful results for comparison with approximate calculations.

Throughout the following discussion, the Ar.HCl system will be used to illustrate the argument, since this is the system which has been most extensively studied using other computational techniques. The methods described are, however, equally applicable to other atom-diatom complexes exhibiting wide amplitude bending motion; in particular, they are suitable for all the rare gas - hydrogen halide van der Waals complexes.

2.1.1 Corrected Born-Oppenheimer method

2.1.1.1 Theory

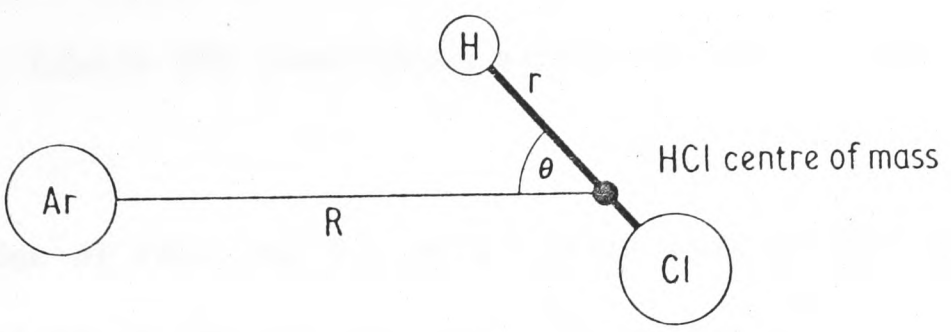

Fig. 1. Coordinate system for Ar.HCl.

Following Holmgren et al. [5], we write the hamiltonian in a molecule-fixed axis system

$$\hat{H} = \frac{\hbar^2}{2\mu}\left[-\frac{\partial^2}{\partial R^2} + \frac{(\hat{J}-\hat{j})^2}{R^2}\right] + V(R,\theta) + b\hat{j}^2 \qquad (1)$$

where μ is the reduced mass $m_{Ar}m_{HCl}/(m_{Ar}+m_{HCl})$, $\hat{J}$ is the operator for the total rotational angular momentum, $\hat{j}$ is the operator for the rotational angular momentum of the diatom, $V(R,\theta)$ is the potential energy and b is the rotational constant of the diatom, which is taken to have its free-molecule value.

The only rigorously good quantum number for Ar·HCl is the total angular momentum J, but there are various other quantum numbers which will be used for labelling the states. The projection of J onto the $\underline{R}$ vector is denoted K and is very nearly a good quantum number. Since the end-over-end rotation of the complex can have no component along $\underline{R}$, K is also the projection of j onto the $\underline{R}$ vector. The j quantum number, for the rotation of the diatomic molecule, is not a good description of the molecular wavefunction for highly hindered rotation, although the

non-crossing rule ensures that it uniquely labels a particular state. In the following discussion a quantum number b is used to label bending states of a particular K in order of ascending energy. In the limit of zero anisotropy, b correlates with j. Finally, a stretching quantum number s labels the stretching states of the van der Waals bond.

The remainder of this section will concentrate on the ground bending and stretching state of the van der Waals bond, since it is rotational excitation of this state that is observed in MBER spectroscopy. Where subscripts are dropped from wavefunctions and energies, they refer to this ground state, which correlates with the j=0 rotational state of free HCl. It is convenient to factorise out immediately all terms in the Hamiltonian which involve the total angular momentum J; these will be reintroduced later by perturbation theory

$$\hat{H} = -\frac{\hbar^2}{2\mu}\frac{\partial^2}{\partial R^2} + V(R,\theta) + b\hat{j}^2 + \frac{\hbar^2}{2\mu R^2}(\hat{J}^2 + \hat{j}^2 - 2\hat{J}.\hat{j}) \quad . \tag{2}$$

Since the end-over-end rotation of the complex can have no component along the a-inertial axis, the operators $\hat{J}_z$ and $\hat{j}_z$ are equivalent. Also, because J is a rigorously good quantum number, the operator $\hat{J}^2$ may be replaced by its eigenvalue J(J+1). The Hamiltonian therefore becomes

$$\hat{H} = -\frac{\hbar^2}{2\mu}\frac{\partial^2}{\partial R^2} + \hat{H}_{bend} + \hat{H}_{rot} + \hat{H}_{cor} \tag{3}$$

where $$\hat{H}_{bend} = V(R,\theta) + b\hat{j}^2 + \frac{\hbar^2}{2\mu R^2}(\hat{j}^2 - 2\hat{j}_z^2) \tag{4}$$

$$\hat{H}_{rot} = \frac{\hbar^2 J(J+1)}{2\mu R^2} \tag{5}$$

$$\hat{H}_{cor} = \frac{-\hbar^2}{\mu R^2} (\hat{J}_x \hat{j}_x + \hat{J}_y \hat{j}_y) \ . \tag{6}$$

The total wavefunction is now expanded in terms of angular functions $\{\phi_b(\theta;R)\}$ which diagonalise $\hat{H}_{bend}$ at each value of the intermolecular distance R

$$\psi_{bs} = \sum_{b'} \phi_{b'}(\theta,R)\ \chi_{bs;b'}(R) \tag{7}$$

$$[\hat{H}_{bend} - U_{b'}^{BO}(R)]\ \phi_{b'}(\theta;R) = 0 \tag{8}$$

where the R-dependent eigenvalues $U_{b'}^{BO}(R)$ form a series of effective (Born-Oppenheimer) potentials for the bending motion of the complex. Substituting equation (7) into the rotationless total Schrödinger equation and projecting onto $\phi_{b''}(\theta;R)$ yields a set of coupled differential equations for the $\{\chi_{bs;b'}(R)\}$

$$\left[-\frac{\hbar^2}{2\mu}\frac{d^2}{dR^2} + U_{b''}^{BO}(R) - E_{bs}\right]\chi_{bs;b''}(R) = \sum_{b'} \left(f_{b''b'}(R) + g_{b''b'}(R)\frac{d}{dR}\right)\chi_{bs;b'}(R) \tag{9}$$

where the matrix elements of $f_{b''b'}(R)$ and $g_{b''b'}(R)$ are defined by

$$f_{b''b'}(R) = \frac{\hbar^2}{2\mu}\int \phi_{b''}^{*}(\theta;R)\frac{d^2}{dR^2}\phi_{b'}(\theta;R)\sin\theta\, d\theta \tag{10}$$

$$g_{b''b'}(R) = \frac{\hbar}{\mu}\int \phi_{b''}^{*}(\theta;R)\frac{d}{dR}\phi_{b'}(\theta;R)\sin\theta\, d\theta \ . \tag{11}$$

It is in principle possible to solve these coupled differential

equations as they stand, but the principal advantage of the adiabatic formulation lies in the availability of approximate solutions, which are computationally very much easier to obtain. The simplest of these is analogous to the ordinary Born-Oppenheimer approximation, and is obtained when all the terms on the right hand side of equation (9) are neglected. The total wavefunction is then a simple product function

$$\psi_{bs}^{BO} = \phi_b(\theta;R)\ \chi_{bs}^{BO}(R) \tag{12}$$

where the stretching wavefunction is an eigenvalue of the one dimensional Schrödinger equation

$$\left[-\frac{\hbar^2}{2\mu}\frac{d^2}{dR^2} + U_b^{BO}(R) - E_{bs}^{BO} \right] \chi_{bs}^{BO}(R) = 0 \ . \tag{13}$$

This is the lower-bound BOARS approximation of Holmgren et al. For the ground state, E_{00}^{BO} provides a lower bound to the true energy E_{00}, provided the basis set used in solving equation (8) is complete.

At the next level of approximation (adiabatic approximation [5]), the diagonal term from the right hand side of equation (9) is included, but all off-diagonal terms are neglected. This still yields a solution where the total wavefunction is a single product function, but the stretching wavefunction is defined by

$$\left[-\frac{\hbar^2}{2\mu}\frac{d^2}{dR^2} + U_b^{Ad}(R) - E_{bs}^{Ad} \right] \chi_{bs}^{Ad}(R) = 0 \tag{14}$$

where the adiabatic potential is given by

$$U_b^{Ad}(R) = U_b^{BO}(R) - f_{bb}(R) \ . \tag{15}$$

The correction term $-f_{bb}(R)$ is always positive (see section 2.1.1.2 below), and the adiabatic approximation in fact provides an upper bound to the true ground-state energy.

The Born-Oppenheimer and adiabatic approximations for the ground state of Ar.HCl were considered by Holmgren et al., who showed that they provided reasonable estimates of the ground state energies and properties of Ar.HCl and Ar.DCl. Nevertheless, the effects of the neglected terms ("non-adiabatic" terms, $\hat{H}_{na}$) are considerably larger than the experimental uncertainties, and it is preferable to include them. Provided the adiabatic approximation is reasonably accurate, this may be done by perturbation theory, starting from the adiabatic solution. The resulting method (Corrected Born-Oppenheimer method , CBO) will be described in the following sections.

2.1.1.2 Matrix elements

Matrix elements of $\hat{H}_{rot}$, $\hat{H}_{cor}$ and $\hat{H}_{na}$ between the bending wavefunctions $\{\phi_b(\theta;R)\}$ are required. These are most simply obtained if the bending Schrödinger equation (7) is solved in a basis set of spherical harmonics for the internal rotation of HCl in the complex

$$\phi_b{}^K(\theta;R) = \sum_j a_{bj}{}^K(R)\ Y_j{}^K(\theta) \qquad (16)$$

where the azimuthal angle γ has been suppressed. The body-fixed projection quantum number K has been introduced because $\hat{H}_{bend}$ is diagonal in this quantum number; the only mixing between states of different K is introduced by the Coriolis perturbation $\hat{H}_{cor}$.

The matrix elements of the rotational and Coriolis perturbations

may be simply obtained in this representation. $\hat{H}_{rot}$ is simply a multiplying operator with only diagonal matrix elements

$$\langle \phi_b^K | \hat{H}_{rot} | \phi_c^M \rangle = \frac{\hbar^2}{2\mu R^2} J(J+1) \delta_{bc} \delta_{KM} \tag{17}$$

where the integration is over angular coordinates only.

$\hat{H}_{cor}$ may be written in terms of the shift operators $\hat{J}_{\pm}$ and $\hat{j}_{\pm}$, and has matrix elements only between states with $\Delta K = \pm 1$

$$\langle \phi_b^K | \hat{H}_{cor} | \phi_c^M \rangle = \frac{-\hbar^2}{2\mu R^2} \sum_j a_{bj}^{K*}(R) \, a_{cj}^{M}(R) \, [j(j+1)-KM]^{\frac{1}{2}}$$

$$\times [J(J+1)-KM]^{\frac{1}{2}} (\delta_{K,M+1} + \delta_{K,M-1}) . \tag{18}$$

The matrix elements of d/dR and d^2/dR^2 required for $\hat{H}_{na}$ could be evaluated by numerical differentiation of the coefficients $a_{bj}^{K}(R)$ of equation (16). However, algebraic expressions for these matrix elements have been given by Child [8], and the use of these expressions is both more convenient and more accurate

$$g_{bc}(R) = \langle \phi_b | d/dR | \phi_c \rangle = \frac{\langle \phi_b | d\hat{H}_{bend}/dR | \phi_c \rangle}{[U_c^{BO}(R) - U_b^{BO}(R)]} \qquad \text{for } b \neq c \tag{19}$$

$$f_{bc}(R) = \langle \phi_b | d^2/dR^2 | \phi_c \rangle = 2 \sum_{d \neq b,c} \frac{\langle \phi_b | d\hat{H}_{bend}/dR | \phi_d \rangle \langle \phi_d | d\hat{H}_{bend}/dR | \phi_c \rangle}{[U_b^{BO}(R) - U_c^{BO}(R)] [U_d^{BO}(R) - U_c^{BO}(R)]}$$

$$+ 2 \, d/dR [U_b^{BO}(R) - U_c^{BO}(R)] \frac{\langle \phi_b | d\hat{H}_{bend}/dR | \phi_c \rangle}{[U_b^{BO}(R) - U_c^{BO}(R)]^2}$$

$$- \frac{\langle \phi_b | d^2\hat{H}_{bend}/dR^2 | \phi_c \rangle}{[U_b^{BO}(R) - U_c^{BO}(R)]} \qquad \text{for } b \neq c . \tag{20}$$

The diagonal terms $g_{bb}(R)$ are zero, but the diagonal second derivative terms are not, and are required for the adiabatic corrections

$$f_{bb}(R) = -\sum_{c\neq b} \frac{|\langle\phi_b|d\hat{H}_{bend}/dR|\phi_c\rangle|^2}{[U_b^{BO}(R) - U_c^{BO}(R)]^2} \qquad (21)$$

The adiabatic corrections are small in regions where the bending wavefunctions $\{\phi_b(\theta;R)\}$ are changing slowly, but have sharp positive peaks if the character of the functions changes fast. For realistic Ar.HCl potentials, the angular minimum is at the linear Ar.H-Cl configuration for large intermolecular distances, but moves to the linear Ar.Cl-H geometry when the repulsive forces dominate. This gives a fast change in $\phi_0(\theta;R)$ in the region of the potential well, and sharp peaks appear in both the adiabatic and non-adiabatic terms as a function of R.

2.1.1.3 Calculation of spectroscopic parameters

The molecular properties obtainable from MBER spectra are the rotational constant B, the centrifugal distortion constant D_J, the angular expectation values $\langle P_1(\cos\theta)\rangle$ and $\langle P_2(\cos\theta)\rangle$, and the angular centrifugal distortion constant D_θ. In previous calculations [1,3,4], spectroscopic constants such as B and D_J have been determined by a least-squares procedure: the ground state energy was evaluated for several values of the rotational quantum number J, and these energies fitted to a quadratic in J(J+1) to obtain B and D_J. This procedure is unsatisfactory for two reasons: First, solving the entire problem for different J values involves the duplication of considerable computational effort and, secondly, the results are likely to be unstable with respect to any systematic errors in the eigenvalues, since small differences between large numbers must be calculated. In the CBO method used here,

these spectroscopic parameters are calculated in a single step, by perturbation theory [9,10]. Thus the rotational constant is the coefficient of J(J+1) in the expression for the total energy, and D_J is obtained from the coefficient of $J^2(J+1)^2$.

Contributions to the rotational constant will arise from two sources: the required J(J+1) dependence may be provided either by terms first order in $\hat{H}_{rot}$ (with a J(J+1) dependence, equation (17)) or by terms second order in $\hat{H}_{cor}$ (with a $[J(J+1)]^{1/2}$ dependence, equation (18)). However, all orders of the non-adiabatic perturbation $\hat{H}_{na}$ will contribute and we require convergence of the perturbation series for this perturbation. If the total hamiltonian is written

$$\hat{H} = \hat{H}^{(0)} + \lambda\hat{H}_{na} + \mu\hat{H}_{rot} + \nu\hat{H}_{cor} \qquad (22)$$

where $\hat{H}^{(0)}$ is the adiabatic hamiltonian, and the energy and wavefunction are expanded in powers of λ, μ and ν

$$E = \sum_{\ell=0}^{\infty}\sum_{m=0}^{\infty}\sum_{n=0}^{\infty} \lambda^{\ell}\,\mu^{m}\,\nu^{n}\,E^{(\ell mn)} \qquad (23)$$

$$\psi = \sum_{\ell=0}^{\infty}\sum_{m=0}^{\infty}\sum_{n=0}^{\infty} \lambda^{\ell}\,\mu^{m}\,\nu^{n}\,\psi^{(\ell mn)} \qquad (24)$$

then these expressions may be substituted into the total Schrödinger equation and a series of perturbation equations may be obtained by collecting powers of λ, μ and ν. This procedure is simply a generalisation of the usual perturbation theory expansion and has been reviewed by Hirschfelder et al. [11]. The general form of the (ℓmn)th equation is

$$\hat{H}^{(0)}\psi^{(\ell mn)} + \hat{H}_{na}\psi^{(\ell-1,mn)} + \hat{H}_{rot}\psi^{(\ell,m-1,n)} + \hat{H}_{cor}\psi^{(\ell m,n-1)}$$

$$\sum_{p=0}^{\ell}\sum_{q=0}^{m}\sum_{r=0}^{n} E^{(pqr)}\psi^{(\ell-p,m-q,n-r)}. \qquad (25)$$

where $E^{(000)}$ and $\psi^{(000)}$ are the adiabatic energy and wavefunction respectively. Many of the lower order perturbation equations are simplified by the fact that the different perturbations do not connect the same excited states to the ground state. Thus there is a selection rule of $\Delta K = \pm 1$ for the Coriolis terms, so that only perturbation terms of even order in $\hat{H}_{cor}$ can contribute to the ground-state energy: that is, $E^{(\ell mn)}=0$ for n odd. Similarly, the non-adiabatic perturbation has no matrix elements diagonal in the bending state ϕ, so that $E^{(lm0)}=0$ for all m.

With this notation, the rotational constant B is given by

$$BJ(J+1) = \sum_{\ell} (E^{(\ell 10)} + E^{(\ell 02)}) \qquad (26)$$

where the two terms arise from $\hat{H}_{rot}$ and $\hat{H}_{cor}$ respectively, as discussed above. Considering first the terms due to $\hat{H}_{rot}$ alone, we write out the relevant perturbation equations explicity

$$[\hat{H}^{(0)} - E^{(000)}]\psi^{(010)} = [E^{(010)} - \hat{H}_{rot}]\psi^{(000)} \qquad (27)$$

$$[\hat{H}^{(0)} - E^{(000)}]\psi^{(100)} = [E^{(100)} - \hat{H}_{na}]\psi^{(000)} \qquad (28)$$

$$[\hat{H}^{(0)} - E^{(000)}]\psi^{(200)} = [E^{(100)} - \hat{H}_{na}]\psi^{(100)} + E^{(200)}\psi^{(000)} \qquad (29)$$

$$[\hat{H}^{(0)} - E^{(000)}]\psi^{(110)} = [E^{(100)} - \hat{H}_{na}]\psi^{(010)} + [E^{(010)} - \hat{H}_{rot}]\psi^{(100)} + E^{(110)}\psi^{(000)} \qquad (30)$$

$$[\hat{H}^{(0)} - E^{(000)}]\psi^{(210)} = [E^{(100)} - \hat{H}_{na}]\psi^{(110)} + [E^{(010)} - \hat{H}_{rot}]\psi^{(200)}$$

$$+ E^{(110)}\psi^{(100)} + E^{(210)}\psi^{(000)} . \tag{31}$$

These may be simplified slightly since $E^{(100)}$ and $E^{(110)}$ vanish as mentioned above. To solve these equations, the various $\psi^{(\ell mn)}$ are expanded in terms of the bending functions $\{\phi_b(\theta;R)\}$

$$\psi^{(\ell mn)} = \sum_b \phi_b(\theta;R)\ \chi_b{}^{(\ell mn)}(R) . \tag{32}$$

This yields simple inhomogeneous differential equations for the functions $\chi_b{}^{(\ell mn)}(R)$. For example, equation (28) becomes

$$\left[-\frac{\hbar^2}{2\mu}\frac{d^2}{dR^2} + U_b(R) - E^{(000)}\right]\chi_b^{(100)}(R) = (f_{b0}(R) + g_{b0}(R)\frac{d}{dR})\ \chi^{(000)}(R) . \tag{33}$$

The numerical method used to solve equations of this type is described in Appendix 1. It is <u>not</u> necessary to expand the functions $\{\chi_b{}^{(\ell mn)}(R)\}$ in terms of a basis set of stretching wavefunctions.

An expression for the rotational constant B may now be obtained. Projecting equation (27) onto $\psi^{(000)}$ gives

$$<000|\hat{H}^{(0)} - E^{(000)}|010> = <000|E^{(010)} - \hat{H}_{rot}|000> \tag{34}$$

where the labels of the bracket notation refer to orders of perturbation theory (ℓmn) not quantum numbers. Since $\psi^{(000)}$ is an eigenfunction of $\hat{H}^{(0)}$ with eigenvalue $E^{(000)}$, the left-hand side of this equation vanishes by hermiticity, and we obtain the zeroth order approximation to the rotational constant

$$E^{(010)} = \langle 000|\hat{H}_{\rm rot}|000\rangle. \tag{35}$$

The first order non-adiabatic term $E^{(110)}$ vanishes, but $E^{(210)}$ does not. From equation (31) we have

$$\langle 000|\hat{H}^{(0)} - E^{(000)}|210\rangle = \langle 000|-\hat{H}_{na}|110\rangle + \langle 000|E^{(010)} - \hat{H}_{\rm rot}|200\rangle + E^{(210)}\langle 000|000\rangle. \tag{36}$$

The left-hand side again vanishes as above and the remaining terms may be simplified by substituting for $\psi^{(110)}$ and $\psi^{(200)}$ from their defining equations (30) and (29)

$$\begin{aligned} E^{(210)} &= -\langle 100|\hat{H}^{(0)} - E^{(000)}|110\rangle - \langle 010|\hat{H}^{(0)} - E^{(000)}|200\rangle \\ &= 2\langle 100|\hat{H}_{na}|010\rangle + \langle 100|\hat{H}_{\rm rot} - E^{(010)}|100\rangle. \end{aligned} \tag{37}$$

Note that this expression does not involve any wavefunctions $\psi^{(\ell mn)}$ from perturbation equations of higher than first order. In order to obtain the second order non-adiabatic correction to B, it is necessary to solve only equations (27) and (28) explicitly.

The Coriolis contribution to the rotational constant is derived similarly. In addition to equation (27) defining $\psi^{(100)}$, we require

$$[\hat{H}^{(0)} - E^{(000)}]\psi^{(001)} = -\hat{H}_{\rm cor}\psi^{(000)} \tag{38}$$

$$[\hat{H}^{(0)} - E^{(000)}]\psi^{(002)} = -\hat{H}_{\rm cor}\psi^{(001)} + E^{(002)}\,\psi^{(000)} \tag{39}$$

$$[\hat{H}^{(0)} - E^{(000)}]\psi^{(101)} = -\hat{H}_{\rm cor}\psi^{(100)} - \hat{H}_{na}\psi^{(001)} \tag{40}$$

$$[\hat{H}^{(0)} - E^{(000)}]\psi^{(102)} = -\hat{H}_{\rm cor}\psi^{(101)} - \hat{H}_{na}\psi^{(002)} + E^{(002)}\psi^{(100)} + E^{(102)}\psi^{(000)}. \tag{41}$$

From equation (39) the leading Coriolis contribution to B is

$$E^{(002)} = \langle 000|\hat{H}_{\rm cor}|001\rangle \tag{42}$$

and from equation (41) there is also a non-adiabatic Coriolis term

$$E^{(102)} = \langle 000|\hat{H}_{\rm cor}|101\rangle + \langle 000|\hat{H}_{na}|002\rangle. \tag{43}$$

Using the definitions of the various perturbation wavefunctions, this becomes

$$\begin{aligned} E^{(102)} &= \langle 001|E^{(000)} - \hat{H}^{(0)}|101\rangle + \langle 100|E^{(000)} - \hat{H}^{(0)}|002\rangle \\ &= 2\langle 001|\hat{H}_{\rm cor}|100\rangle + \langle 001|\hat{H}_{na}|001\rangle. \end{aligned} \tag{44}$$

Again, although the derivation of this expression involves higher order perturbation equations such as (39) and (40), it is not necessary to solve these explicitly, since only $\psi^{(100)}$ and $\psi^{(001)}$ appear in the final result.

Collecting equations (35), (37), (42) and (44), we obtain for the leading terms in equation (26)

$$\begin{aligned} BJ(J+1) &= E^{(010)} + E^{(210)} + E^{(002)} + E^{(102)} \\ &= \langle 000|\hat{H}_{\rm rot}|000\rangle \\ &\quad + 2\langle 100|\hat{H}_{na}|010\rangle + \langle 100|\hat{H}_{\rm rot} - E^{(010)}|100\rangle \\ &\quad + \langle 000|\hat{H}_{\rm cor}|001\rangle \\ &\quad + 2\langle 002|\hat{H}_{\rm cor}|100\rangle + \langle 001|\hat{H}_{na}|001\rangle. \end{aligned} \tag{45}$$

Analogous expressions may be derived for the other spectroscopic constants and evaluated in the same way. Thus for the centrifugal distortion constant

$$-D_J J^2(J+1)^2 = \sum_{\ell} (E^{(\ell 20)} + E^{(\ell 12)} + E^{(\ell 04)}). \tag{46}$$

$E^{(\ell 04)}$ is fourth order in the Coriolis perturbation and may safely be neglected. The leading non-adiabatic contribution to the centrifugal distortion constant D_J is from $E^{(220)}$, and the final expression for D_J (including terms up to second order in $\hat{H}_{cor}$ and $\hat{H}_{na}$) is

$$\begin{aligned} -D_J J^2(J+1)^2 = &\langle 000|\hat{H}_{\rm rot} - E^{(010)}|010\rangle + \langle 001|\hat{H}_{\rm rot} - E^{(010)}|001\rangle \\ &+ 2\langle 010|\hat{H}_{\rm cor}|001\rangle + 2\langle 200|\hat{H}_{\rm rot} - E^{(010)}|010\rangle \\ &+ \langle 110|\hat{H}_{na}|010\rangle + \langle 110|\hat{H}_{\rm rot} - E^{(010)}|100\rangle \\ &- E^{(020)}\langle 100|100\rangle. \end{aligned} \tag{47}$$

In order to calculate the expectation values of the Legendre polynomials $P_2(\cos\theta)$ and $P_1(\cos\theta)$, which are required in the calculation of the nuclear quadrupole coupling constant and dipole moment of the complex, we introduce a fictitious perturbation hamiltonian [11] $P_2(\cos\theta)$ (or $P_1(\cos\theta)$), and solve the additional first order perturbation equation for the wavefunction correction $\pi(\theta,R)$

$$[\hat{H}^{(0)} - E^{(000)}]\pi = \xi[P_2(\cos\theta) - \langle P_2\rangle^{(0)}]\psi^{(0)} \tag{48}$$

where the constant ξ has units of energy, and has been introduced merely to satisfy the requirements of dimensionality. It will cancel from the final result. $\langle P_2\rangle^{(0)}$ is the zeroth order expectation value of $P_2(\cos\theta)$

$$\langle P_2\rangle^{(0)} = \langle 000|P_2(\cos\theta)|000\rangle. \tag{49}$$

Because $P_2(\cos\theta)$ had matrix elements off-diagonal in bending state $\phi(\theta;R)$, there is a correction to its expectation value first order in the non-adiabatic perturbation. This contrasts with the rotational constant, where the leading non-adiabatic term is second order in $\hat{H}_{na}$, since $\hat{H}_{rot}$ has no matrix elements off-diagonal in bending state. Proceeding by an argument similar to that for the rotational constant, we obtain for the expectation value of $P_2(\cos\theta)$, to second order in $\hat{H}_{na}$

$$\begin{aligned}\langle P_2(\cos\theta)\rangle = {} & \langle 000|P_2(\cos\theta)|000\rangle \\ & + 2\langle 000|P_2(\cos\theta)|100\rangle \\ & + 2\langle 100|\hat{H}_{na}/\xi|\pi\rangle + \langle 100|P_2(\cos\theta) - \langle P_2\rangle^{(0)}|100\rangle.\end{aligned} \tag{50}$$

The final result for $\langle P_1(\cos\theta)\rangle$ is similar, but with the appropriate changes in the matrix elements and in the definition of $\pi(\theta;R)$.

Further potential information is available from D_θ, the centrifugal distortion constant for $\langle P_2(\cos\theta)\rangle$

$$\langle P_2(\cos\theta)\rangle_J = \langle P_2(\cos\theta)\rangle_0 + D_\theta J(J+1). \tag{51}$$

and this quantity has now been observed for several van der Waals complexes [7-9]. In the perturbation treatment, D_θ arises as the J(J+1) coefficient of $\langle P_2(\cos\theta)\rangle$ and there are again contributions from both $\hat{H}_{rot}$ and $\hat{H}_{cor}$. The final result is

$$D_\theta\, J(J+1) = 2\langle 000|P_2(\cos\theta)|010\rangle$$

$$+ 2\langle 100|(\hat{H}_{rot}-E^{(010)}/\xi|\pi\rangle + \langle 100|P_2(\cos\theta)|010\rangle$$

$$+ 2\langle 010|\hat{H}_{na}/\xi|\pi\rangle$$

$$+ 2\langle 001|\hat{H}_{cor}/\xi|\pi\rangle\ \langle 001|P_2(\cos\theta)-\langle P_2\rangle^{(0)}|001\rangle\,. \qquad (52)$$

A qualitative understanding of the effect of the non-adiabatic perturbation may be obtained from figure 2, where the ground and first excited K = 0 state adiabatic potentials are plotted for a typical Ar.HCl potential, together with the zeroth order ground state wavefunction $\chi^{(000)}(R)$ and the first order non-adiabatic correction $\chi_1{}^{(100)}(R)$ from the first excited bending state. The lower part of the figure shows the non-adiabatic coupling terms $f_{10}(R)$ and $g_{10}(R)$.

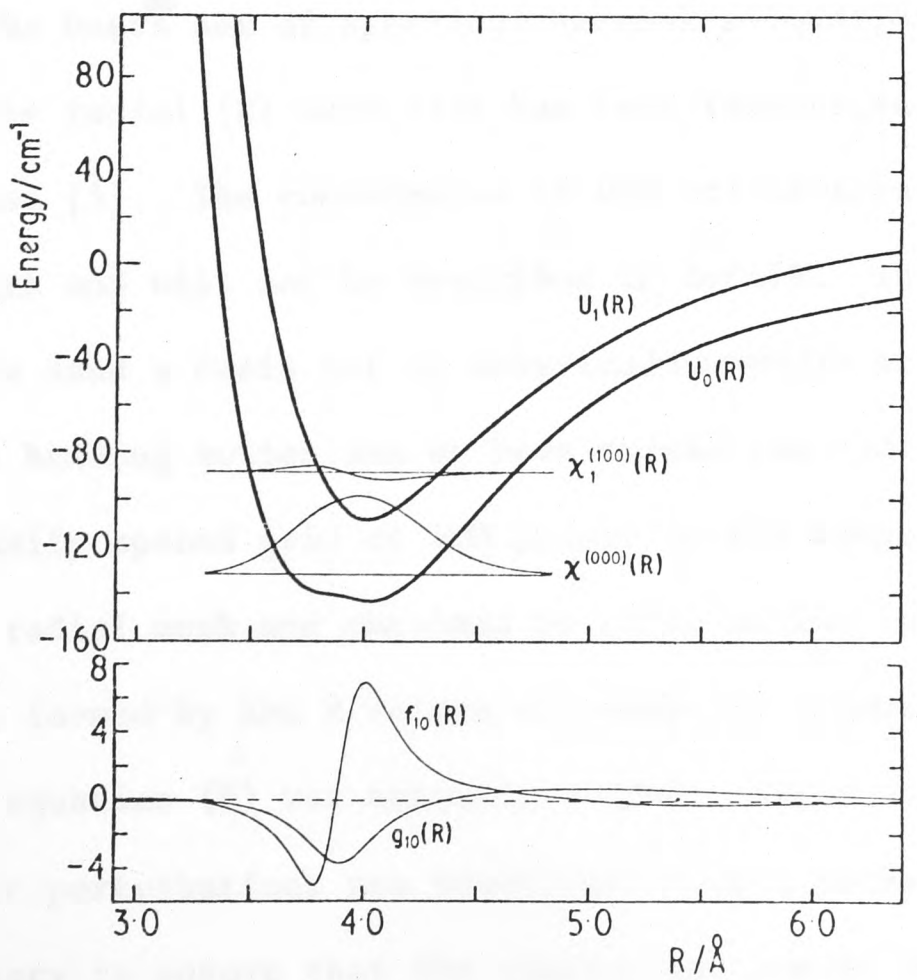

Figure 2. Potential energy curves and wavefunction contributions for the lowest two bending states of the DG potential. The lower part of the figure shows the matrix elements of the non-adiabatic perturbation (see text).

The correction wavefunction $\chi_1^{(100)}$, obtained by solving equation (33), is equivalent to a sum over contributions from all stretching states of the b=1 bending state which are mixed into the ground state by the non-adiabatic perturbation. However, although there are contributions from highly excited (and fast-oscillating) zeroth order wave-functions, $\chi_1^{(100)}$ itself is a well behaved, slowly varying function. This is another feature favouring the direct solution method of Appendix 1, since it is unnecessary to use a very fine radial grid to allow for fast-oscillating components of the perturbed wave-function.

2.1.1.4 Convergence

The corrected Born-Oppenheimer (CBO) method described above is an extension of the Born-Oppenheimer angular-radial separation (BOARS) method of Holmgren et al. [5] and the convergence of BOARS results with respect to the basis set of spherical harmonics (equation (16)) and with respect to the radial (R) mesh size has been investigated in their original paper [5]. The convergence of CBO calculations is similar in these respects and will not be described in detail. In the calculations below we have used a basis set of spherical harmonics with $j_{max}=7$ to describe the bending motion and we have solved the radial equations using an equally spaced grid of 400 points on the range R = 3.0Å to 6.0Å. This radial mesh was obtained by cubic spline interpolation in a coarse grid, formed by the R values at which the clamped-nucleus Schrodinger equation (8) was actually solved. Since the adiabatic and non-adiabatic perturbations are sometimes sharply peaked functions of R, it is necessary to ensure that the coarse mesh points are sufficiently close together to describe the spike accurately. This is achieved by using a closer mesh in this region only, but because the nature of the

spike varies considerably between potentials it is not possible to give general rules for the required mesh.

We have investigated the convergence of CBO calculations with respect to the basis set of bending states $\{\phi_b(\theta;R)\}$ introduced by the non-adiabatic perturbation. We performed calculations for the Ar·H^{35}Cl isotope on potential IIb of Holmgren et al. [12] (HWK potential, figure 3). This potential was the one which gave the best fit to the MBER data, using the BOARS method for calculating spectroscopic parameters. The results of this convergence test are shown in table 1, and it may be seen that convergence is essentially complete when 3 excited bending states are included.

There is no question of convergence with respect to a basis set of stretching states, since the perturbation equations are solved directly, without introducing a basis set of zeroth order stretching states. This is equivalent to using an infinite basis set for the R coordinate.

Table 1. Convergence of CBO calculations with respect to basis set of bending states for Ar·H^{35}Cl on HWK surface. Note that the number of $K = \pm 1$ bending states used is the same as for $K = 0$.

b_{max}	E/cm^{-1}	B/MHz	$\langle P_2(\cos\theta)\rangle$
0	-126.800	1673.471	0.36971
1	-127.939	1685.860	0.35636
2	-128.129	1687.949	0.36164
3	-128.139	1688.050	0.36240
4	-128.139	1688.051	0.36240

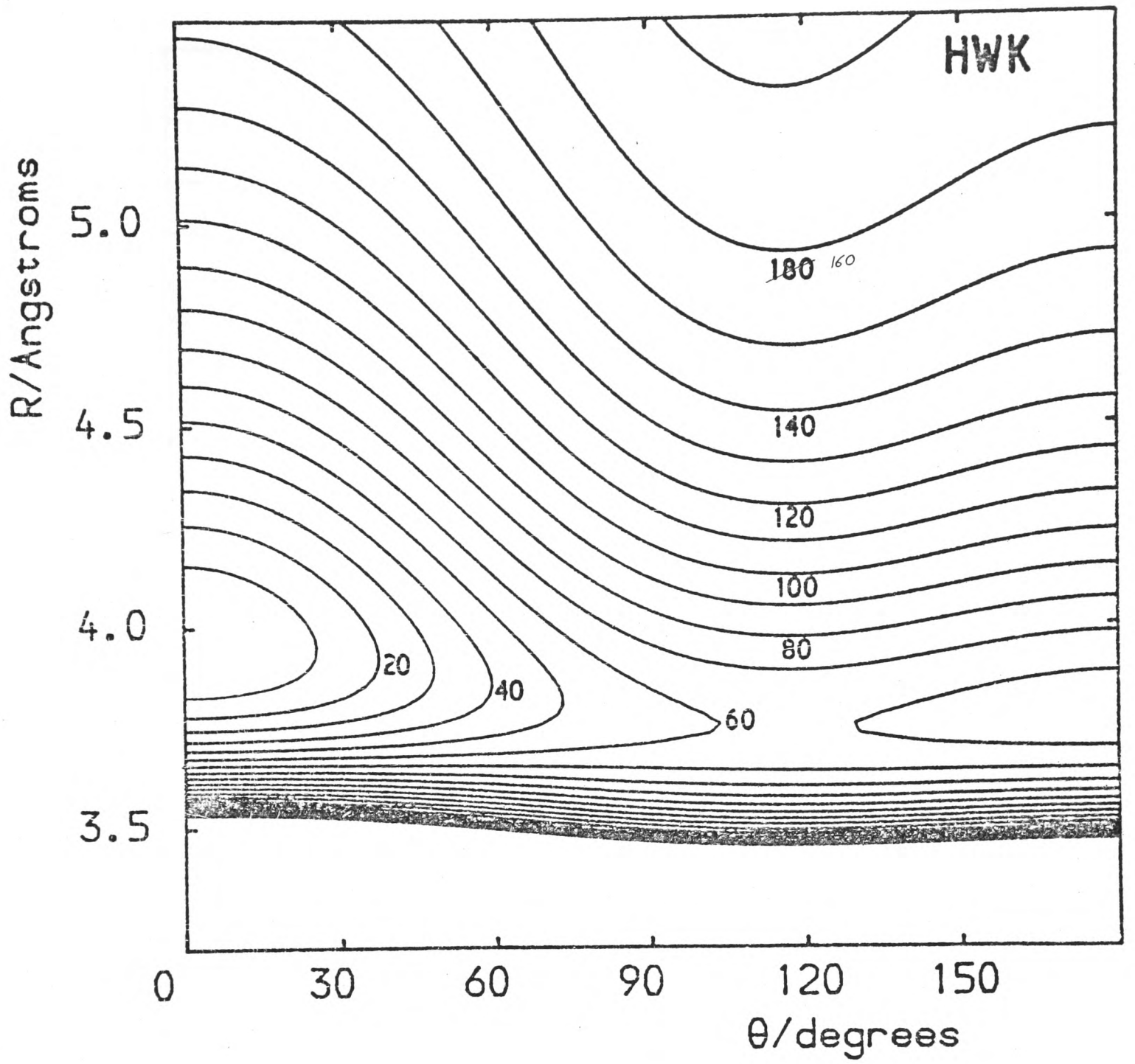

Figure 3. Contour plot of potential IIb of Holmgren et al. for Ar·HCl (HWK potential).
Contours are plotted at 10 cm^{-1} intervals relative to the absolute minimum at -183.3 cm^{-1}.

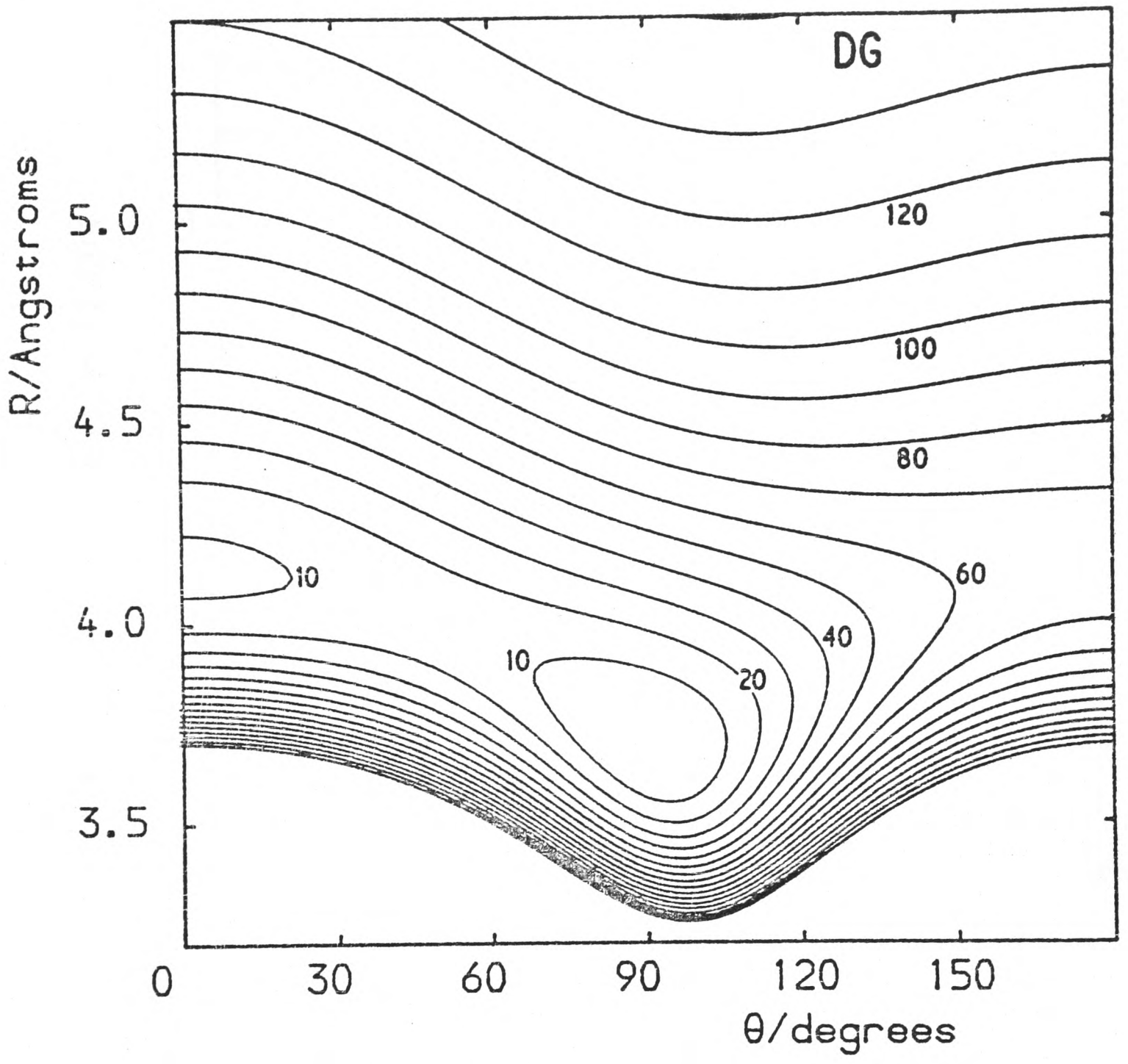

Figure 4. Contour plot of potential I of Dunker and Gordon for Ar·HCl (DG potential).
Contours are plotted at 10 cm^{-1} intervals relative to the absolute minimum at -168.3 cm^{-1}.

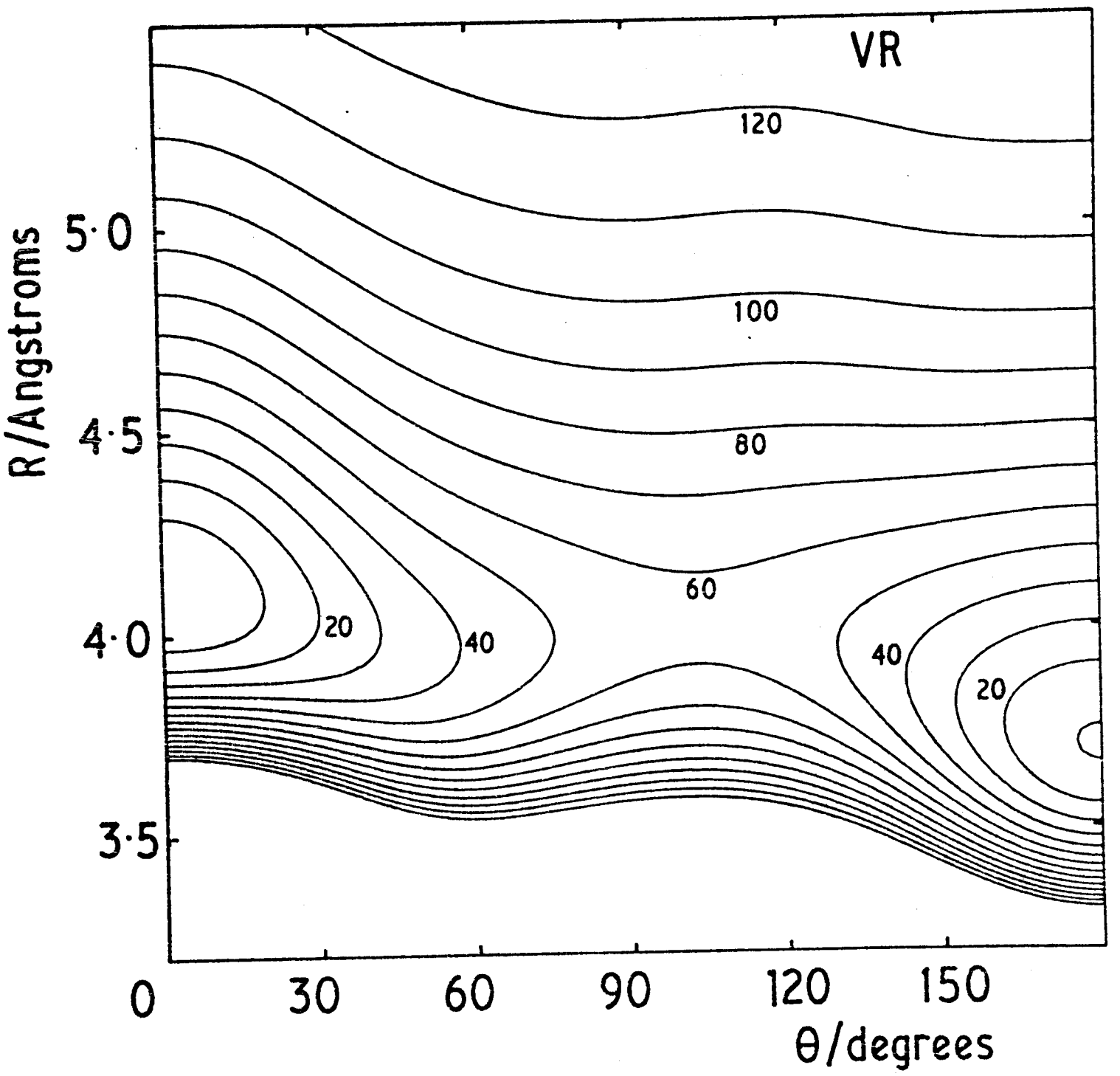

Figure 5. Contour plot of the *ab initio* potential of Vliegenthart and Rozendaal for Ar·HCl (VR potential).
Contours are plotted at 10 cm^{-1} intervals relative to the absolute minimum at -149.3 cm^{-1}.

2.1.1.5 Comparison with previous calculations

Calculations on the Ar.HCl system have been carried out by several authors [1,3,4,6], as discussed above. The potential for which most previous calculations are available is potential I of Dunker and Gordon (DG potential, figure 4), and in table 2 CBO calculations on this potential are compared with close-coupling [1,6], secular determinant [3,4], BO and adiabatic results. All calculations use a basis set with $j_{max} = 4$ for Ar·HCl and $j_{max} = 5$ for Ar·DCl; these basis sets are not quite fully converged, but have been used here to maintain comparability with the earlier calculations. The centre of mass shift for the Ar·DCl calculations has been performed using the approximate results of Dunker and Gordon for the same reason.

Table 2. Comparison of CBO method with previous calculations, using Dunker and Gordon potential 1.

	E/cm^{-1}	B/MHz	D_J/kHz	$\langle P_2(\cos\theta)\rangle$
		$Ar \cdot H^{35}Cl$		
Close coupling [1]	-132.436	1690±3	28±15	-0.02704
Close coupling [6]	-132.495	1693.2	37.0	-
Secular determinant	-132.497	1693±1	40±2	-
BO	-134.048	1700.682	34.05	-0.00735
Adiabatic	-131.702	1688.253	37.50	0.00743
CBO	-132.473±0.04	1693.001±1.0	38.15±0.5	-0.02808±0.001
		$Ar.D^{35}Cl$		
Close coupling [1]	-136.016	1686±3	45±15	-0.03263
BO	-138.524	1692.566	36.89	0.01476
Adiabatic	-134.232	1673.077	46.84	0.04647
CBO	-135.983±0.08	1686.580±2.0	48.85±0.5	-0.03345±0.001

It may be seen from table 2 that the CBO method gives a dramatic improvement over the adiabatic values for both the ground state energy and the expectation value of $P_2(\cos\theta)$. The second order ground state energy for Ar·HCl on the DG surface is $-132.473cm^{-1}$, which is still slightly above the secular determinant energy calculated by LeRoy et al. [3]. However, when third and fourth order terms are included, the CBO method gives $-132.496cm^{-1}$, in good agreement with the secular determinant result of $-132.497cm^{-1}$. The only spectroscopic observable for which higher order terms may be significant is the rotational constant B; these terms are expected to be considerably smaller than the second order contribution and will depend on the details of the potential surface. The estimated uncertainties for the CBO results with the potentials considered here are given in tables 2 and 4.

2.1.1.6 Effect of centre of mass shift

The coordinate system used in the CBO calculations (figure 1) is based on the vector from the diatom centre of mass to the argon atom and the angular coordinate θ is defined relative to this. In order to perform calculations for two different isotopic species of a complex (for example Ar·HCl and Ar·DCl) it is necessary to assume that the intermolecular potential is, in some sense, isotope independent. The most commonly used model in the literature supposes that the potential is the same for the same geometry; that is, the same Ar-Cl and Ar-H(D) distances. However, because the diatom centre of mass is different for the two isotopic species, a particular geometry is described by different (R,θ) coordinates for the two isotopes. Thus to allow for the centre of mass shift, it is necessary to transform the potential relative to some reference isotope before doing the calculations.

Several methods of performing the centre of mass shift have been proposed. Holmgren et al. [5] in their BOARS calculation used a Taylor expansion in powers of δ/R, where δ is the centre of mass shift. We have used a method due to Liu et al. [13], in which the transformed potential is evaluated by Gauss-Legendre quadrature at each value of R. This method is both more accurate and simpler to program than the earlier method of Kreek and LeRoy [14].

One effect of the centre of the mass shift is to introduce high order Legendre terms into the potential, even if the potential for the reference isotope is truncated at a low order. Thus the HWK potential is written in the form

$$V(R,\theta) = \sum_{k=0}^{k_{max}} V_k(R) P_k(\cos\theta) \qquad (53)$$

Table 3. Effect of centre of mass shift on spectroscopic parameters for $Ar\cdot D^{35}Cl$ on the HWK potential, using $b_{max} = 3$.

k_{max}	E/cm^{-1}	B/MHz	D_J/kHz	$\langle P_2(\cos\theta)\rangle$	D_θ/p.p.m.
No cm shift	-135.883	1634.953	17.76	0.53773	15.83
2	-136.407	1662.356	18.93	0.52648	20.04
3	-136.550	1663.260	18.74	0.53028	18.71
4	-136.544	1663.254	18.74	0.53007	18.74

with the series truncated at $k_{max} = 2$ for the Ar·HCl isotope. In the transformed potential for Ar·DCl, however, there are contributions from $k = 3,4$ etc. terms. To assess the importance of these higher order terms, we have carried out CBO calculations for $Ar\cdot D^{35}Cl$ on the HWK surface, truncating the transformed potential at several values of k_{max}, and the

results are shown in table 3.

The initial effect of the centre of mass shift is dramatic, changing the rotational constant by about 30 MHz and the other parameters by less important amounts. The $P_3(\cos\theta)$ terms is also important, though fairly close to the limit of reliability of the calculations, whereas the $P_4(\cos\theta)$ term may be neglected for most purposes. The other calculations in this chapter have truncated the series for the transformed potential at $k_{max} = 3$.

2.1.1.7 Relative importance of perturbation terms

The relative sizes of various terms contributing to spectroscopic parameters have been evaluated for Ar·H^{35}Cl and Ar·D^{35}Cl on the HWK potential, and the results are shown in table 4.

The non-adiabatic terms in table 4 are the major terms omitted in the BOARS approach and it may be seen that they make an important contribution (>10 MHz) to the rotational constants. Because the second order non-adiabatic contributions to B are so large, we have also calculated the third order corrections, which are approximately -1 MHz in magnitude. It is clear that adiabatic approximations to the rotational constant may be considerably in error. The non-adiabatic corrections to $\langle P_2(\cos\theta)\rangle$ are small for this potential, although corrections up to 0.08 in the expectation value have been found for other potentials (cf. table 2). The very small non-adiabatic correction to D_θ for Ar·HCl is due to a fortuitous cancellation of terms, as may be seen from the Ar·DCl result, where the non-adiabatic term contributes over 20 per cent of the total.

The Coriolis term also makes important contributions to the

Table 4. Magnitude of perturbation terms for Ar·HCl on the HWK potential, using $b_{max} = 4$. Terms marked - have not been calculated, but are believed to be very small.

	E/cm^{-1}	B/MHz	D_J/kHz	$\langle P_2(\cos\theta)\rangle$	D_θ/p.p.m.
		$Ar\cdot H^{35}Cl$			
Zeroth order	-126.800	1678.81	18.57	0.36971	20.78
1st order $\hat{H}_{na}$	0	0	0	0.00555	0.05
2nd order $\hat{H}_{na}$	-1.339	15.006	2.08	-0.01285	-
2nd order $\hat{H}_{cor}$	0	-5.496	0.07	0	3.63
$\hat{H}_{cor}/\hat{H}_{na}$ cross term	0	-0.269	-	0	-
Total	-128.139	1688.051	20.72	0.36240	24.47
Uncertainty	0.3	3.0	0.5	0.002	2.0
		$Ar\cdot D^{35}Cl$			
Zeroth order	-135.609	1665.07	17.16	0.52791	14.93
1st order $\hat{H}_{na}$	0	0	0	0.01295	-4.51
2nd order $\hat{H}_{na}$	-0.942	11.760	1.88	-0.01041	-
2nd order $\hat{H}_{cor}$	0	-13.054	-0.31	0	8.29
$\hat{H}_{cor}/\hat{H}_{na}$ cross term	0	-0.511	-	0	-
Total	-136.551	1663.269	18.74	0.53045	18.71
Uncertainty	0.3	3.0	0.5	0.002	2.0

rotational constant and to D_θ. The Coriolis contribution to B is usually in the range 5 to 15 MHz and is always negative in sign, since the Coriolis effect always depresses the energy for the rotating molecule. This result disagrees with that of Holmgren et al. [12], who found that the Coriolis contribution to B was smaller than here and, for the case of Ar·DCl on the DG potential, actually positive in sign. Their result is not physically reasonable, since the $K = \pm 1$ perturbing

states lie above the ground state. The inaccuracy probably arose because of numerical instability in their procedure for determining B, by a fit of total energy to a power series in J(J+1).

Howard [15] has recently pointed out that there is a Coriolis contribution to the quadrupole coupling constant itself, as well as to its centrifugal distortion constant. The hamiltonian for nuclear quadrupole coupling $\hat{H}_{quad}$ has matrix elements off-diagonal in the projection quantum number K, due to perpendicular components of the nuclear quadrupole coupling constant. The second order effect of these matrix elements is expected to be very small, but the cross-term between the perpendicular quadrupole and $\hat{H}_{cor}$ may be significant. Howard [15] has shown that this effect will appear in the spectrum with the same J- and M-dependence as the parallel quadrupole coupling, so that the quadrupole coupling constant for the complex is given by

$$eQq = eQq^{HCl}\left[\langle P_2(\cos\theta)\rangle + \frac{1}{\sqrt{3}}\langle 001|C_{21}+C_{2-1}|000\rangle\right] \qquad (54)$$

where the $C_{\ell m}$ operators are the renormalised spherical harmonics $(4\pi(2\ell+1))^{1/2}\ Y_{\ell m}$. An effective angular expectation value may thus be defined

$$\langle P_2(\cos\theta)\rangle_{eff} = \langle P_2(\cos\theta)\rangle + \frac{1}{\sqrt{3}}\langle 001|C_{21}+C_{2-1}|000\rangle. \qquad (55)$$

The correction term may be visualised as due to the fact that $\langle P_2(\cos\theta)\rangle$ measures the projection of eQq^{HCl} onto the $\underline{R}$ vector of the complex whereas the experiment measures the projection onto the a-inertial axis. These axes coincide for the linear and $\theta = \pi/2$ configurations of the complex, but differ slightly for intermediate angles. In Ar·HCl, the

angle between the $\underline{a}$ and $\underline{R}$ axes rises to a maximum of about 7×10^{-4} radians for $\theta=\pi/4$. We have evaluated the correction term of equation (55) for the HWK potential and find it to be 0.00035 for $Ar\cdot H^{35}Cl$ and 0.00062 for $Ar\cdot D^{35}Cl$. For most purposes this may be neglected, and it has been omitted from the expectation values of $P_2(\cos\theta)$ quoted elsewhere in this chapter.

2.1.2 Reversed adiabatic method

The CBO method described above provides an efficient means of calculating spectroscopic constants for atom-diatom van der Waals complexes, and is much more accurate than the original BOARS treatment of Holmgren et al. However, for some potentials the nonadiabatic correction terms are large, and it is clear that the perturbation series does not converge quickly. For such potentials, an alternative theoretical approach is required.

2.1.2.1 Theory

In the adiabatic approximation, a near-diagonal representation was obtained by expanding the total wavefunction in terms of angular functions $\{\phi_b(\theta;R)\}$ which diagonalised the bending hamiltonian. This is appropriate when the angular functions concerned vary slowly with the intermolecular distance R. When this is not the case, an obvious alternative is to expand the total wavefunction in terms of radial functions which diagonalise a suitably chosen stretching hamiltonian. This will give a near-diagonal representation if the stretching functions obtained vary slowly with angle θ.

The total hamiltonian is therefore factorised

$$\hat{H} = \hat{H}_{stretch} + b\hat{j}^2 + \hat{H}_j + \hat{H}_{rot} + \hat{H}_{cor} \qquad (56)$$

where

$$\hat{H}_{stretch} = -\frac{\hbar^2}{2\mu}\frac{\partial^2}{\partial R^2} + V(R,\theta), \qquad (57)$$

$$\hat{H}_j = \frac{\hbar^2}{2\mu R^2}(\hat{j}^2 - 2\hat{j}_z^2) \qquad (58)$$

and $\hat{H}_{rot}$ and $\hat{H}_{cor}$ are as defined previously (equations (5) and (6)). The total wavefunction is expanded

$$\psi_{sb} = \sum_{s'} \chi_{s'}(R;\theta)\ \phi_{sb;s'}(\theta) \tag{59}$$

where the stretching wavefunctions $\{\chi_{s'}(R;\theta)\}$ depend parametrically upon θ and are defined by

$$\left[\hat{H}_{stretch} - U_{s'}^{RBO}(\theta)\right]\chi_{s'}(R;\theta) = 0\ . \tag{60}$$

The functions $U_{s'}^{RBO}(\theta)$ form a series of effective potentials for the bending motion of the complex. The eigenfunctions of $\hat{H}^{RBO} = \hat{H}_{stretch} + b\hat{j}^2$ are then solutions of the set of coupled differential equations

$$\left[b\hat{j}^2 + U_{s''}^{RBO}(\theta) - E_{sb}\right]\ \phi_{sb;s''}(\theta) = \sum_{s'}\left[m_{s'',s'}(\theta) + n_{s'',s'}(\theta)\frac{d}{d\theta}\right]\ \phi_{sb;s'}(\theta) \tag{61}$$

where $$m_{s'',s'}(\theta) = -b\int \chi_{s''}(R;\theta)\ \hat{j}^2\ \chi_{s'}(R;\theta)\ dR \tag{62}$$

and $$n_{s'',s'}(\theta) = -2b\int \chi_{s''}(R;\theta)\ \frac{d}{d\theta}\ \chi_{s'}(R;\theta)\ dR\ . \tag{63}$$

The reversed Born-Oppenheimer (RBO) solution is then obtained by neglecting all the terms on the right hand side of equation (61)

$$\psi_{sb}^{RBO} = \chi_s(R;\theta)\ \phi_{sb}^{RBO}(\theta) \tag{64}$$

$$\left[b\hat{j}^2 + U_s^{RBO}(\theta) - E_{sb}^{RBO}\right]\ \phi_{sb}^{RBO}(\theta) = 0 \tag{65}$$

and the reversed adiabatic (RA) approximation is obtained when the diagonal

term $m_{ss}(\theta)$ is included

$$\psi_{sb}^{RA} = \chi_s(R;\theta)\ \phi_{sb}^{RA}(\theta) \tag{66}$$

$$\left[\hat{bj}^2 + U_s^{RA}(\theta) - E_{sb}^{RA}\right]\ \phi_{sb}^{RA}(\theta) = 0 \tag{67}$$

where $$U_s^{RA}(\theta) = U_s^{RBO}(\theta) - m_{ss}(\theta)\ . \tag{68}$$

It would be possible to include the off-diagonal nonadiabatic terms, as well as the neglected terms in equation (56), by perturbation theory, although there are special numerical problems which do not arise in the CBO case. However, as will be seen below, the RA approximation is itself sufficiently accurate for calculating the spectroscopic observables for most potentials, and the additional complexity introduced by the non-adiabatic terms is not justified.

2.1.2.2 Matrix elements

The reversed adiabatic correction term $m_{ss}(\theta)$ is given by [8]

$$m_{ss}(\theta) = \langle\chi_s|-b\hat{j}^2|\chi_s\rangle = b\sum_{s'}\frac{|\langle\chi_s|\partial V/\partial\theta|\chi_{s'}\rangle|^2}{\left[U_s^{RBO}(\theta)-U_{s'}^{RBO}(\theta)\right]^2} \tag{69}$$

where the integrations are over R only. The infinite summation over stretching states could be performed by explicitly calculating the excited state wavefunctions and then summing matrix elements, but it is more convenient to use the differential equation method of Appendix 1, which allows all contributions to be included in a single step.

In the RA approximation, $U_s^{RBO}(\theta)$ and other functions are calculated

on a grid of θ values, but matrix elements are then required between bending functions expressed in terms of spherical harmonics. It is thus more convenient to convert the pointwise functions into expansions in Legendre polynomials, since standard angular momentum techniques can then be applied. This is most simply achieved if the pointwise functions are evaluated at Gauss-Legendre quadrature points. For example, if

$$U_s^{RBO}(\theta) = \sum_k U_k \, P_k(\cos\theta) \tag{70}$$

the coefficients U_k are given by

$$U_k = \int_{-1}^{1} (k+\tfrac{1}{2}) \, U_s^{RBO}(\theta) \, P_k(\cos\theta) \, d\cos\theta \approx \sum_i (k+\tfrac{1}{2}) \, U_s^{RBO}(\arccos x_i) \, P_k(x_i) \, w_i \tag{71}$$

where the w_i and x_i are weights and abscissae for N-point Gaussian quadrature [16].

The operators $\hat{H}_j$ and $\hat{H}_{cor}$ are numerically difficult to deal with in the reversed adiabatic formulation, although it would be possible to expand the functions $\{\chi_s(R;\theta)\}$ in terms of eigenfunctions of $\hat{j}^2$ at each intermolecular distance R, and then calculate the matrix elements using standard techniques. In the present work the small operator $\hat{H}_j$ has been neglected, and the effect of $\hat{H}_{cor}$ on the spectroscopic observables has been taken from ordinary BO calculations. This procedure gives accurate results, as will be shown in section 2.1.2.5 below.

2.1.2.3 Calculation of spectroscopic parameters

(1) Rotational constant B

As in the CBO case, there are contributions to B from both $\hat{H}_{rot}$ and

$\hat{H}_{cor}$. In the reversed adiabatic approximation, when both $\hat{H}_j$ and $\hat{H}_{cor}$ are neglected, the contribution from $\hat{H}_{rot}$ is simply

$$B_{rot} = \int \phi_{00}^{RA}(\theta)\ B(\theta)\ \phi_{00}^{RA}(\theta)\ \sin\theta\ d\theta \tag{72}$$

where $$B(\theta) = \int \chi_0(R;\theta)\ (\hbar^2/2\mu R^2)\ \chi_0(R;\theta)\ dR\ . \tag{73}$$

This can then be corrected by the Coriolis term taken from the BO approximation. This term should have essentially the same value in the BO and RA approaches since it arises from the same term in the full hamiltonian. The expression used is thus

$$B = B_{rot} + B_{cor}^{BO} \tag{74}$$

(2) Centrifugal distortion constant D_J

A formal expression for D_J in the reversed adiabatic approximation, neglecting all perturbation terms except $\hat{H}_{rot}$, may be written

$$D_J\ J^2(J+1)^2 = \sum_{b\neq 0} \frac{|\langle 00|\hat{H}_{rot}|0b\rangle|^2}{E_{0b}^{RA} - E_{00}^{RA}} + \sum_{s\neq 0}\sum_{b} \frac{|\langle 00|\hat{H}_{rot}|sb\rangle|^2}{E_{sb}^{RA} - E_{00}^{RA}}\ . \tag{75}$$

The first term is readily evaluated by summing matrix elements, and the summation converges rapidly. The second term does not converge very fast as it stands, but may be very accurately approximated by

$$\int \phi_{00}^{RA}(\theta)\ D_J(\theta)\ \phi_{00}^{RA}(\theta)\ \sin\theta\ d\theta \tag{76}$$

where $D_J(\theta)$ is the pseudo-diatomic centrifugal distortion constant evaluated at fixed angle

$$D_J(\theta)\ J^2(J+1)^2 = \sum_{s\neq 0} \frac{|\langle \chi_0(R;\theta)|\hat{H}_{rot}|\chi_s(R;\theta)|^2}{U_s^{RA}(\theta) - U_0^{RA}(\theta)} \qquad (77)$$

This expression can be evaluated efficiently using the differential equation method of Appendix 1, ensuring convergence of the summation.

There are thus two contributions to the centrifugal distortion constant, and these have a clear physical interpretation. The dominant contribution corresponds to the second term of equation (75), and is simply the fixed-angle centrifugal distortion constant of equation (77) averaged over the bending motion of the complex. However, there is also a smaller contribution arising from the distortion of the angular wavefunction as the complex rotates.

3) Angular expectation values $\langle P_1(\cos\theta)\rangle$ and $\langle P_2(\cos\theta)\rangle$.

These are given by the expectation values over the bending wavefunction

$$\langle P_1(\cos\theta)\rangle = \int \phi_{00}^{RA}(\theta)\ P_1(\cos\theta)\ \phi_{00}^{RA}(\theta)\ \sin\theta\ d\theta \qquad (78)$$

and analogously for $\langle P_2(\cos\theta)\rangle$.

4) Angular centrifugal distortion constant D_θ

The expression for D_θ may be written (cf. equation (52))

$$D_\theta\ J(J+1) = -2 \sum_{sb} \frac{\langle 00|P_2(\cos\theta)|sb\rangle\ \langle sb|\hat{H}_{rot}|00\rangle}{E_{sb}^{RA} - E_{00}^{RA}} + \text{Coriolis term} \qquad (79)$$

However, at each value of θ there are only diagonal matrix elements of $P_2(\cos\theta)$ between the stretching wavefunctions $\{\chi_s(R;\theta)\}$, so that the expression for D_θ reduces to

$$D_\theta\ J(J+1) = -2 \sum_{b\neq 0} \frac{\langle 00|P_2(\cos\theta)|0b\rangle\ \langle 0b|\hat{H}_{rot}|00\rangle}{E^{RA}_{0b} - E^{RA}_{00}} + \text{Coriolis term}. \qquad (80)$$

This summation is again quickly convergent. As before, it is simpler to take the Coriolis term from BO calculations than to calculate it in the RA formulation.

2.1.2.4 Convergence

Most aspects of the convergence of RA calculations are the same as for CBO calculations; for Ar·HCl and Ar·DCl calculations have been performed using $j_{max} = 7$ and solving the radial equations on a grid of 400 equally spaced points between 3.0 Å and 6.0 Å. However, there remain two degrees of freedom which must be converged.

1) We have investigated the convergence of reversed adiabatic calculations with respect to the number of Gaussian quadrature points used in solving the angular equations, using an ab initio potential due to Vliegenthart and Rozendaal [17] (VR potential, figure 5). This potential has been chosen because the position of the radial minimum $R_m(\theta)$ varies particularly fast with θ, which is expected to result in slower convergence of the Gaussian quadratures than is found for most other potentials. The results of these calculations are shown in table 5; it may be seen that convergence is essentially complete for N = 10, and this value of N has been used in all the other RA calculations presented here.

2) The convergence of D_J and D_θ with respect to the basis set of bending states (equations (75) and (80)) has also been investigated, and the results are shown in table 6. $b_{max} = 3$ has been used in

all subsequent calculations.

Table 5. Convergence of RA calculations with respect to number of Gaussian quadrature points, using VR potential. The Coriolis term in B is omitted.

N	B/MHz	$\langle P_2(\cos\theta)\rangle$
4	1610.52	0.1959
6	1610.57	0.2430
8	1610.74	0.2391
10	1610.67	0.2401
12	1610.68	0.2400

Table 6. Convergence of RA calculations with respect to basis set of bending states, using HWK potential

	Ar·HCl		Ar·DCl	
b_{max}	D_J/kHz	$D_\theta/10^{-6}$	D_J/kHz	$D_\theta/10^{-6}$
0	18.34	0.00	17.99	0.00
1	19.72	18.63	18.33	13.58
2	20.14	29.64	18.54	22.60
3	20.16	30.28	18.56	23.72
4	20.16	30.28	18.56	23.77

2.1.2.5 Comparison with previous calculations

Reversed adiabatic calculations have been performed using the HWK potential [5] (figure 3), and are compared with the results of Grabenstetter and Le Roy [4], Kidd et al. [6], and with CBO results in table 7.

Table 7. Comparison of methods using HWK potential

	B/MHz	D_J/kHz	$\langle P_2(\cos\theta)\rangle$	$D_\theta/10^{-6}$
	Ar·HCl			
CBO	1688 ±3	20.7±0.5	0.3624±0.002	24.5±4.0
RA	1694.1±3	20.2±0.5	0.3638±0.002	30.3±4.0
Secular determinant [4]	1691 ±2	20 ±3	-	-
Close coupling [6]	1690.8	20.2	-	-
	Ar·DCl			
CBO	1663±3	18.7±0.5	0.5305±0.002	18.7±4.0
RA	1666±3	18.6±0.5	0.5332±0.002	23.8±4.0

It may be seen that RA calculations are of approximately the same accuracy as CBO calculations for Ar·HCl on this potential. The accuracy of RA calculations improves from Ar·HCl to Ar·DCl, since the neglected coupling terms involve the rotational constant of the diatomic molecule; CBO calculations, by contrast, are less accurate for DCl complexes, because the states coupled by the nonadiabatic terms are closer together than in HCl complexes.

In conclusion, the CBO method is often more accurate than the RA method, but it is less stable; the CBO method breaks down for some potentials, whereas the RA approximation always gives reasonably accurate

spectroscopic constants. The CBO method tends to break down when the equilibrium angle changes quickly with R; this is the case for some of the potentials considered in chapters 4 and 5, where the preferred angle is $\theta = 0^{o}$ at $R = R_e$, but becomes $\theta = 180^{o}$ at smaller values of R. Conversely, the RA method is least accurate when the equilibrium distance $R_m(\theta)$ changes fast with θ.

In the following chapters, the CBO method has been used where possible, but the RA method has been used in "difficult" cases.

2.2 Linewidth calculations

The quantum mechanical theory of rotational line broadening for a dilute solution of a diatomic gas in a bath of structureless perturbers is well understood [18], but for systems with reduced masses approaching those of Ar+HCl fully quantal close coupling calculations are prohibitively expensive. Various angular momentum decoupling approximations, particularly the coupled states approximation [19,20], have been applied to the calculation of line broadening cross sections, but even these are too expensive to use in a least squares procedure to optimize potential parameters. More satisfactory are approaches using curved classical paths for the translational motion, but treating the rotational motion quantally [21,22]; these are reasonably inexpensive and appear to give good results. We have used a modified version of the method of Smith et al. [22], in which some of their approximations have been removed. As will be seen below, the method appears to give reliable results for all but the lowest rotational line, as judged by comparison with coupled states and more sophisticated classical path results. The present method is very much faster than any of the alternatives, producing a complete set of line broadening cross sections for a trial potential surface in less than 10 seconds on an ICL 2980 computer.

In the classical path formulation the cross section for pressure broadening of an isolated spectral line is given in terms of S matrix elements by [21]

$$\sigma_{jj'}(T) = (k_B T)^{-2} \int_0^\infty \int_0^\infty \sigma_{jj'}(b,E)\, \exp(-E/k_B T)\, 2\pi b\, db\, dE, \qquad (81)$$

$$\sigma_{jj'}(b,E) = 1 - \sum_{\substack{m_\alpha m_\beta \\ m'_\alpha q\, m'_\beta}} (-1)^{m_\beta - m_\alpha} \begin{pmatrix} j & K & j' \\ m_\alpha & q & -m'_\alpha \end{pmatrix} \begin{pmatrix} j & K & j' \\ m_\beta & q & -m'_\beta \end{pmatrix}$$

$$\times \langle j'm'_\alpha | S^*(b,E) | j'm'_\beta \rangle \langle jm_\alpha | S(b,E) | jm_\beta \rangle, \qquad (82)$$

where T is the temperature, j and j' are the rotational quantum numbers of the states connected by the transition, b is the impact parameter for the collision, E is the translational energy, the summations over $m_{\alpha,\beta}$ and $m'_{\alpha,\beta}$ are over all possible projections of j and j' onto a spaced-fixed axis, and K is the tensor order of the transition (1 for far infrared spectra, 2 for Raman spectra).

The problem of calculating line broadening cross sections thus reduces to that of calculating classical path S matrices. Following Smith et al. [22] we express the S matrix for each classical trajectory as the complex exponential of a phase integral matrix $\underline{\eta}(b,E)$

$$\underline{S}(b,E) = \exp(i\underline{\eta}(b,E)), \tag{83}$$

$$\langle jm|\eta|j'm'\rangle = \int_{-\infty}^{\infty} \langle jm|V(\underline{R}(t))|j'm'\rangle \exp(i\omega_{jj'}t)\, dt, \tag{84}$$

where $\omega_{jj'}$ is the angular velocity associated with the energy difference between states $|jm\rangle$ and $|j'm'\rangle$, $V(\underline{R})$ is the intermolecular potential and $\underline{R}(t)$ is the time-dependent position vector describing the classical trajectory for the collision. This expression is just the leading term in the Magnus expansion [23] of the proper time-ordered exponential; further terms involve commutators between potentials at different times and are believed to be small for atom-diatom collisions [24].

Next, the peaking approximation is made [22]; this involves neglecting the time-dependence of the angle between $\underline{R}(t)$ and the space-fixed quantisation axis, and has the result of making the $\underline{\eta}$ matrix diagonal in m

$$\langle jm|\eta|j'm'\rangle = \sum_k \langle jm|C_{k0}|j'm'\rangle \int_{-\infty}^{\infty} V_k(R(t))\, \cos\omega_{jj'}t\, dt \tag{85}$$

where the C_{kO} are the renormalised spherical harmonics $(4\pi/(2k+1))^{1/2} Y_k^0$, R(t) is the length of the vector $\underline{R}(t)$ and the $V_k(R)$ are Legendre components of the potential

$$V(R,\theta) = \sum_k V_k(R) P_k(\cos\theta) \quad . \tag{86}$$

The S matrix is now also diagonal in m, and equation (82) simplifies to

$$\sigma_{jj'}(b,E) = 1 - \sum_{mm'q} \begin{pmatrix} j & K & j' \\ m & q & -m' \end{pmatrix}^2 \langle j'm' | S^*(b,E) | j'm' \rangle$$

$$\times \langle jm | S(b,E) | jm \rangle \tag{87}$$

It may be noted that this expression involves only <u>diagonal</u> S-matrix elements. Smith et al. [22] next make a series of approximations which enable them to obtain an analytical expression for the S matrix elements. This procedure has advantages for potentials with a simple analytical form of the $V_k(R)$ and with only low order Legendre polynomials $P_k(\cos\theta)$ contributing, but for less restrictive potentials the expressions for the S matrix elements become very complicated. It is then simpler (and more accurate) to calculate the $\underline{\eta}$ matrix exactly from equation (85) and then exponentiate it numerically.

Our program for calculating the line broadening cross sections $\sigma_{jj'}(b,E)$ starts by evaluating R(t) for the centrifugally corrected isotropic potential, using a predictor-corrector algorithm based on Hermite interpolation and the Euler-Maclaurin sum rule [25] to propagate R(t) outwards from the classical turning point; the $V_k(R)$ are then evaluated at a set of up to 128 equally spaced values of t and Fourier transformed using the Cooley-Tukey FFT algorithm [26]. The $\underline{\eta}$ matrix is constructed using exact values for the angular momentum

coupling terms and exponentiated using the identity

$$\exp(i\underline{\eta}) = \underline{X}^{-1} \exp(i\underline{D})\ \underline{X}\,, \tag{88}$$

where $\underline{D}$ is a diagonal matrix defined by

$$\underline{\eta} = \underline{X}^{-1}\ \underline{D}\ \underline{X}\,. \tag{89}$$

The integrations over b and E are then carried out using Gaussian quadrature as described by Kircz et al. [27], which was found to converge more rapidly than simple Gauss-Laguerre or Gauss-Hermite quadrature. In the present work eight-point quadratures were used for both the impact parameter and energy integrals.

For a diatomic molecule with rotational constant b_d, all the phase integrals required for equation (85) are for values of ω_{jj}, which are multiples of $2b_d$. For suitably chosen time steps, therefore, the required Fourier integrals are provided directly by the discrete Fourier transformation without the need for interpolation.

In order to judge the accuracy of the present method, we have compared it with various calculations in the literature for Neilsen and Gordon's potential 52 [21]. Neilsen and Gordon have reported accurate classical path calculations on this surface and Smith et al. [22] have compared their approximation to Neilsen and Gordon's. Goldflam et al. [28] have performed coupled states calculations on this surface for one energy only; these are expected to be accurate to ±5 per cent [20]. The results of the present method are compared with these earlier calculations in table 8. The agreement is good for all transitions except $j = 0 \rightarrow 1$. The present calculations give linewidths slightly below

those of Neilsen and Gordon [21], but the coupled states results suggest that Neilsen and Gordon's results themselves may be somewhat too high.

Table 8. Comparison of rotational line-broadening cross-sections calculated by different methods. All calculations are for surface 52 of Neilsen and Gordon [21].

Line (j→j')	E = 150 K GGK	E = 150 K NG	E = 150 K This work	E = 398 K GGK	E = 398 K NG	E = 398 K This work
	Cross sections at fixed collision energy/Å^2					
0→1	86	98.23	(61.2)	75	79.88	(54.0)
1→2	82	84.91	83.2	54	57.41	50.7
2→3	65	68.61	65.4	46	45.16	42.4
3→4	46	50.92	44.8	35	37.38	34.6
4→5	32	37.17	31.4	-	30.63	28.0
5→6	-	26.37	21.8	-	23.75	22.0

Line (j→j')	NG	SGC	This work
	Cross sections averaged over energy at temperature 300 K		
0→1	74.02	-	(50.9)
1→2	59.16	69.7	56.8
2→3	47.40	51.3	46.6
3→4	38.44	40.2	36.1
4→5	31.48	32.3	29.0
5→6	25.42	26.3	23.5

GGK, coupled states results of Goldflam et al. [28]. NG, classical path results of Neilsen and Gordon [21]. SGC, approximate classical path results of Smith et al. [22].

On the basis of this comparison we believe that the present method provides line broadening cross sections accurate to ±3 $\mathring{A}^2$. However, as will be seen below, the Neilsen-Gordon potential 52 is not realistic and it would be desirable to obtain more accurate calculations on our fitted potentials, to verify that our computational method is still accurate for these.

2.3 Second virial coefficients

Second virial coefficients were evaluated by direct numerical integration of the classical expression

$$B_{12} = \pi N \int_0^\infty \int_{-1}^{1} [1 - \exp(-V(R,\theta)/k_B T)] \, d\cos\theta \, R^2 \, dR. \qquad (90)$$

Quantum corrections were ignored, since they are expected to be small compared to the experimental uncertainties at the temperatures for which data are available (190 K to 480 K for Ar·HCl).

REFERENCES

1. A.M. Dunker and R.G. Gordon, J. chem. Phys. 64, 354 (1976).

2. R.G. Gordon, J. chem. Phys. 51, 14 (1969).

3. R.J. Le Roy, J.S. Carley and J.E. Grabenstetter, Faraday Discus. Chem. Soc. 62, 169 (1977).

4. J.E. Grabenstetter and R.J. Le Roy, private communication.

5. S.L. Holmgren, M. Waldman and W. Klemperer, J. chem. Phys. 67, 4414 (1977).

6. I.F. Kidd, G.G. Balint-Kurti and M. Shapiro, Faraday Discus. R. Soc. Chem. 71/22 (1981).

7. M. Shapiro, J. chem. Phys. 56, 2582 (1972).

8. M.S. Child, Molecular Collision Theory, Academic Press (1974), p. 89.

9. D.L. Albritton, W.J. Harrop, A.L. Schmeltekopf and R.N. Zare, J. mol. Spectrosc. 46, 25 (1973).

10. J.M. Hutson, J. Phys. B 14, 851 (1981).

11. J.O. Hirschfelder, W. Byers Brown and S.T. Epstein, Adv. quant. Chem. 1, 255 (1964).

12. S.L. Holmgren, M. Waldman and W. Klemperer, J. chem. Phys. 69, 1661 (1978).

13. W.-K. Liu, J.E. Grabenstetter, R.J. Le Roy and F.R. McCourt, J. chem. Phys. 68, 5028 (1978).

14. H. Kreek and R.J. Le Roy, J. chem. Phys. 63, 338 (1975).

15. B.J. Howard, Molec. Phys. to be published.

16. M. Abramowitz and I.A. Stegun, Handbook of Mathematical Functions, Dover, New York (1964).

17. J.A. Vliegenthart and A. Rozendaal, quoted in reference 6.

18. R. Schafer and R.G. Gordon, J. chem. Phys. 58, 5422 (1973)

19. R. Goldflam and D.J. Kouri, J. chem. Phys. 66, 542 (1977).

20. S. Green, L. Monchick, R. Goldflam and D.J. Kouri, J. chem. Phys. 66, 1409 (1977).

21. W.B. Neilsen and R.G. Gordon, J. chem. Phys. 58, 4131 (1973); 58, 4149 (1973).

22. E.W. Smith, M. Giraud and J. Cooper, J. chem. Phys. 65, 1256 (1976); E.W. Smith and M. Giraud, J. chem. Phys. 71, 4209 (1979).

23. W. Magnus, Commun. pure appl. Math. 7, 649 (1954).

24. C. Boulet and D. Robert, Chem. Phys. Lett. 60, 162 (1978).

25. A. Ralston and P. Rabinowitz, A First Course in Numerical Analysis, second edition, McGraw-Hill (1978), pp. 224-225.

26. J.W. Cooley and J.W. Tukey, Math. Comput. 19, 297 (1965).

27. J.G. Kircz, G.J.Q. van der Peijl, J. van der Elsken and D. Frenkel, J. chem. Phys. 69, 4606 (1978).

28. R. Goldflam, S. Green and D.J. Kouri, J. chem. Phys. 67, 4149 (1977).

CHAPTER 3

THE INTERMOLECULAR POTENTIAL OF Ar·HCl

CHAPTER 3

THE INTERMOLECULAR POTENTIAL OF Ar·HCl

The most thoroughly studied of the rare gas -hydrogen halide systems is Ar·HCl, which has been investigated using several different experimental methods. In this chapter, the available experimental data are discussed with a view to assigning uncertainties for use in least squares fitting. The data are then used to test various potentials which have been proposed in the literature. Finally, simultaneous least squares fits to all the useful experimental data are presented and several new potentials are obtained which fit all the existing experimental results.

3.1 Experimental data

3.1.1 Molecular beam spectra

Novick et al. [1,2] and Hutson and Howard [3] have obtained microwave and radiofrequency spectra of the ground vibrational states of the Ar·HCl and Ar·DCl van der Waals complexes. The important quantities obtained from the spectra for each isotope are the rotational and centrifugal distortion constants, the angular expectation values $\langle P_1(\cos\theta)\rangle$ and $\langle P_2(\cos\theta)\rangle$, and the angular centrifugal distortion constant D_θ.

All the spectroscopic constants for the Ar·HCl and Ar·DCl complexes can be measured more accurately than they can be calculated, so that the weights given to the spectroscopic observables in the least squares fits (table 2) are based on estimates of the computational accuracy. The uncertainty of ±0.002 in the expectation values of $P_2(\cos\theta)$ is based on the comparison of expectation values obtained

from chlorine and deuterium quadrupole coupling constants; for $\langle P_1(\cos\theta)\rangle$, obtained from the dipole moments, the uncertainties are larger because of contributions from induced moments and charge transfer.

As discussed in the Introduction, there are slight differences between the intermolecular potentials for Ar·HCl and Ar·DCl because of the different zero point vibrational amplitudes in HCl and DCl. This is expected to have a significant effect on the observed rotational constant for Ar·DCl, and this quantity has accordingly been omitted from the least squares fits described in this chapter.

3.1.2 Rotational linewidths

Cross sections for pressure broadening of $j \rightarrow j + 1$ pure rotational lines of HCl by Ar have been measured by van Aalst et al. [4] for $j = 0$ to 5 at temperatures of 125 K, 175 K and 300 K, and by Frenkel et al. [5] for $j = 6$ to 9 at 162.5 K. Error estimates for these measurements have been given in [4] and [6]. In most cases the experimental errors are greater than the ± 3.0 Å^2 error in the linewidth calculations and have been used without modification in the least squares fits. Where the experimental errors are given as less than ± 3.0 Å^2, the latter value has been used.

Van der Peijl et al. [7] have measured cross sections for pressure broadening of HCl pure rotational Raman lines by Ar at 295 K, but the data are considerably inferior to the far infrared cross sections. Linewidths were measured under conditions where HCl self broadening was significant (HCl partial pressure 0.99 atm) and the Ar + HCl cross sections were obtained by measuring linewidths at Ar partial pressures

of zero, 9.71 atm and 19.24 atm; the Ar·HCl cross sections were then obtained from the gradient of linewidth with respect to Ar pressure, which was not accurately determined. The experimental uncertainties quoted in [7] appear to be unreasonably optimistic; we have used twice the quoted uncertainties in the least squares fits and still obtain poor agreement with these experiments. It is likely that the experiments, rather than the calculations, are at fault, since the Raman cross sections are incompatible with the far infrared cross sections, although the two effects should probe similar features of the anisotropic potential. Indeed, the cross sections for the Raman and far infrared linewidths are simply different averages over the same elastic S matrix elements (equation (82) of chapter 2).

Our computational method is not accurate for the lowest rotational line in either the far infrared or the Raman spectra and these data have been omitted from our fits.

3.1.3 Second virial coefficients

The mixed second virial coefficient B_{12} for Ar + HCl mixtures has been measured by Schramm and Leuchs [8] at temperatures from 190 K to 480 K; they have given the accuracy of their measurements as ranging from ± 7 cm^3 mol^{-1} at 190 K to ± 5 cm^3 mol^{-1} at 480 K and we have adopted these error estimates.

3.1.4 Molecular beam scattering

Farrar and Lee [9] have measured total differential cross sections for Ar + HCl collisions at an energy of about 620 cm^{-1}. They did not

resolve diffraction oscillations, but did observe a single damped rainbow maximum. They interpreted their data using a purely isotropic potential with a well depth of 133 cm^{-1} and equilibrium distance 400 pm.

Unfortunately, it is not possible to include the differential cross sections directly in the least squares fits in a satisfactory way, since the computing time required to perform the calculation in the presence of anisotropy is prohibitive. However, Buck and McGuire [10] have shown that the anisotropy shifts the position of the rainbow maximum only slightly, so that Farrar and Lee's estimate of the isotropic well depth should be fairly reliable. We have included this information in our least squares fits by introducing an isotropic well depth of 133 ± 4 cm^{-1} as a data point.

3.1.5 Other data

Various features in the spectra of bulk phase Ar + HCl mixtures have been attributed to Ar·HCl complexes: Rank et al. [11] and Miziolek and Pimentel [12] have observed such spectra near the HCl fundamental stretching frequency, and Boom and van der Elsken [13] have observed Ar·HCl in the near infrared around 30 cm^{-1}. However, all these spectra are at low resolution, and cannot be conclusively assigned. They are thus of little use in determining the anisotropic potential.

Cross sections for pressure shifting of HCl pure rotational lines by Ar have been measured [4,14]. The line shifts appear naturally in the classical path formulation of chapter 2 as the imaginary part of the cross sections $\sigma_{jj'}(T)$, but the approximations made there are expected to affect the calculated line shifts more than the corresponding widths [15]. A more accurate (and more expensive) computational

method would be necessary if the line shift data were to be included in the least squares fits.

Leonardi-Cattolica et al. [16] have observed proton spin-lattice relaxation times for HCl in gaseous Ar + HCl mixtures at temperatures from 300 K to 420 K. These relaxation times are dependent on the inelasticity of Ar + HCl collisions in much the same way as the rotational line broadening data [4,5], but in addition are averaged over the HCl rotational quantum number j, and so contain less detailed information than the linewidths. In view of the considerable additional computational effort required to calculate nmr relaxation times, it was decided not to include these data in the least squares fits.

Several authors have observed linewidths and shifts for HCl vibration-rotation lines perturbed by Ar [17]. However, these are affected by the dependence of the intermolecular potential on the HCl vibrational coordinate r, as well as by the anisotropy of the potential, and so have been excluded from the present study.

Polanyi and coworkers [18] have investigated inelastic HCl + Ar collisions at high energies by monitoring infrared emission from a molecular beam of HCl before and after crossing a beam of Ar atoms, and have interpreted their results in terms of an exponential gap law with a single adjustable parameter. However, classical trajectory calculations [19] have demonstrated that these results are not very sensitive to the intermolecular potential.

Piollet-Mariel et al. [20] have very recently measured the intensity variation of HCl rotation-vibration lines with Ar pressure, and have developed a somewhat crude theoretical interpretation of the effect [21]. However, the intensity variation is difficult to measure accurately, and the data currently available do not provide a sensitive probe of the

potential anisotropy.

3.2 Previously proposed potentials

Many intermolecular potentials have been proposed for Ar·HCl, based either on ab initio calculations or on experimental data. However, as will be seen below, none of these potentials adequately reproduces all the experimental data. Several of these potentials will now be considered in detail.

1) Neilsen and Gordon [22] generated a series of Ar·HCl potentials based on simple models of the attractive and repulsive forces in Ar·HCl, and attempted to determine the sensitivity of various relaxation phenomena to the potential parameters. They then varied the potential parameters by hand to obtain an optimum fit to far infrared linewidths [23] and n.m.r. relaxation times [16] for Ar + HCl mixtures. This procedure yielded a series of potentials which gave similar fits to the experimental data. Dunker and Gordon [24] subsequently modified these potentials slightly to improve the fit to the rotational constant of the Ar·HCl complex measured by Novick et al. [1]. Dunker and Gordon's potential I (DG potential, figure 4 of chapter 2) is typical of these, and has been selected for consideration here.

2) Kircz et al. [16] used essentially the same parameterisation of the potential as Neilsen and Gordon, but fitted to more extensive measurements of far infrared linewidths [4,5]. Their potential (KPEF potential, figure 1) is completely different from Neilsen and Gordon's, which serves to demonstrate the danger of fitting to relaxation data alone.

3) Vliegenthart and Rozendaal [25] have recently produced an ab initio potential for Ar·HCl, which they have fitted to an analytic functional form [26]. This potential (VR potential, figure 5 of chapter 2) differs considerably from other theoretical calculations on Ar·HCl [27,28], but is included here because it has several features similar to the potentials obtained by least squares fitting below.

4) Holmgren, Waldman and Klemperer [29] obtained a potential by fitting to the molecular beam spectra of Novick et al. [1,2], using the BOARS method to calculate spectroscopic constants. This potential (HWK potential) is shown in figure 3 of chapter 2.

Calculations of spectroscopic constants have been carried out for these four potentials, and are compared with the experimental data [1-3] in table 1. The HWK potential gives by far the best fit, as would be expected, since it is the only one of the potentials that was fitted to the molecular beam spectra. The DG potential completely fails to reproduce the angular expectation values, because its absolute minimum is at a T-shaped configuration; as will be seen below, the spectra require a linear equilibrium geometry. The VR potential gives rotational constants which are too small by about 4%, indicating that its equilibrium intermolecular distance is too large by about 8 pm, and is not anisotropic enough to reproduce the angular expectation values accurately. Conversely, the KPEF potential has an equilibrium intermolecular separation which is about 13 pm too small, and has too great an anisotropy in the region of the potential well.

Calculations of far infrared line broadening cross sections for these potentials are shown in figure 2. The DG and KPEF potentials give reasonably good fits to the data, since they were determined by fitting

Table 1. Comparison of calculated and observed spectroscopic parameters for previously proposed potentials.

Potential	B/MHz	D_J/kHz	$\langle P_2(\cos\theta)\rangle$	$\langle P_1(\cos\theta)\rangle$	$D_\theta/10^{-6}$
Ar·HCl					
DG	1693.0	38.3	-0.028	0.342	96
KPEF	1790.7	12.9	0.616	0.849	-2
VR	1608.1	35.5	0.240	0.518	21
HWK	1688.1	20.7	0.363	0.688	25
Experiment	1678.511	20.0	0.34058	0.673	23.7
Ar·DCl					
DG	1685.2	49.2	-0.035	0.402	175
KPEF	1791.5	12.1	0.719	0.895	0
VR	1581.4	21.8	0.465	0.754	27
HWK	1663.3	18.7	0.531	0.804	19
Experiment	1657.627	17.1	0.53701	0.833	19.0

to similar information. The HWK potential, which was the only one to fit the molecular beam spectra, gives poor line broadening cross sections, particularly for the high rotational lines. This reflects the fact that the high j linewidths are determined by the characteristics of strong collisions which sample the repulsive wall of the potential, and the HWK potential is nearly isotropic in this region. The VR potential also fails to reproduce the high j linewidths, because it has a much "softer" repulsive wall than the other potentials.

Calculated and observed second virial coefficients for Ar+HCl mixtures are shown in figure 3. Second virial coefficients are principally a measure of the (weighted) volume of the potential well (equation (90) of chapter 2). The HWK potential reproduces the

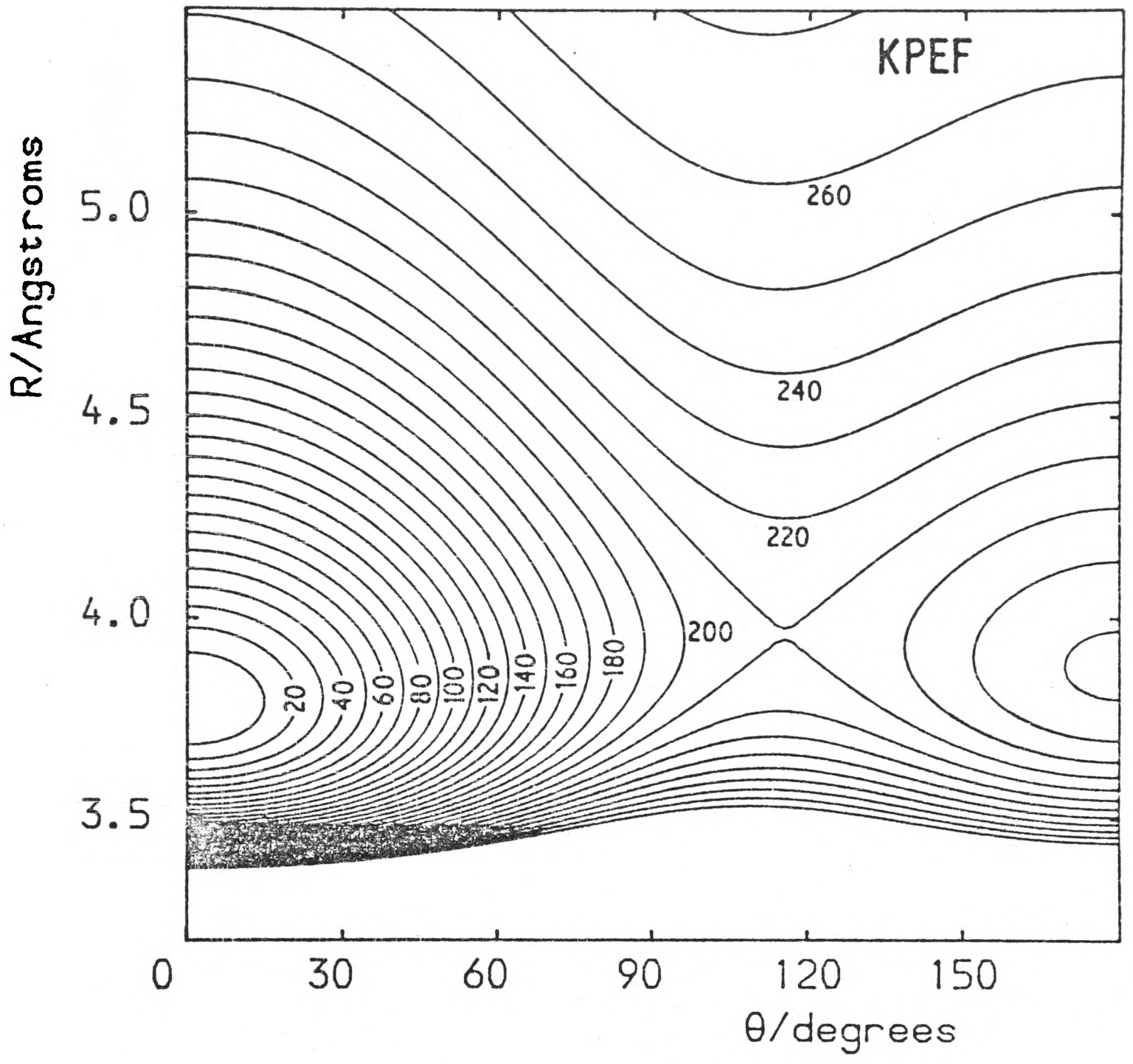

Figure 1. Contour plot of potential A1 of Kircz et al. for Ar·HCl (KPEF potential).
Contours are plotted at 10 cm^{-1} intervals relative to the absolute minimum at -291.3 cm^{-1}.

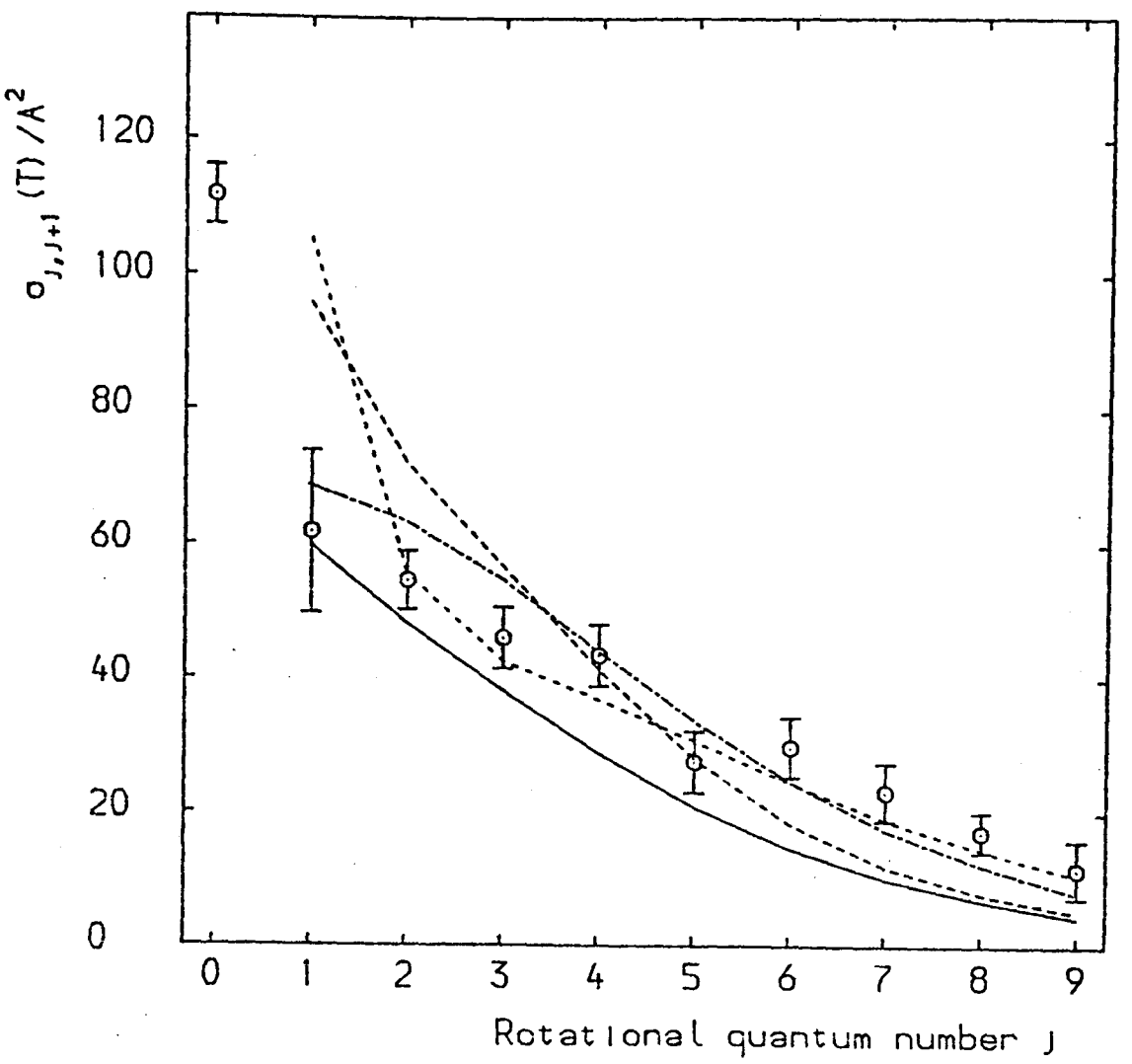

Figure 2. Comparison between experimental and calculated far infrared line broadening cross sections for HCl perturbed by Ar. The points with error bars are the experimental results, and the drawn lines are calculated for previously proposed potentials.

-·-·-·- DG potential

- - - - - KPEF potential

– – – – – HWK potential

——— VR potential

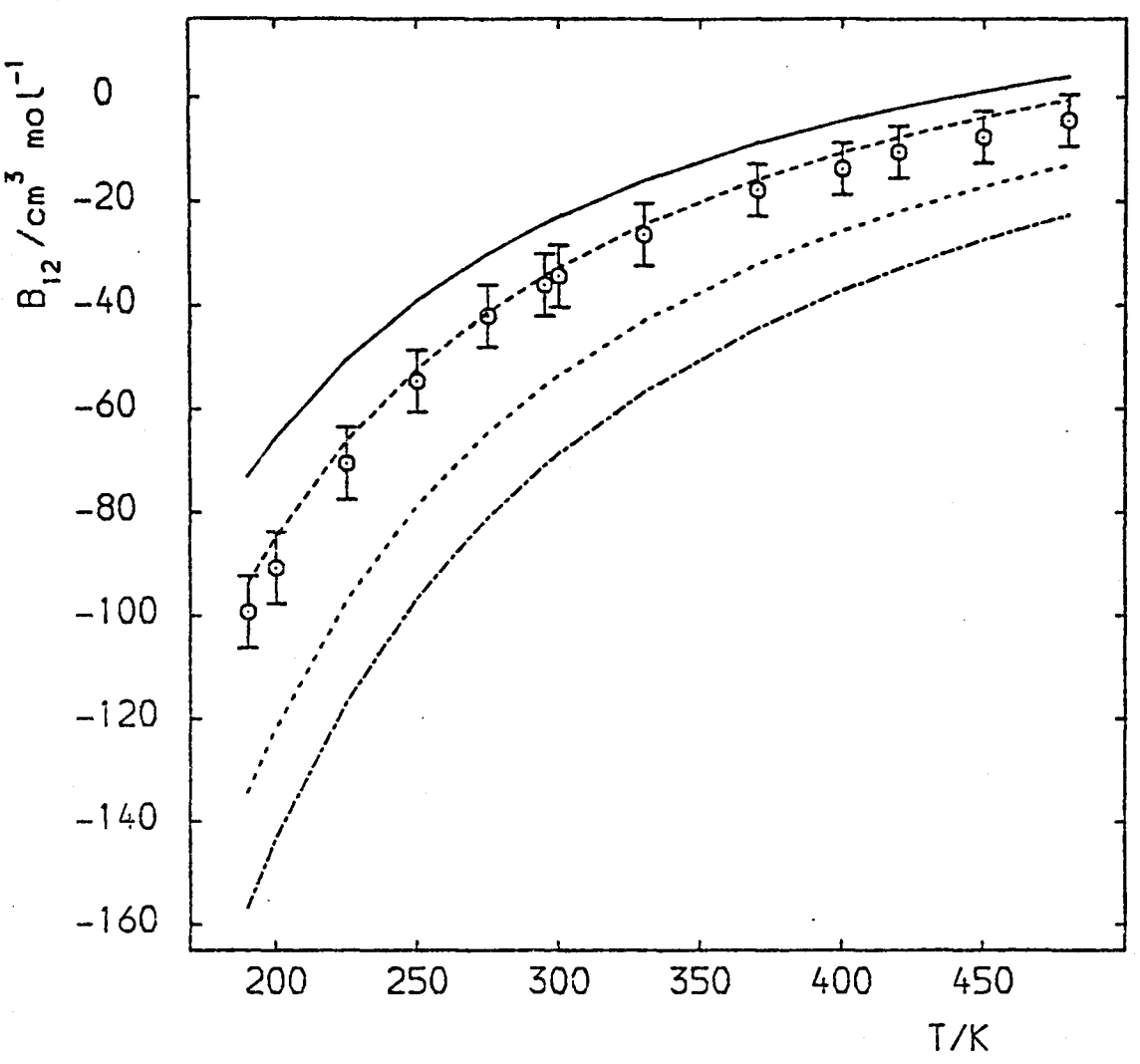

Figure 3. Comparison between experimental and calculated second virial coefficients for Ar+HCl mixtures, using previously proposed potentials. The points with error bars are the experimental results, and the potentials used in the calculations are represented as in figure 2.

experimental data well, but both the DG and KPEF potentials give second virial coefficients that are significantly too negative. For the KPEF potential, this results from the fact that the well around $\theta = 0^{o}$ is too deep. For the DG potential, the minimum is a reasonable depth, but the radial curvature near the minimum is too low, so that the effective volume of the well, as measured by the configuration integral, is too great. This low curvature is also shown by the spectroscopic centrifugal distortion constants D_J; these are much too large for the DG potential, as shown in table 1. The second virial coefficients calculated for the VR potential are somewhat less negative than the experimental ones, indicating that the VR potential is slightly too shallow.

Thus none of the potentials previously proposed for Ar·HCl reproduces all the experimental data adequately. Only the HWK potential reproduces the molecular beam spectra with any accuracy, and it fails to give the far infrared linewidths correctly. It is therefore desirable to attempt a simultaneous fit to all the data, and the remainder of this chapter is devoted to this.

3.3 Parameterisation of the intermolecular potential

In order to obtain information on intermolecular interactions by least squares fitting to experimental data, it is necessary to parameterise the anisotropic potential. The parameterisation chosen must be flexible enough to approximate the true potential closely in the physically significant regions but simple enough for the potential parameters to be determined from the experimental data. Any choice of parameterisation necessarily forces the fitted potential to conform to certain constraints; thus, when least squares fitting, it is desirable

to try several different functional forms. It is then possible, by comparing the resulting potentials, to see which features of the potential are physically significant and which are merely artifacts of the parameterisation. In this section several functional forms that we have used to describe the anisotropic potential are discussed.

All the potential parameterisations discussed below will be based in some way on a one-dimensional well-shaped function, and it is important that this should be chosen carefully. Many simple functional forms have been proposed, of which the Morse, Lennard-Jones and Buckingham (α - 6) forms are the best known. The Morse potential can be excluded immediately for van der Waals interactions, since it dies off too rapidly at large R, while the Lennard-Jones function has an unrealistic form for the repulsive potential. The Buckingham potential has the correct functional form at both large and small R

$$V(R) = \varepsilon/(\alpha - 6)\left[6\ \exp[\alpha(1-x)] - \alpha x^{-6}\right] \qquad (1)$$

where ε is the well depth, α determines the steepness of the repulsive branch and $x = R/R_m$, where R_m is the radial position of the minimum. However, it has been found for the rare gas pairs that the Buckingham potential cannot simultaneously reproduce both the correct well depth and the correct long-range C_6 coefficient; the C_6 coefficient for a Buckingham (α - 6) potential is given by

$$C_6 = \frac{\varepsilon\alpha R_m^{\ 6}}{(\alpha - 6)} \qquad (2)$$

and for the rare gas pairs is generally predicted to be 50 to 100 per cent too large by a Buckingham potential of the correct depth. As will

be seen below, this problem also arises for the Ar·HCl potential. The situation may be improved by adding terms in R^{-8} and R^{-10}, but the potential then becomes rather cumbersome, with too many variable parameters for our purpose. A more successful functional form has been proposed by Maitland and Smith [30]; their potential is based on the Lennard-Jones function, but the exponent of the repulsive wall is allowed to vary with R

$$V(R) = \varepsilon/(n-6)[6x^{-n} - nx^{-6}], \tag{3}$$

where

$$n = m + \gamma(x-1).$$

The effective long-range C_6 coefficient is again determined by ε and R_m

$$C_6 = \varepsilon R_m^{\,6} \tag{4}$$

but is considerably lower than for a Buckingham potential of the same depth and reproduces the theoretical C_6 coefficient reasonably accurately. The Maitland-Smith potential has proved remarkably successful in reproducing bulk phase [31] and molecular beam glory scattering [32] results for the rare gas pairs, and is likely to be superior to other simple functions in anisotropic systems also. As remarked above, the centrifugal distortion constants D_J of the van der Waals molecules are principally determined by the radial curvature at the potential minimum, which for a Maitland-Smith potential is given by

$$\left(\frac{d^2V}{dR^2}\right)_{R=R_m} = \frac{6\varepsilon m}{R_m^{\,2}}. \tag{5}$$

For Ar·HCl, ε and R_m are determined by other data; thus, in order to gain the necessary flexibility to fit D_J, the repulsive wall parameter m must be optimised. However, the skewing parameter γ does not affect the curvature at the minimum and also has very little effect on the other experimental observables, so that it is not possible to determine γ from a least squares fit to the data currently available. We have fixed γ at 9.0 in the present work, so that for our purposes the Maitland-Smith potential has three variable parameters, ε, R_m and m. The parameters ε and R_m have exactly the same interpretation as for other one-dimensional potentials, while m is analogous to the α parameter of the Buckingham (α - 6) potential and principally determines the curvature at the minimum and hence the spectroscopic centrifugal distortion constants.

3.3.1 Multipole parameterisation

The conventional parameterisation for atom-diatom systems involves writing the potential as a Legendre series

$$V(R,\theta) = \sum_k V_k(R) P_k(\cos\theta). \qquad (6)$$

This is completely general, provided the sum over k is taken to infinity and no restriction is placed on the form of the functions $V_k(R)$. As commonly used, however, the summation is truncated at k = 2 or 3 and the $V_k(R)$ are assumed to have one of the simple well-shaped forms discussed above. As will be seen below, this results in a potential with insufficient flexibility in the repulsive region and with large correlation coefficients between its fitted parameters.

If the multipole parameterisation is truncated at $k = 3$ and each $V_k(R)$ is expressed as a three-parameter Maitland-Smith or Buckingham potential, there are twelve parameters which can be varied independently. For Ar·HCl this proved to be too many to determine from the experimental data and some additional constraints were required. We obtained an eight-parameter potential by floating the four well depths ε_0 to ε_3, the radial position of the isotropic minimum R_{m0} and the isotropic wall parameter m_0, but constraining the anisotropic R_{mk} and m_k to be the same for all $k > 0$, that is $R_{m1} = R_{m2} = R_{m3}$ and $m_1 = m_2 = m_3$.

The leading term proportional to $P_1(\cos\theta)$ in the multipole expansion of the long-range potential varies as R^{-7} rather than as R^{-6} [33]. The radial functions for $V_1(R)$ in the multipole potentials used here were given this long-range behaviour by replacing 6 by 7 throughout equations (1) and (3). This is formally preferable, but makes very little difference to any of the observables.

3.3.2 Four-angle parameterisation

The two quantities most precisely defined by the MBER spectra are the radial position of the equilibrium configuration R_e and the angular curvature of the well near the minimum, but neither of these quantities is immediately obtainable from the parameters of the multipole potential. This has the unfortunate consequence that the fitted parameters of a multipole potential are highly correlated. An alternative approach, which still gives radial coefficients of the Legendre polynomials $V_k(R)$ in a simple form, is to express the potential at each of several angles as a well-shaped function and then at each R interpolate between these angles using Legendre polynomials. The four-angle potential used

here is obtained by specifying the potential at $\theta = 0^{o}$, 60^{o}, 120^{o} and 180^{o} as a Maitland-Smith potential and then interpolating using the first four Legendre polynomials. This gives for the $V_k(R)$

$$18V_0(R) = V(R, 0^{o}) + 8V(R, 60^{o}) + 8V(R, 120^{o}) + V(R, 180^{o}), \quad (7)$$

$$30V_1(R) = 7V(R, 0^{o}) + 16V(R, 60^{o}) - 16V(R, 120^{o}) - 7V(R, 180^{o}), \quad (8)$$

$$18V_2(R) = 8V(R, 0^{o}) - 8V(R, 60^{o}) - 8V(R, 120^{o}) + 8V(R, 180^{o}), \quad (9)$$

$$15V_3(R) = 4V(R, 0^{o}) - 8V(R, 60^{o}) + 8V(R, 120^{o}) - 4V(R, 180^{o}), \quad (10)$$

with $V_k(R) = 0$ for all higher order Legendre components. This is a twelve-parameter potential so that addition constraints are again required to reduce the number of independent parameters to a manageable size. None of the data currently available give reliable information on the shape of the potential near the linear Ar·Cl-H geometry ($\theta = 180^{o}$), so we have obtained a seven-parameter potential by constraining the potential at $\theta = 180^{o}$ to be the same as $\theta = 120^{o}$

$$\varepsilon(180^{o}) = \varepsilon(120^{o}), \; R_m(180^{o}) = R_m(120^{o}), \; m(180^{o}) = m(120^{o}) \quad (11)$$

and also requiring R_m and m to vary in the same way as ε between 0^{o} and 120^{o}, in order to minimise unphysical angular oscillations in the potential

$$\frac{R_m(60^{o}) - R_m(0^{o})}{R_m(120^{o}) - R_m(0^{o})} = \frac{\varepsilon(60^{o}) - \varepsilon(0^{o})}{\varepsilon(120^{o}) - \varepsilon(0^{o})} = \frac{m(60^{o}) - m(0^{o})}{m(120^{o}) - m(0^{o})}. \quad (12)$$

For the four-angle parameterisation the well depth of the spherically averaged potential $V_0(R)$ is not simply obtained from the potential parameters; for comparison with the well depth from the differential

cross section data, the well depth of the spherically averaged potential is taken to be the same as the spherical average of the well depth

$$18\varepsilon_{iso} = \varepsilon(0^{o}) + 8\varepsilon(60^{o}) + 8\varepsilon(120^{o}) + \varepsilon(180^{o}). \qquad (13)$$

This introduces an error of less than 1 cm^{-1} into the isotropic well depth.

3.3.3 Angle-dependent parameterisation

The fitted parameters obtained for the four-angle potential form are less correlated than for the multipole parameterisation, but the four-angle parameterisation does have the disadvantage that spurious angular oscillations sometimes develop in the potential beyond the region sampled by the spectroscopic data. This is because the true potential changes very quickly near $\theta = 0^{o}$ and the four-angle potential attempts to model this behaviour using only Legendre terms up to $P_3(\cos\theta)$. One way around this problem is to specify each of the parameters ε, R_m and m as an explicit function of θ, so that the potential is necessarily smooth. Physically, R_m and m are expected to have one value near the linear Ar·H-Cl geometry ($\theta = 0^{o}$), where the principal repulsive interaction is between Ar and H, and a rather different value near the Ar·Cl-H geometry ($\theta = 180^{o}$), where the Ar·Cl interaction dominates. Between these limits there will be a fairly sudden change in R_m and m as the hydrogen end of HCl moves away out of contact with Ar. We therefore write

$$R_m(\theta) = R_m(0^o) + \Delta R\ f(\theta;\kappa) \tag{14}$$

$$m(\theta) = m(0^o) + \Delta m\ f(\theta;\kappa) \tag{15}$$

$$f(\theta;\kappa) = 1 - [\tfrac{1}{2}(1+\cos\theta)]^{\kappa}, \tag{16}$$

where $f(\theta;\kappa)$ is a function which is near 0 close to $\theta = 0^o$ and then has a fairly sharp change to a value near 1 beyond $\theta = 60^o$. The parameter κ describes the rate at which the changeover from H-like to Cl-like interactions takes place.

The MBER spectra of Ar·HCl and Ar·DCl are sensitive only to the potential near the minimum [34], but do provide a very sensitive probe of the angular curvature of the well near $\theta = 0^o$. It is thus desirable to parameterise the well depth so that this curvature is directly reflected in the potential parameters. This may be achieved by writing $\varepsilon(\theta)$ in the same form as $R_m(\theta)$ and $m(\theta)$

$$\varepsilon(\theta) = \varepsilon(0^o) + \Delta\varepsilon\ f(\theta;\lambda) \tag{17}$$

where the shape parameter λ is optimised independently of κ. This provides the necessary flexibility of $\varepsilon(\theta)$ in the region of the absolute minimum, but forces the well depth to be θ-independent near the Ar·Cl-H configuration. As will be seen below, none of the experimental data currently available sensitively probes the potential in the Ar·Cl-H region, so that this lack of flexibility does not damage the quality of fit; nevertheless, it should be remembered that this form of $\varepsilon(\theta)$ cannot model a second minimum near $\theta = 180^o$, so that the absence of such a minimum in our fitted potentials is not evidence against its existence. This restriction on the potential form will be relaxed in the next

chapter of this thesis.

The angle-dependent parameterisation provides an algorithm for evaluating $V(R,\theta)$ for a specified R and θ, but this form is not ideal for performing bound state or scattering calculations; in both cases the Legendre components $V_k(R)$ of the potential are required, in order to evaluate matrix elements of the potential between spherical harmonic basis functions. The required components may be expressed as integrals over the angular potential

$$V_k(R) = \int_{-1}^{1} (k + \tfrac{1}{2}) V(R,\theta)\ P_k(\cos\theta)\ d\cos\theta \qquad (18)$$

and these integrals are readily evaluated numerically using Gaussian quadrature. The resulting potential has important contributions from high order Legendre terms, but does not have a correspondingly large number of parameters. It has been found for Ar·HCl that approximately ten Legendre polynomials must be included to represent $V(R,\theta)$ accurately in the repulsive region, although convergence is much faster at larger R.

The well depth of the spherically averaged potential $V_0(R)$ is again not simply related to the potential parameters for this parameterisation. For comparison with the total differential cross section data [9], we have taken the spherical average of the well depth

$$\varepsilon_{iso} = \tfrac{1}{2} \int_{-1}^{1} \varepsilon(\theta)\ d\cos\theta = \varepsilon(0^{o}) + \Delta\varepsilon\ \lambda/(1+\lambda)\ . \qquad (19)$$

3.4 Potential optimisation

Least squares fits have been performed using the following four parameterisations.

Surface B1. Multipole parameterisation using Buckingham (α - 6) radial potentials.

Surface M1. Multipole parameterisation using Maitland-Smith radial potentials.

Surface M2. Four-angle parameterisation using Maitland-Smith radial potentials.

Surface M3. Angle-dependent parameterisation using Maitland-Smith radial potentials.

The parameters defining the best fit surfaces are given in table 2, and the surfaces are shown in figures 4-6. The fits to the experimental data are summarised in table 3 and figures 7-9.

3.4.1 Surface B1

This is a conventional multipole potential, using Buckingham (α - 6) radial functions and with the Legendre expansion truncated at the $P_3(\cos\theta)$ term. The anisotropic m and R_m values are constrained as discussed in section 3.3.1 above. The best fit potential is shown in figure 4 and the quality of fit is characterised by the sum of squares of weighted residuals $\chi^2 = 54.0$. This may be compared with $\chi^2 = 620$ for surface IIb of Holmgren et al. [29], which was obtained by fitting to the MBER spectra alone.

Surface B1 has three major disadvantages.

(1) The fitted parameters are highly correlated and have correspondingly high standard deviations; the correlation matrix for this

potential is given in table 4(a). The correlation coefficients between the anisotropic well depths ε_1 and ε_2, and between ε_2 and ε_3 are greater than -0.98, and there are several other correlation coefficients greater than 0.9.

(2) The angular centrifugal distortion constants D_θ and the high j rotational line broadening cross sections are not well reproduced by this potential. Both these effects occur because the truncated multipole parameterisation cannot model the shape of the HCl molecule in the repulsive region, where the hydrogen end of HCl is in contact with Ar and the repulsive component changes very rapidly with θ. The calculated D_θ values are too low because R_m does not decrease fast enough as θ increases from 0^o, and the high j line broadening cross sections are dominated by the repulsive part of the potential energy surface, where the multipole potential is not sifficiently anisotropic.

(3) The isotropic long range C_6 coefficient for the B1 surface is 6.56×10^{17} cm^{-1} pm^6, which is much higher than is expected from theoretical considerations; Waldman and Gordon [28] have given a value of $4.53 \times 10^{17} cm^{-1}$ pm^6 based on a Drude model.

All these effects are due to deficiencies in the parameterisation used and demonstrate that the conventional multipole parameterisation is not adequate for representing strongly anisotropic intermolecular potentials.

3.4.2 Surface M1

This differs from surface B1 only in that the radial functions used are Maitland-Smith instead of Buckingham (α-6) potentials. The quality

of fit is very similar, with $\chi^2 = 55.8$, and surfaces B1 and M1 are almost identical in the region of the minimum (see figure 4). However, the long range C_6 coefficient is significantly different ($4.20 \times 10^{17} cm^{-1} pm^6$) and agrees much better with the theoretical estimates. For this reason

Table 2. Parameters of optimised potentials.

Potential B1

ε_0	= 123.14(2.66)cm^{-1}	R_{m0}	= 386.72(0.84)pm	α_0	= 16.13(0.5
ε_1	= 21.70(5.08)cm^{-1}	R_{m_1}	= 407.36(2.86)pm	α_1	= 16.32(1.9
ε_2	= 27.07(7.39)cm^{-1}	R_{m2}	= 407.36pm	α_2	= 16.32
ε_3	= 9.12(4.75(cm^{-1}	R_{m3}	= 407.36pm	α_3	= 16.32
C_6	= $6.56 \times 10^{17} cm^{-1} pm^6$			χ^2	= 54.0

Potential M1

ε_0	= 123.99(2.59)cm^{-1}	R_{m0}	= 387.44(0.85)pm	m_0	= 13.61(0.5
ε_1	= 20.91(4.84)cm^{-1}	R_{m1}	= 406.22(2.81)pm	m_1	= 15.16(1.9
ε_2	= 27.67(7.18)cm^{-1}	R_{m2}	= 406.22pm	m_2	= 15.16
ε_3	= 8.48(4.73)cm^{-1}	R_{m3}	= 406.22pm	m_3	= 15.16
C_6	= $4.20 \times 10^{17} cm^{-1} pm^6$			χ^2	= 55.8

Potential M2

$\varepsilon(0^o)$	= 178.77(1.70)cm^{-1}	$R_m(0^o)$	= 397.01(0.47)pm	$m(0^o)$	= 15.87(0.4
$\varepsilon(60^o)$	= 127.42(2.15)cm^{-1}	$R_m(60^o)$	= 386.83pm	$m(60^o)$	= 13.55
$\varepsilon(120^o)$	= 113.82(2.02)cm^{-1}	$R_m(120^o)$	= 384.13(0.56)pm	$m(120^o)$	= 12.93
$\varepsilon(180^o)$	= 113.82cm^{-1}	$R_m(180^o)$	= 384.13pm	$m(180^o)$	= 12.93
C_6	$4.11 \times 10^{17} cm^{-1} pm^6$	ε_{iso}	= 123.5cm^{-1}	χ^2	= 34.9

Potential M3

$\varepsilon(0^o)$	= 180.82(1.52)cm^{-1}	$R_m(0^o)$	= 399.97(0.81)pm	$m(0^o)$	= 16.71(0.7
$\Delta\varepsilon$	= -67.67(0.93)cm^{-1}	ΔR	= 16.69(1.00)pm	Δm	= 3.92(1.1
λ	= 5.07(0.18)	κ	= 6.44(0.79)		
C_6	= $4.12 \times 10^{17} cm^{-1} pm^6$	ε_{iso}	= 124.3cm^{-1}	χ^2	= 31.1

Maitland-Smith potentials have been used in preference to Buckingham potentials as radial functions for the four-angle and angle-dependent potentials described below.

Table 3. Fits to data from molecular beam spectroscopy

	Experimental result	Uncertainty	Surface B1	Surface M1	Surface M2	Surface M3
			Ar·HCl spectra			
B/MHz	1678.511	2.0	1679.26	1679.34	1678.94	1678.92
D_J/kHz	20.0	0.5	19.85	19.94	19.95	19.80
$\langle P_2(\cos\theta)\rangle$	0.3406	0.002	0.3383	0.3384	0.3406	0.3404
$\langle P_1(\cos\theta)\rangle$	0.676	0.05	0.641	0.640	0.653	0.656
D_θ/ppm	23.7	2.0	20.50	19.55	24.70	24.32
			Ar·DCl spectra			
D_J/kHz	17.1	0.5	16.38	16.36	16.34	16.54
$\langle P_2(\cos\theta)\rangle$	0.5370	0.002	0.5391	0.5388	0.5368	0.5372
$\langle P_1(\cos\theta)\rangle$	0.834	0.05	0.802	0.802	0.803	0.804
D_θ/ppm	19.0	3.0	14.71	14.11	18.99	21.82

3.4.3 Surface M2

This is a four-angle potential with Maitland-Smith radial functions and fits the experimental data significantly better than the M1 or B1 potentials, with $\chi^2 = 34.9$. The final potential is shown in two representations in figures 4 and 5. The potential parameters are much

less strongly correlated and are consequently better determined. The spectroscopic data are much better reproduced than by the multipole potentials, particularly in the case of the angular centrifugal distortion constants D_θ. The high j line broadening cross sections are also modelled rather better, although the calculated cross sections are still consistently lower than the experimental values.

3.4.4 Surface M3

The angle-dependent parameterisation is the most physically reasonable of the parameterisations used here, since it introduces high Legendre polynomials in a realistic way to model the repulsive part of the potential. The optimised potential is shown in figures 4, 5 and 6. The parameters of the fitted potential are reasonably well decorrelated, as may be seen from the correlation matrix in table 4(b), and the parameters are well determined. The quality of fit is only slightly better than for the four-angle potential, with $\chi^2 = 31.1$, but surface M3 is nevertheless probably the most realistic. The long-range C_6 coefficient for surface M3 is 4.12×10^{17} cm^{-1} pm^6, which is in reasonably good agreement with the theoretical value [28].

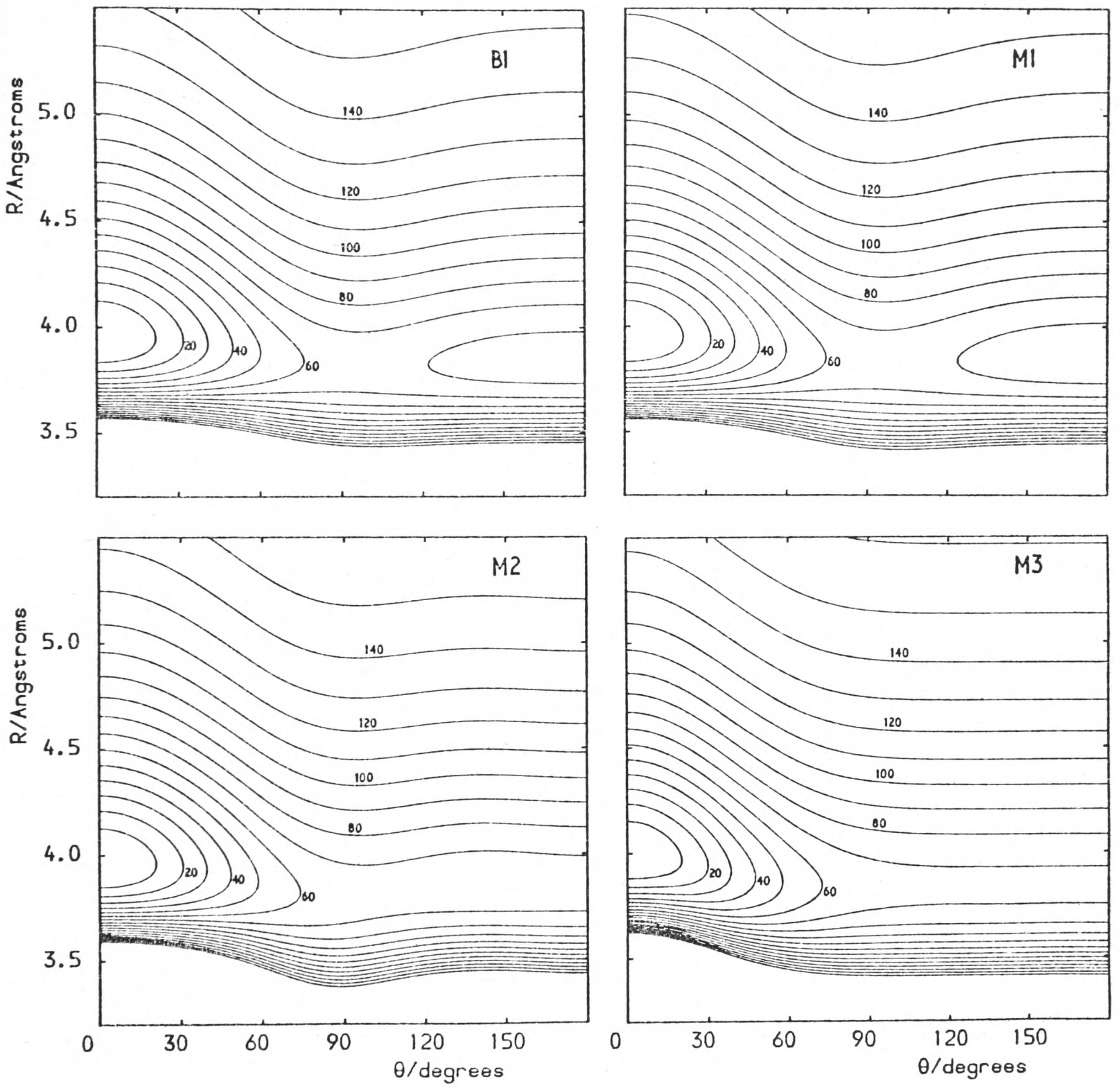

Figure 4. Contour plots of the four optimised potentials B1, M1, M2 and M3 for Ar HCl. Contours are plotted at 10 cm^{-1} intervals relative to the absolute minimum of each potential.

Figure 5. Coefficients of Legendre polynomials $V_k(R)$ for potentials M2 and M3 for Ar·HCl.

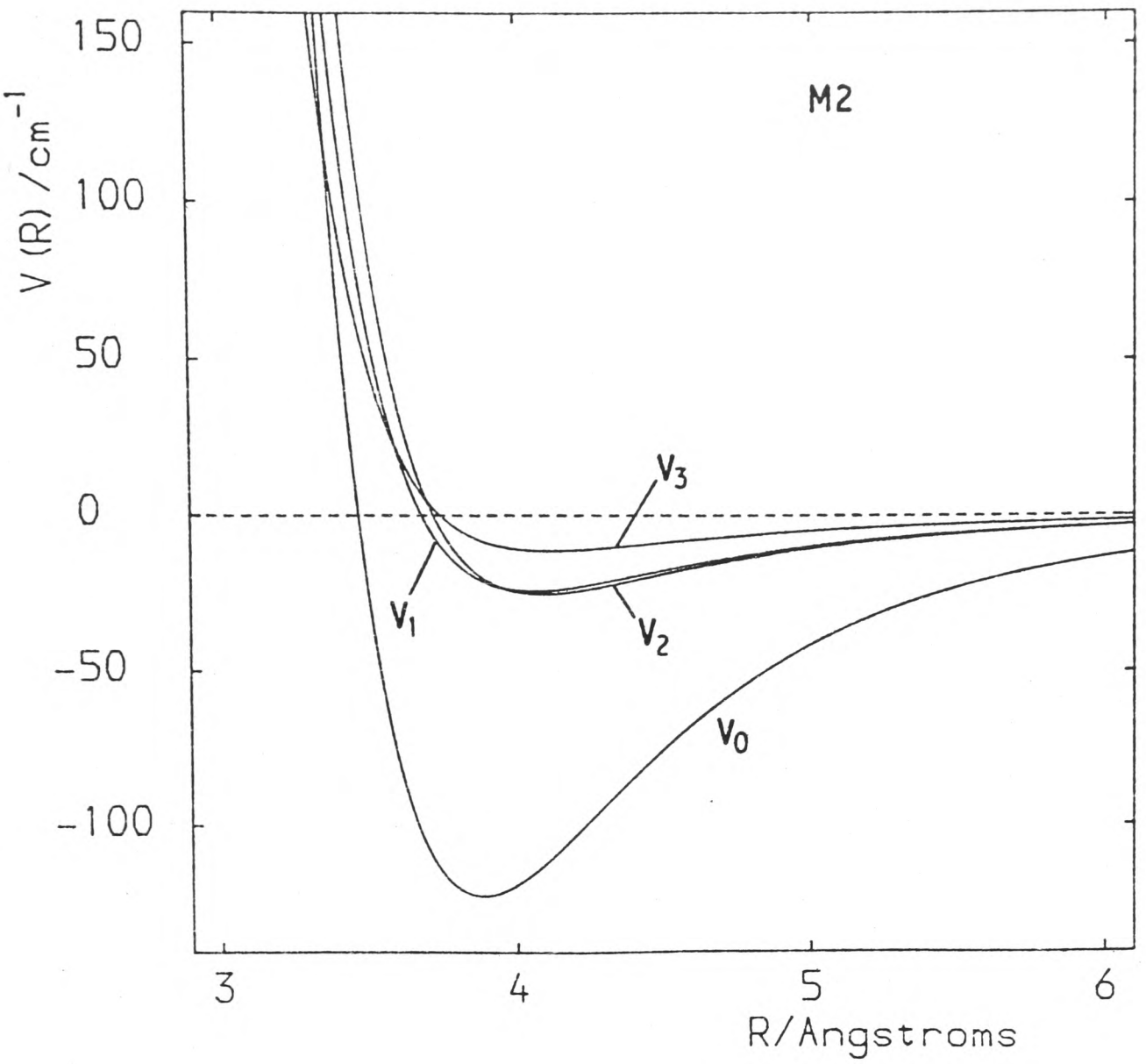
M2
V (R) /cm^{-1}
150
100
50
0
-50
-100
3
4
5
6
R/Angstroms
V_0
V_1
V_2
V_3

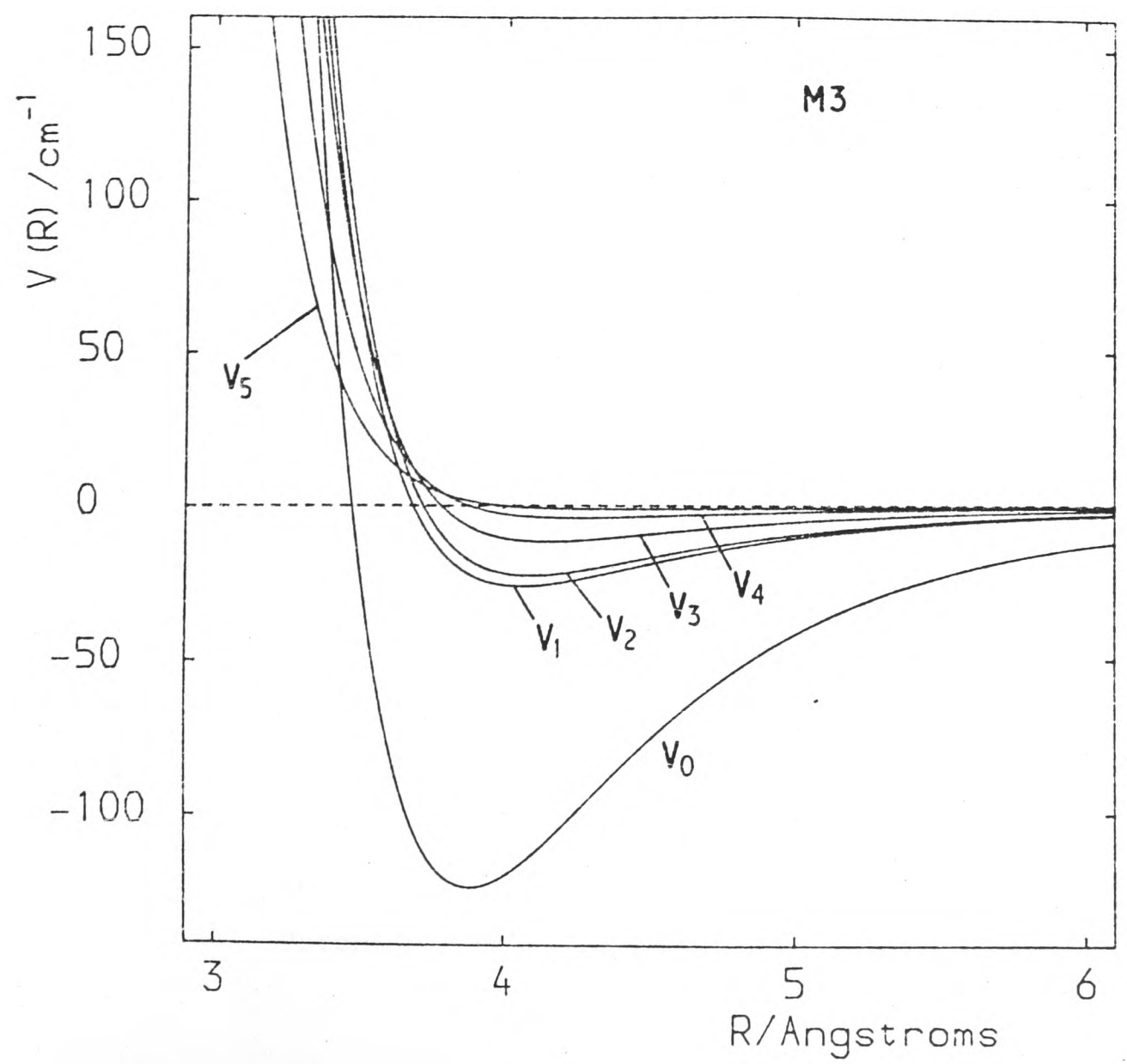
M3
V (R) /cm^{-1}
150
100
50
0
-50
-100
3
4
5
6
R/Angstroms
V_0
V_1
V_2
V_3
V_4
V_5

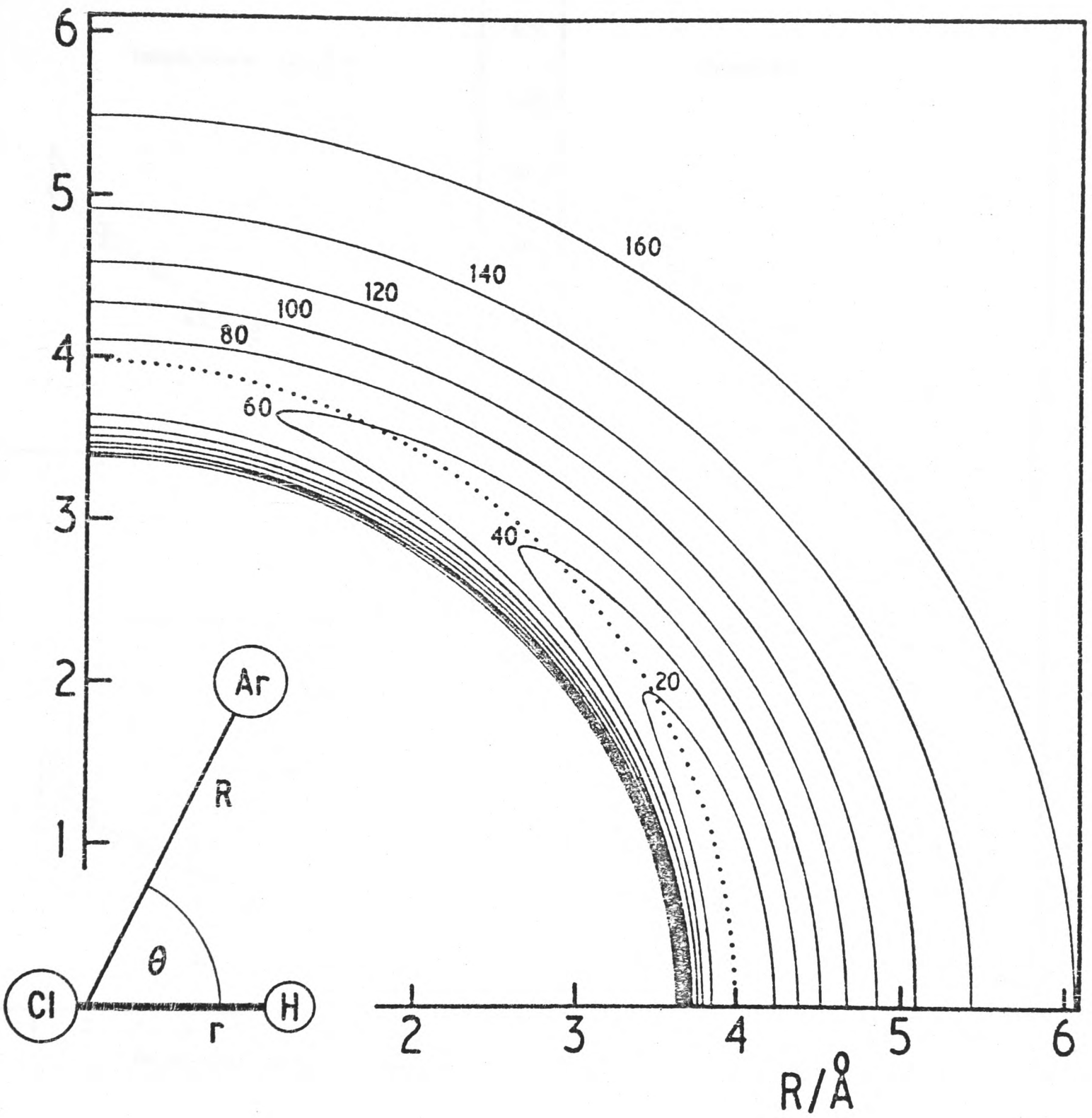

Figure 6. Polar contour plot of potential M3 for Ar·HCl.
Contours are plotted at 20 cm^{-1} intervals relative to the absolute minimum at -180.8 cm^{-1}. The dotted line is a circle at R = 4.0 A.
Potential M2 appears almost identical in this representation.

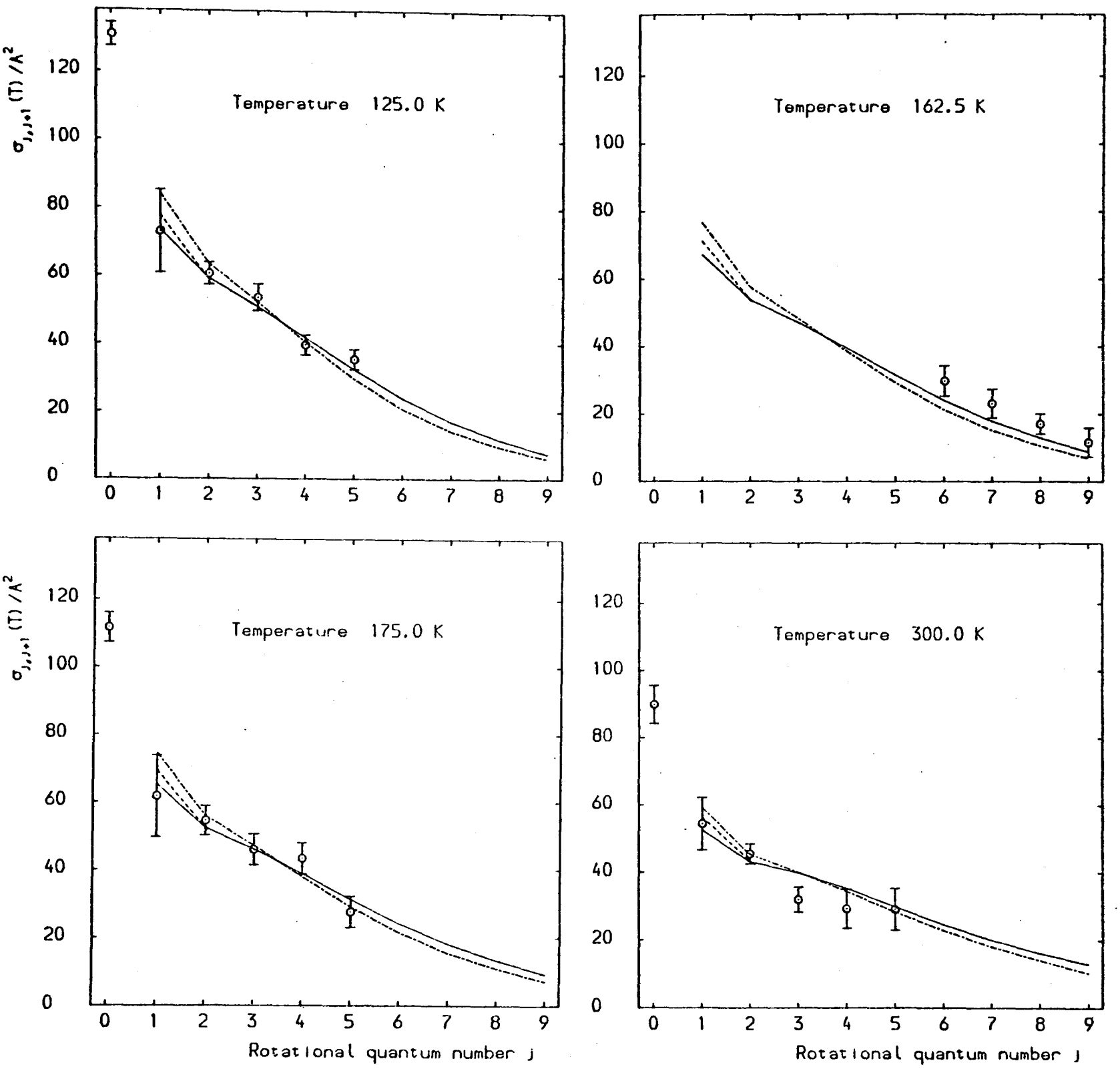

Figure 7. Comparison between experimental and calculated far infrared line broadening cross sections for HCl perturbed by Ar. The points with error bars are the experimental results, and the drawn lines are calculated for the optimised potentials.

----- M1 potential

----- M2 potential

—— M3 potential

The calculated cross sections for the M2 potential for j>3 are almost coincident with those for the M3 potential, and have not been shown separately.

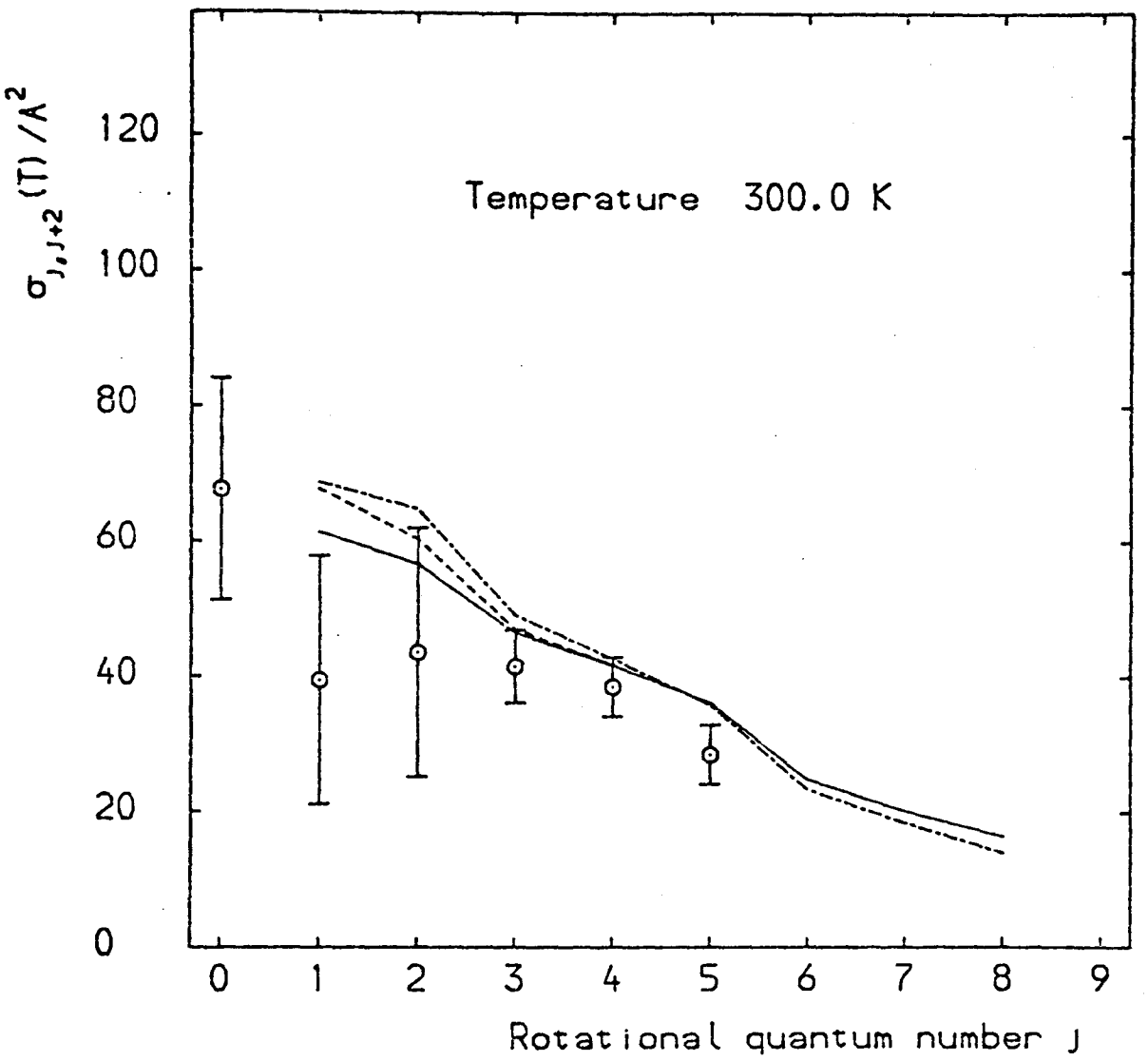

Figure 8. Comparison between experimental and calculated pure rotational Raman line broadening cross sections for HCl perturbed by Ar. The points with error bars are the experimental results, and the optimised potentials are represented as in figure 7.

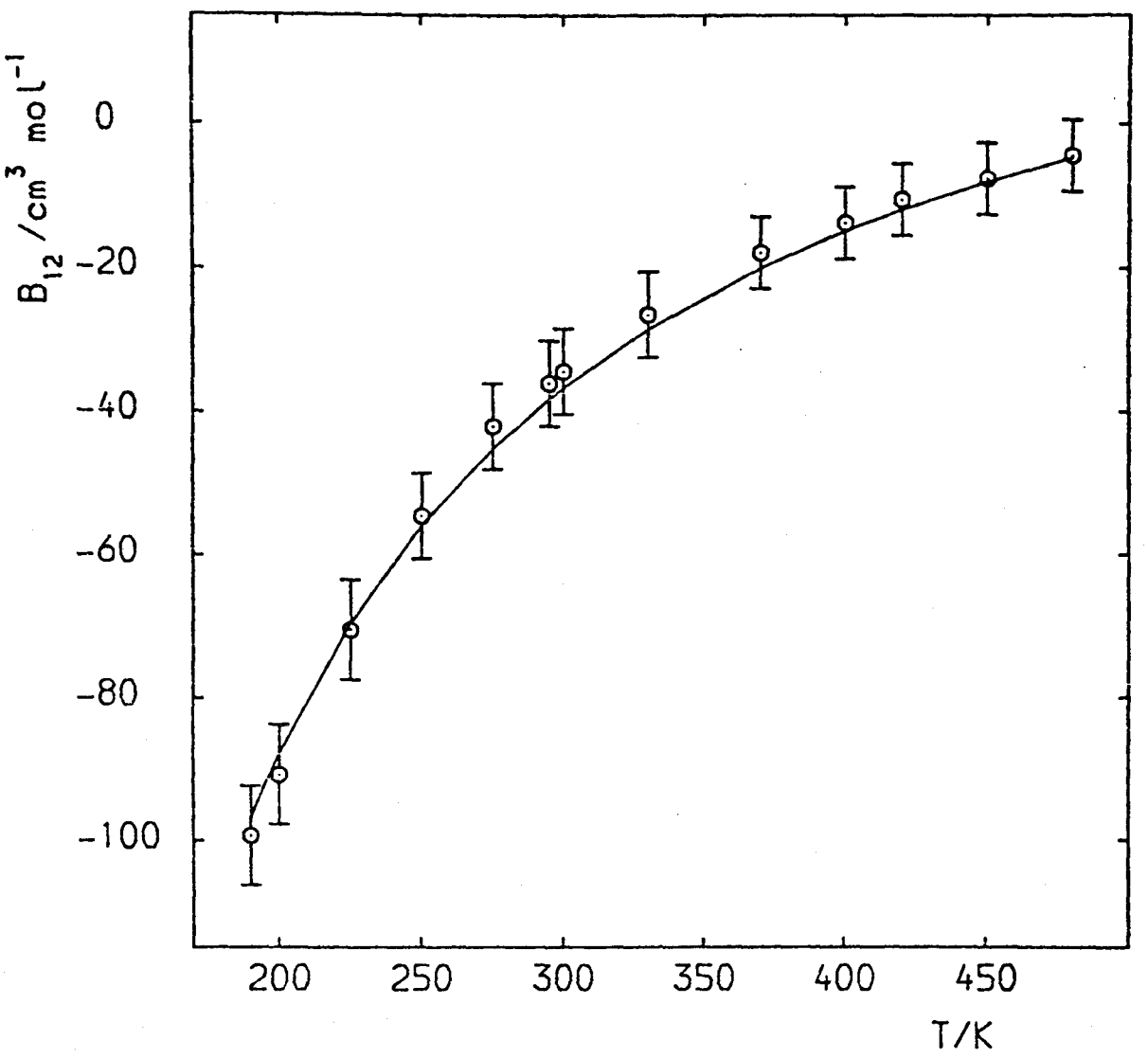

Figure 9. Comparison between experimental and calculated second virial coefficients for Ar+HCl mixtures. The points with error bars are the experimental results, and the solid line is calculated using potential M3. The calculated second virial coefficients for the B1, M1 and M2 potentials are within 1 cm^3 mol^{-1} throughout the temperature range.

Table 4

(a) Correlation matrix for surface B1

	ε_0	ε_1	ε_2	ε_3	m_0	m_1	R_{m0}	R_{m1}
ε_0	1.00							
ε_1	0.52	1.00						
ε_2	-0.46	-0.99	1.00					
ε_3	0.48	0.96	-0.99	1.00				
m_0	0.62	0.43	-0.36	0.39	1.00			
m_1	-0.66	-0.92	0.87	-0.85	-0.57	1.00		
R_{m0}	-0.60	-0.86	0.81	-0.82	-0.61	0.88	1.00	
R_{m1}	0.75	0.80	-0.74	0.75	0.73	-0.95	-0.85	1.00

(b) Correlation matrix for surface M3

	$\varepsilon(0^o)$	$\Delta\varepsilon$	λ	$m(0^o)$	Δm	$R_m(0^o)$	ΔR	κ
$\varepsilon(0^o)$	1.00							
$\Delta\varepsilon$	0.22	1.00						
λ	0.08	0.17	1.00					
$m(0^o)$	-0.17	-0.84	0.14	1.00				
Δm	0.28	0.90	-0.13	-0.91	1.00			
$R_m(0^o)$	0.32	-0.13	-0.27	0.15	0.03	1.00		
ΔR	-0.34	-0.06	0.25	0.01	-0.19	-0.88	1.00	
κ	0.14	-0.58	-0.19	0.58	-0.43	0.76	-0.49	1.00

3.5 Sensitivity of potential parameters to observables

The molecular beam spectra demonstrate unambiguously that the absolute minimum in the potential is at (or very near) a linear configuration and is very probably Ar·H-Cl rather than Ar·Cl-H. The

difference in expectation values of $P_2(\cos\theta)$ between Ar·HCl and Ar·DCl indicates that wide amplitude bending motion is taking place and the amplitude is expected to be larger for Ar·HCl than for Ar·DCl because of the difference in rotational constants between HCl and DCl. The magnitude of the isotope effect in $\langle P_2(\cos\theta)\rangle$ confirms that the equilibrium angle is close to 0^o (or 180^o). The angular expectation values themselves do not discriminate between the Ar·H-Cl and Ar·Cl-H equilibrium geometries, but this information may be obtained from the angular centrifugal distortion constants D_θ (see section 3.5.5 below).

Considerable physical insight may be gained from the Jacobian matrix for surface MB: that is, the matrix of partial derivatives of experimental observables with respect to potential parameters. This matrix is given (for selected observables) in table 5 and may be used to establish which experimental observables influence which parameters of the optimised potential.

3.5.1 Absolute well depth $\varepsilon(0^o)$

The absolute well depth is mainly determined by the second virial coefficients, particularly those for low temperatures. Second virial coefficients are principally a measure of the volume of the well, but the position of the absolute minimum R_e and the radial and angular curvatures of the well near the minimum are accurately determined by the MBER data, so that the influence of the second virial coefficients in our fits is primarily on the well depth.

The molecular beam total differential cross sections were also introduced as a constraint on the well depth, as discussed in section 3.1.4 above, and together with these other data produce an absolute well

Table 5. Jacobian matrix for surface M3 for selected observables

	$\varepsilon(0^{\circ})/cm^{-1}$	$\Delta\varepsilon/cm^{-1}$	λ	$m(0^{\circ})$	Δm	$R_m(0^{\circ})/pm$	$\Delta R/pm$	κ
				Ar·HCl spectra				
B/MHz	0.20	0.76	-0.94	-1.49	-0.43	-8.4	-3.8	5.2
D_J/kHz	-0.132	0.067	0.70	-1.07	-0.70	-0.23	-0.33	0.26
$\langle P_2(\cos\theta)\rangle/10^{-3}$	0.026	-5.1	0.89	-0.26	3.1	0.115	-0.20	1.06
D_θ/ppm	0.031	0.49	1.38	-0.31	-0.47	-0.184	-1.5	0.43
				Ar·DCl spectra				
D_J/kHz	-0.109	0.036	0.151	-0.92	-0.44	-0.195	-0.192	0.32
$\langle P_2(\cos\theta)\rangle/10^{-3}$	0.003	-4.0	13.8	-0.44	2.7	0.127	-0.29	0.68
D_θ/ppm	0.026	-0.51	-0.79	-0.149	-0.223	-0.20	-0.96	1.30
				Second virial coefficients				
$B_{12}(T = 190K)$/ $cm^3 mol^{-1}$	-1.50	-1.21	3.0	4.7	4.2	-0.80	-0.72	-0.057
$B_{12}(T = 480K)$/ $cm^3 mol^{-1}$	-0.40	0.33	0.78	2.4	2.2	-0.063	-0.078	-0.128
				Far infrared line broadening cross sections				
$j = 1 \rightarrow 2$ (125 K)/$Å^2$	-0.042	-0.51	-0.89	-0.73	0.26	0.070	-0.95	-2.2
$j = 1 \rightarrow 2$ (300K)/Å	0.038	-0.35	-0.96	-0.81	0.21	0.26	-0.67	-1.80
$j = 9 \rightarrow 10$ (162.5K)/$Å^2$	0.037	-0.047	-0.25	1.07	-0.174	-0.049	-0.29	-0.49

depth of 180.8 cm^{-1} for the M3 potential, corresponding to an isotropic well depth around 124 cm^{-1}. If the differential cross sections are omitted from the fit, the resulting well depth is 178.0 cm^{-1}, with small changes in the other parameters. A detailed analysis of the differential cross sections is required to establish whether the fitted potentials are capable of reproducing the experimental results.

It may be noted here that the standard deviations quoted for the fitted potentials parameters in table 2 are a measure of the sensitivity of the parameters to random errors in the data; if systematic errors are present, the potential parameters may vary by much larger amounts. Nevertheless, the well depth obtained here is almost certainly accurate to ± 10 cm^{-1}. The very large well depths for Ar·HCl that have been obtained from the temperature dependence of intensities of infrared spectra [11-13] are incorrect; these data have recently been reanalysed by Boom [35] to give a well depth of 233 ± 25 cm^{-1} for Ar·HCl, which is in much better agreement with the value obtained here.

3.5.2 Well depth anisotropy, $\Delta\varepsilon$ and λ

These are principally determined by the spectroscopic expectation values of $P_2(\cos\theta)$, which are obtained from Cl nuclear quadrupole coupling constants in Ar·HCl and Ar·DCl. The $\langle P_2(\cos\theta)\rangle$ values for both isotopic species are strongly affected by $\Delta\varepsilon$, since an increased (more negative) $\Delta\varepsilon$ results in stronger confinement of the HCl molecule near the linear Ar·H-Cl configuration. The angular well width parameter λ affects the two isotopes by very different amounts; an increase in λ increases the value of $\langle P_2(\cos\theta)\rangle$ for deuterium much more than that for the hydrogen species. The well depth anisotropy is

thus determined by the average of the Ar·HCl and Ar·DCl $\langle P_2(\cos\theta)\rangle$ values whereas the width parameter λ is determined by the isotope effect in $\langle P_2(\cos\theta)\rangle$.

It is also interesting to note the effect of $\Delta\varepsilon$ on the line broadening cross sections; the low j cross sections are somewhat sensitive to $\Delta\varepsilon$, increasing with increasing anisotropy, but the high j cross sections are almost completely insensitive. This is because the anisotropy in the well region is a slowly varying function of R, so that the well region cannot provide a sufficiently fast-varying anisotropy to cause inelastic transitions in high j states of HCl; in order to broaden the high j rotational lines, a short-lived impulsive perturbation is required and this can be provided only by the anisotropy of the repulsive wall. Even the low j linewidths are not strongly affected by the well depth anisotropy, which explains why Ar·HCl potentials derived principally from line broadening data [6, 22] have failed to reproduce the MBER spectra.

3.5.3 Radial curvature parameters $m(0^o)$ and Δm

These are principally determined by the spectroscopic centrifugal distortion constants D_J, since an increase in m results in a larger stretching force constant for the van der Waals bond and a reduced centrifugal distortion constant. The second virial coefficients are also affected by m, as mentioned above, but the influence of the centrifugal distortion constants is dominant. The D_J values for the hydrogen and deuterium complexes are affected similarly by $m(0^o)$, but Δm influences the hydrogen D_J value more than the deuterium constant; this is because the amplitude of bending motion is larger for Ar·HCl

than for Ar·DCl, so that the Ar·HCl D_J constant samples the radial curvature of the well over a larger angular range.

The effect of the radial curvature parameters on the line broadening cross sections is also of interest. The effect of increasing $m(0^o)$ here is to steepen both the isotropic and the anisotropic repulsive walls; the peak anisotropy for a given collision is not greatly changed, but the time spent on the repulsive wall is decreased. This increases the high frequency Fourier components of the anisotropy at the expense of the low frequency components and thus increases the probability of inelastic collisions for HCl molecules in high j states, while decreasing the probability of inelasticity for molecules in low j states. The overall effect of an increase in $m(0^o)$ is thus to decrease the low j line broadening cross sections and increase the high j cross sections.

3.5.4 Equilibrium distance $R_m(0^o)$

As discussed above, the equilibrium configuration of the complex is linear, Ar·H-Cl. The rotational constant of the Ar·HCl complex is a measure of the vibrationally averaged moment of inertia in the ground vibrational state and so provides a very accurate measure of the equilibrium distance at $\theta = 0^o$.

3.5.5 Well position anisotropy ΔR and shape parameter κ

ΔR and κ are principally determined by the angular centrifugal distortion constants D_θ and by the line broadening data. The quantity D_θ measures the change in angular curvature of the well with R and this

is closely related to the behaviour of $R_m(\theta)$ in the classically allowed region $\theta < 80^o$. As is clearly shown by our fits, a large positive value of D_θ requires that R_m decrease sharply as θ increases from 0^o and this is physically reasonable only for the Ar·H-Cl configuration, where the hydrogen end of HCl is in contact with the Ar atom. If the equilibrium configuration were Ar·Cl-H, $R_m(\theta)$ near equilibrium would be relatively insensitive to changes in θ, producing much smaller values of D_θ.

Changes in R_m with θ also strongly affect the anisotropy of the repulsive wall, so that the rotational linewidths increase as ΔR becomes greater (more negative). The observation that the linewidths decrease as κ increases is surprising, since this would, at first sight, be expected to increase the probability of inelastic collisions. The effect probably occurs because increasing κ increases the magnitude of high order Legendre terms in the potential anisotropy at the expense of low order terms and it is the low order anisotropies, $P_1(\cos\theta)$ and $P_2(\cos\theta)$, that are most effective in causing line broadening.

3.6 Conclusion

The potential surfaces for Ar·HCl obtained in this chapter give good fits to the molecular beam spectra, rotational linewidths, second virial coefficients and molecular beam total differential cross sections. The general features of the potential are unambiguously determined: the equilibrium configuration is linear, Ar·H-Cl, at an Ar-HCl centre of mass distance of 400 pm, and the radial position of the minimum $R_m(\theta)$ decreases sharply as the complex is bent away from its equilibrium

configuration.

The data from different experiments are to a large extent complementary; the MBER spectra determine the shape of the well near the absolute minimum, the rotational line broadening data are principally sensitive to the anisotropy of the repulsive wall and the second virial coefficients and differential cross sections provide information mainly on the depth of the potential well. The only feature of the intermolecular potential which is poorly determined is the depth of the well near the linear Ar·Cl-H configuration, which is not probed by the Ar·HCl complex in its ground vibrational state. This restriction will be investigated in the next chapter.

REFERENCES

1. S.E. Novick, P. Davies, S.J. Harris and W. Klemperer, J. chem. Phys. 59, 2273 (1973).

2. S.E. Novick, K.C. Janda, S.L. Holmgren, M. Waldman and W. Klemperer, J. chem. Phys. 65, 1114 (1976).

3. J.M. Hutson and B.J. Howard, J. chem. Phys. 74, 6520 (1981).

4. R.M. van Aalst, J. Schuurman and J. van der Elsken, Chem. Phys. Lett. 35, 558 (1975).

5. D. Frenkel, D.J. Gravesteyn and J. van der Elsken, Chem. Phys. Lett. 40, 9 (1976); D. Frenkel, Ph.D. thesis, Amsterdam (1977).

6. J.G. Kircz, G.J.Q. van der Peijl, J. van der Elsken and D. Frenkel, J. chem. Phys. 69, 4606 (1978).

7. G.J.Q. van der Peijl, D. Frenkel and J. van der Elsken, Chem. Phys. Lett. 56, 6)2 (1978).

8. B. Schramm and U. Leuchs, Ber. Bunsenges. phys. Chem. 83, 847 (1979).

9. J.M. Farrar and Y.T. Lee, Chem. Phys. Lett. 26, 428 (1974).

10. U. Buck and P. McGuire, Chem. Phys. 16, 101 (1976).

11. D.H. Rank, P. Sitaram, W.A. Glickman and T.A. Wiggins, J. chem. Phys. 39, 2673 (1963).

12. A.W. Miziolek and G.C. Pimentel, J. chem. Phys. 65, 4462 (1976).

13. E.W. Boom and J. van der Elsken, J. chem. Phys. 73, 15 (1980).

14. D. Frenkel and J. van der Elsken, Chem. Phys. Lett. 50, 116 (1977).

15. C. Boulet and D. Robert, Chem. Phys. Lett. 60, 162 (1978).

16. A.M. Leonardi-Cattolica, K.O. Prins and J.S. Waugh, J. chem. Phys. 54, 769 (1971).

17. D.H. Rank, D.P. Eastman, B.S. Rao and T.A. Wiggins, J. mol. Spectrosc. 10, 34 (1963); J. mol. Spectrosc. 13, 87 (1964); A. Levy, E.P. Mariel and C. Boulet, J. quant. Spectrosc. radiat. Transfer 13, 673 (1973); S.B. Petrov, Opt. Spectrosc. 39, 150 (1975); J. Wormhoudt, J.I. Steinfeld and I. Oppenheim, J. chem. Phys. 66, 3121 (1977); A.J. Miziolek, J. mol. Spectrosc. 65, 134 (1977).

18. A.M.B. Ding and J.C. Polanyi, Chem. Phys. 10, 39 (1975); B.A. Esche, R.E. Kutina, N.C. Lang, J.C. Polanyi and A.M. Rulis, Chem. Phys. 41, 183 (1979).

19. J.C. Polanyi, N. Sathyamurthy and J.L. Schreiber, Chem. Phys. 24, 105 (1977); J.C. Polanyi and N. Sathyamurthy, Chem. Phys. 29, 9 (1978).

20. E. Piollet-Mariel, C. Boulet and A. Levy, J. chem. Phys. 74, 900 (1981).

21. E. Piollet-Mariel, C. Boulet and A. Levy, J. chem. Phys. to be published.

22. W.B. Neilsen and R.G. Gordon, J. chem. Phys. 58, 4131 (1973); 58, 4149 (1973).

23. H.E. Scott, Ph.D. thesis, Ohio State University (1973).

24. A.M. Dunker and R.G. Gordon, J. chem. Phys. 64, 354 (1976).

25. J.A. Vliegenthart and A. Rozendaal, private communication quoted in reference 26.

26. I.F. Kidd, G.G. Balint-Kurti and M. Shapiro, Faraday Discus. R. Soc. Chem. 71/22 (1981).

27. P.H. Blustin, Theoret. Chem. Acta (Berl.) 47, 249 (1978); W. Kolos, G. Corongiu and E. Clementi, Int. J. quant. Chem. 17, 775 (1980).

28. M. Waldman and R.G. Gordon, J. chem. Phys. 71, 1340 (1979).

29. S.L. Holmgren, M. Waldman and W. Klemperer, J. chem. Phys. 69, 1661 (1978).

30. G.C. Maitland and E.B. Smith, Chem. Phys. Lett. 22, 443 (1973) i.

31. R.A. Aziz and W. Kocay, Molec. Phys. 30, 857 (1975).

32. C.A. Linse, J.J.H. van den Biesen, E.H. van Veen and C.J.N. van den Meijdenberg Physica A 99, 166 (1979); J.J.H. van den Biesen, F.A. Stokvis, E.H. van Veen and C.J.N. van den Meijdenberg, Physica A 100, 375 (1980).

33. A.D. Buckingham, Adv. chem. Phys. 12, 107 (1967).

34. J.M. Hutson, A.E. Barton, P.R.R. Langridge-Smith and B.J. Howard, Chem. Phys. Lett. 73, 218 (1980).

35. E.W. Boom, Ph.D. thesis Amsterdam (1981).

CHAPTER 4

RARE GAS - HYDROGEN CHLORIDE SYSTEMS

CHAPTER 4

RARE GAS - HYDROGEN CHLORIDE SYSTEMS

In the preceding chapter, anisotropic intermolecular potentials for Ar·HCl were obtained by simultaneous least squares fitting to rotational spectra of the bound Ar·HCl complex [1-3], pressure broadening of HCl rotational lines by Ar [4-6], second virial coefficients of Ar+HCl mixtures [7] and molecular beam total differential cross sections [8]. The different sets of data were to a large extent complementary, and the resulting potential was well determined over a large area of configuration space. The equilibrium geometry was found to be linear, Ar·H-Cl, at an Ar - HCl centre of mass distance of 400 pm, with a well depth around 180 cm^{-1}. The only remaining uncertainty was in the well depth near the linear Ar·Cl - H configuration; the best fit potential did not have a secondary minimum here, but such a minimum was not excluded by the experimental data.

The purpose of this chapter is to extend this work to the systems Ne·HCl, Kr·HCl and Xe·HCl. Rotational spectra of all these complexes have been observed in molecular beams [9-14], and far infrared line broadening data are also available [4,15]. It is found that several of the potential parameters are independent of the rare gas, while others follow clear trends down the series. In addition, the Ne·HCl spectra demonstrate that the Ne·HCl complex does have a shallow secondary minimum at the Ne·Cl-H configuration, so that similar behaviour may be expected for the other complexes. This information is used in deriving potentials for Kr·HCl and Xe·HCl, and a revised Ar·HCl potential incorporating this feature is also presented.

4.1 Isotope dependence of the intermolecular potential

Before considering intermolecular potentials for individual systems, a minor improvement used in this chapter for interpreting spectroscopic rotational constants of van der Waals complexes will be described.

For most of the spectroscopic parameters, the dependence of the intermolecular potential on the isotopic species involved may safely be neglected, but this is not the case for the rotational constants. The rotational constant of a van der Waals molecule is related to the expectation value $\langle 1/R^2 \rangle$, involving an average over the wide-amplitude vibrations of the complex. The zero-point vibrational amplitude of the DCl molecule is smaller than that of the HCl molecule, so that the DCl molecule is effectively smaller than HCl: the values of r_0 obtained from the rotational constants of HCl and DCl are 128.387 and 128.124 pm respectively. This will produce a smaller value of the equilibrium separation $R_m(0^o)$ in DCl complexes compared to the corresponding HCl complex, with a correspondingly larger rotational constant than would otherwise be expected.

In chapter 3, the rotational constant of Ar·DCl was omitted from the least squares fits because of this effect. However, it is possible to correct for this on a more quantitative basis, and include a (modified) rotational constant for DCl complexes in the least-squares fits. The decrease in effective size is expected to be largest at $\theta = 0^o$ (linear Rg·HCl), and very small at the T-shaped geometry. It is thus possible to calculate rotational constants for the Rg·DCl complexes both on the Rg·HCl surface and on a modified surface appropriate to the deuterium complex, according to the prescription

$$R_m^D(0^o) = R_m^H(0^o) - \delta \qquad (1)$$

$$R_m^D (90^o) = R_m^H (90^o) \qquad (2)$$

with all the other potential parameters unaltered. The quantity δ is 0.252 pm for HCl complexes. The experimental rotational constants for the Rg·DCl complexes may then be corrected by the differences between these two calculated values. The corrections appropriate to Ne·DCl, Ar·DCl, Kr·DCl and Xe·DCl are given in Table 1; the corrected values given in the table were used in the least squares fits described below.

Table 1. Corrections applied to rotational constants of DCl complexes (MHz)

	experiment	correction	corrected value
Ne·D^{35}Cl	2698.1373	1.70	2696.44
Ar·D^{35}Cl	1657.627	1.44	1656.19
^{84}Kr·D^{35}Cl	1183.7728	1.05	1182.72
^{129}Xe·D^{35}Cl	979.4096	0.93	978.48

4.2 Ne·HCl

The rotational spectra of the Ne·HCl [9] and Ne·DCl [10] van der Waals complexes have recently been measured, and information is also available on the broadening of HCl far infrared spectra by Ne [15]. The spectra of the Ne·HCl (DCl) complexes are qualitatively different from those of the other complexes considered here, because of the much lower anisotropy of the intermolecular potential for Ne·HCl. In Ne·HCl, the barrier to internal rotation of HCl is comparable with its rotational constant, so that the motion is better regarded as a hindered rotation, rather than as a wide amplitude vibration. The spectra are thus sensitive

to the entire range of the angular coordinate θ, enabling information to be obtained on the potential near the linear Ne·Cl-H configuration; similar information is not directly available for the more anisotropic complexes Ar·HCl, Kr·HCl and Xe·HCl.

4.2.1 Parameterisation of the potential

In chapter 3, it was concluded that the most satisfactory parameterisation of the intermolecular potential was to express the potential at each angle θ in the Maitland-Smith form [16], and to write the parameters of the Maitland-Smith potential as explicit functions of θ. This approach is retained in the present chapter, although the functional forms used for $\varepsilon(\theta)$ and $R_m(\theta)$ have been modified.

Since the spectra of Ne·HCl and Ne·DCl are sensitive to the whole angular range of the potential, a parameterisation of the well depth function $\varepsilon(\theta)$ in terms of the depth and width of a single angular well is not appropriate. Even if the parameterisation is modified to incorporate a secondary minimum at the Ne·Cl-H configuration, as for Ar·HCl below, the fitted parameters obtained for Ne·HCl are highly correlated. In order to obtain a more suitable parameterisation of $\varepsilon(\theta)$, it is necessary to investigate how the spectroscopic parameters are related to potential features in the weakly anisotropic case. The well depth function $\varepsilon(\theta)$ is principally determined by the angular expectation values; for very low anisotropies, perturbation theory may be used to obtain expressions for the expectation values of $P_1(\cos\theta)$ and $P_2(\cos\theta)$, starting from the isotropic limit. The leading terms in the expressions obtained are

$$\langle P_1(\cos\theta)\rangle = \frac{\langle j=0|P_1(\cos\theta)|j=1\rangle \langle j=1|V(\theta)|j=0\rangle}{b} \qquad (3)$$

$$\langle P_2(\cos\theta)\rangle = \frac{\langle j=0|P_2(\cos\theta)|j=2\rangle \langle j=2|V(\theta)|j=0\rangle}{3b} \qquad (4)$$

where b is the rotational constant of the diatomic molecule, and the effects of wide amplitude stretching motion have been neglected. If the potential $V(\theta)$ is expanded in terms of Legendre polynomials

$$V(\theta) = \sum_k V_k P_k(\cos\theta) \qquad (5)$$

the matrix elements of $V(\theta)$ appearing in equations (3) and (4) are directly proportional to V_1 and V_2 respectively. Although the anisotropy in Ne·HCl is too great for these expressions to hold accurately, a parameterisation of the potential in terms of the Legendre components of the well depth function nevertheless yields well determined parameters

$$\varepsilon(\theta) = \sum_k \varepsilon_k P_k(\cos\theta) \qquad (6)$$

and this form of $\varepsilon(\theta)$ has been used for Ne·HCl. The summation over k was truncated at the ε_2 term, since inclusion of ε_3 did not improve the quality of fit by a statistically significant amount.

Preliminary fits to the data for Ne·HCl indicated the presence of a subsidiary minimum around $\theta = 180^{\circ}$; before describing the parameterisations used for $m(\theta)$ and $R_m(\theta)$, the probable origin of this potential feature will be examined. It is at first sight surprising that a significant minimum should exist at Rg·Cl-H geometry, since the attractive forces are not expected to be very anisotropic in this region [17]. However, inspection of a charge density contour diagram for HCl (figure 1) shows that the electron density is concentrated away from the

molecular axis, so that a rare gas atom can approach closer to Cl in the linear Rg·Cl-H configuration than is possible in the T-shaped geometry. The attractive forces at this smaller distance are significantly greater than at $\theta = 90^{o}$, giving rise to a minimum at the linear geometry.

The functional form previously used for $R_m(\theta)$ has therefore been altered to incorporate this behaviour around $\theta = 180^{o}$,

$$R_m(\theta) = R_m(0^{o}) + \Delta R_1 \; f(\theta;\kappa) + \Delta R_2 \; g(\theta) \qquad (7)$$

where $g(\theta) = \cos^2\theta, \quad \theta > 90^{o}$

$g(\theta) = 0, \qquad \theta < 90^{o}$.

The function $g(\theta)$ has the required behaviour; it is 1 near $\theta = 180^{o}$, and goes smoothly to zero at $\theta = 90^{o}$. ΔR_2 is not experimentally accessible for any of the complexes considered here, but it may be estimated from the theoretical charge density distribution for HCl. We have estimated ΔR_2 for HCl from the contour plots of Cade et al. [18], and obtained a value of -16 pm relative to the HCl centre of mass. ΔR_2 has been fixed at this value for all the complexes of HCl considered here.

The functional form used for $m(\theta)$ here is the same as for Ar·HCl in chapter 3

$$m(\theta) = m(0^{o}) + \Delta m \; f(\theta;\xi) \qquad (8)$$

except that ξ was not constrained to be the same as κ (for $R_m(\theta)$).

The experimental data for Ne·HCl are not as extensive as those for Ar·HCl; in particular, there are no data sensitive to the absolute well depth. The centrifugal distortion constants D_J are principally sensitive to the radial curvature of the well near the van der Waals

minimum, which in turn depends on the well depth and the wall parameter $m(\theta)$. There is evidence from studies of rare gas pair potentials [19] that the wall parameter does not change greatly with the rare gas involved, and we have accordingly fixed $m(0^o)$ and Δm for Ne·HCl at values similar to those determined for Ar·HCl below. The parameters κ and ξ were also fixed at the Ar·HCl values, since they are principally determined by the shape of the HCl molecule.

4.2.2 Potential optimisation

A simultaneous least squares fit has been performed to the 12 parameters obtained from the MBER spectra of the Ne·HCl and Ne·DCl complexes [9,10] and the 7 far infrared line broadening cross sections for HCl perturbed by Ne [15]. Scott has given the experimental uncertainties in his line broadening cross sections as ±5 to 10%, which is smaller than the computational uncertainties. The estimated computational uncertainty of ±3 $\mathring{A}^2$ has accordingly been used for all the line broadening cross sections for the Ne·HCl system. The parameters of the fitted potential (which will be referred to as the M4 potential) are given in table 2, and a contour plot is shown in figure 2. The fit to the molecular beam spectra is summarised in table 3, and the fit to the rotational line broadening data is shown in figure 3. The sum of the squares of weighted residuals χ^2 is 13.1.

Table 2. Parameters of M4 potential for Ne·HCl

ε_0	= 47.62 (0.89) cm^{-1}	$R_m(0^o)$	= 379.01 (1.48) pm	$m(0^o)$	= 22.2
ε_1	= 5.67 (0.18) cm^{-1}	ΔR_1	=-11.92 (1.72) pm	Δm	= -9.6
ε_2	= 14.07 (0.31) cm^{-1}	κ	= 12.7	ξ	= 16.4
		ΔR_2	=-16.0	γ	= 9.0

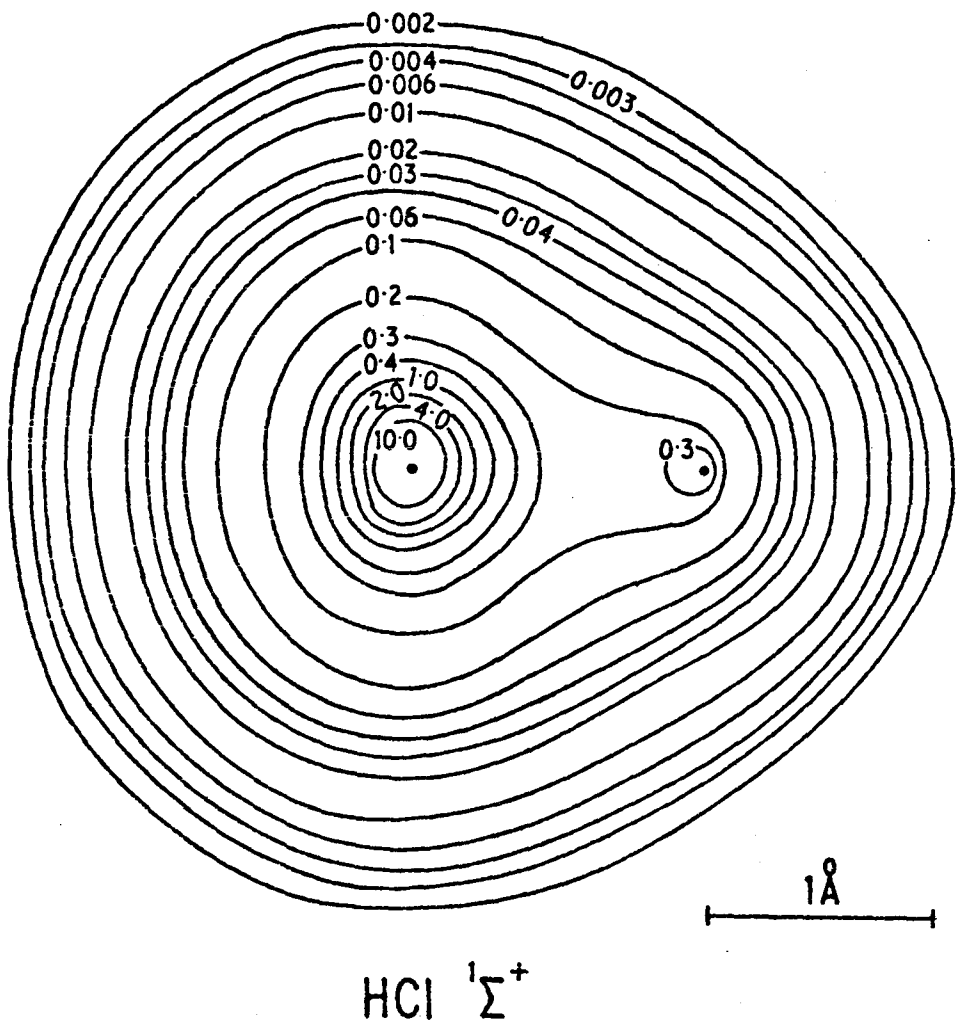

Figure 1. Contour plot of the total charge density in HCl.

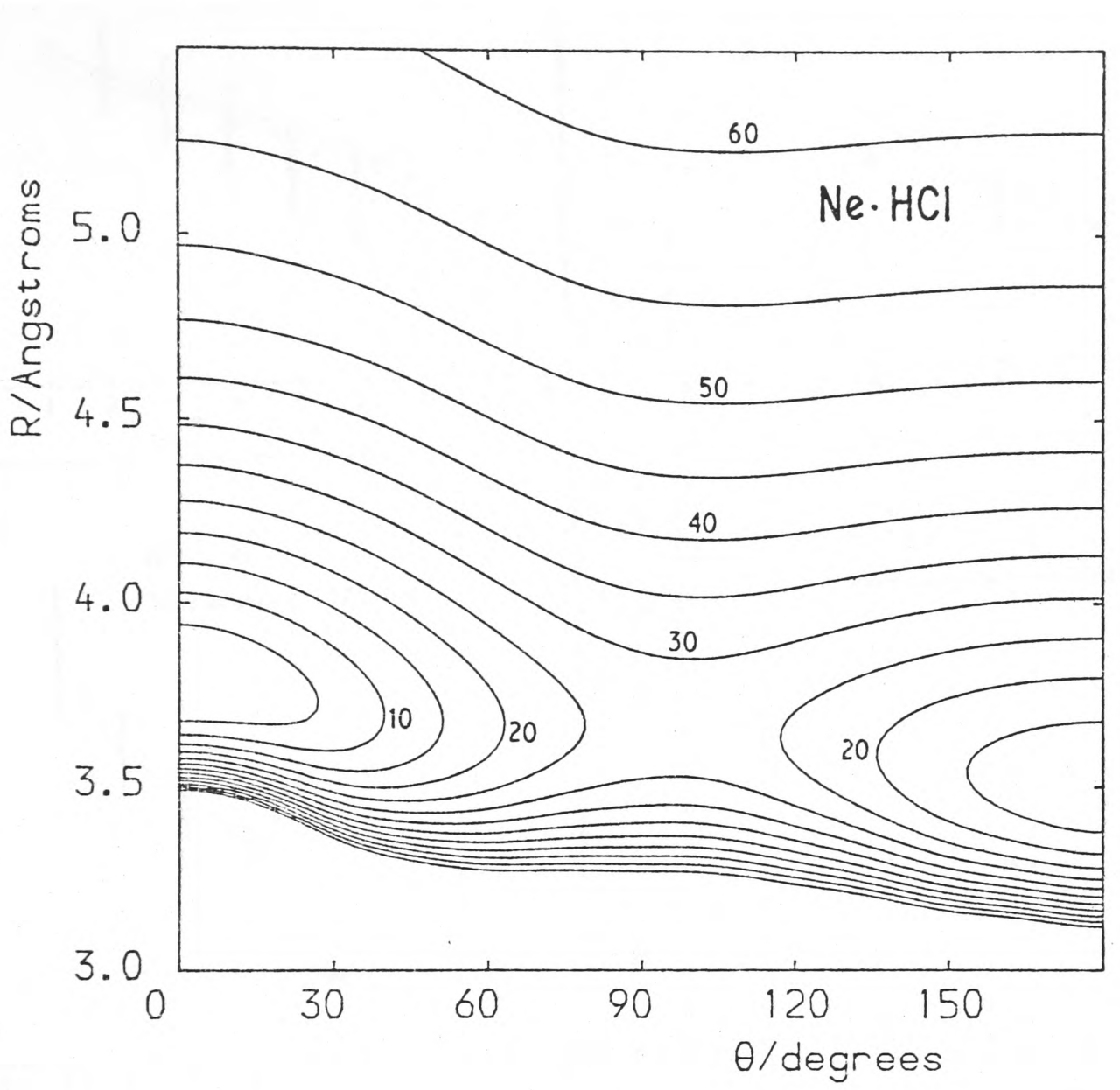

Figure 2. Contour plot of potential M4 for Ne·HCl. Contours are at 5 cm^{-1} intervals relative to the absolute minimum.

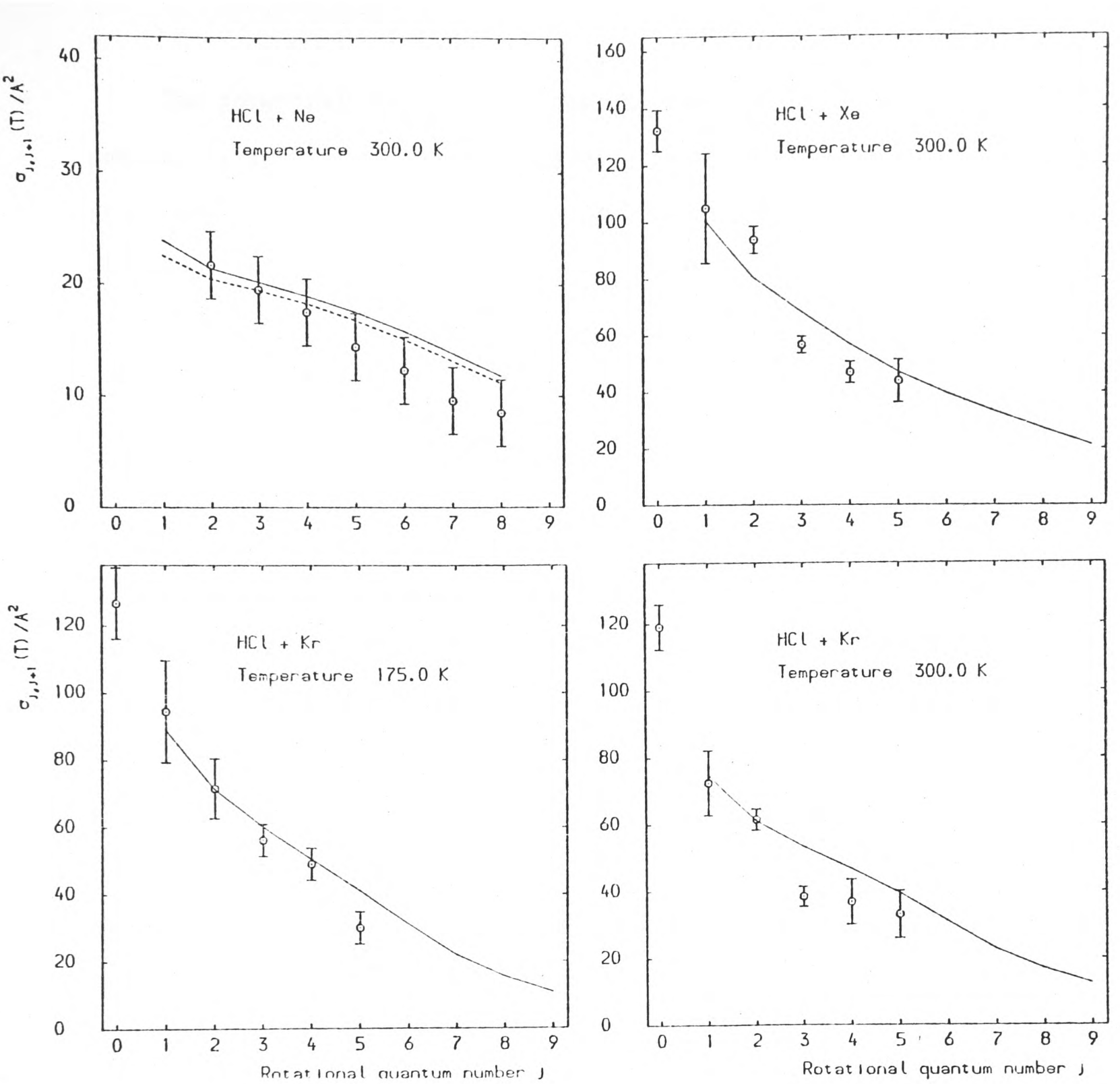

Figure 3. Comparison of experimental and calculated far infrared line broadening cross sections for HCl perturbed by rare gases. The points with error bars are the experimental results, and the drawn lines are calculated for the optimised potentials. For Ne·HCl, the solid line is for potential M4, and the broken line for potential M5.

The potential around $\theta = 0^{o}$ has the same general form as the potentials for Ar·HCl, Kr·HCl and Xe·HCl obtained below. The well depth at $\theta = 180^{o}$ is 56.0 cm^{-1}, compared with 40.6 cm^{-1} at $\theta = 90^{o}$. The model used for the origin of the secondary minimum may now be tested, since it predicts that the long range C_6 coefficients at $\theta = 90^{o}$ and 180^{o} will be approximately the same. For a Maitland-Smith potential, the C_6 coefficient is given by

$$C_6 = \varepsilon R_m^6 . \qquad (9)$$

The values obtained from this formula are 1.00×10^{17} cm^{-1} pm^6 and 1.06×10^{17} cm^{-1} pm^6 at $\theta = 90^{o}$ and 180^{o} respectively; considering the roughness of the model, these are remarkably similar. These values may also be compared with C_6 coefficients for the Ne·Ar interaction, which would be expected to be similar to the Ne·Cl interaction. The C_6 value obtained from a Maitland-Smith potential for Ne·Ar [19] is 1.09×10^{17} cm^{-1} pm^6, whereas the accurate value (from oscillator strength sum rules [20]) is 0.99×10^{17} cm^{-1} pm^6.

4.3 The subsidiary minimum at $\theta = 180^{o}$

The presence of a subsidiary minimum in the potential surface for Ne·HCl strongly suggests that such a feature will occur also for Ar·HCl, Kr·HCl and Xe·HCl. For Ar·HCl, there are also two additional pieces of information which suggest the presence of a secondary minimum

1) Buck and Schleusener [21] have carried out coupled states calculations of total differential cross sections for Ar·HCl on the M3 potential of chapter 3, and for the HWK potential, and their results

are shown in figure 4. The M3 potential accurately predicts the experimental position of the rainbow maximum and the magnitude of the high angle (inelastic) scattering, but the amplitude of the rainbow is better reproduced by the HWK potential. Pack [22] has shown that damping of rainbow oscillations is caused by the anisotropy of the well depth function, so that the presence of a secondary minimum may be expected to improve the fit to the molecular beam scattering data.

2) The ab initio potential of Vliegenthart and Rozendaal [23] has a substantial second minimum, which may also be attributed to closer approach of Ar to Cl at the linear geometry than is possible at $\theta = 90^{o}$. The VR potential is quite accurate near the linear Ar·H-Cl geometry; it is likely to be reasonably accurate near the linear Ar·Cl-H geometry also.

The experimental data for the systems Ar·HCl, Kr·HCl and Xe·HCl are relatively insensitive to the presence of such a secondary minimum, so that its characteristics must be fixed in the least squares fits. For these more strongly anisotropic systems, the parameterisation of $\varepsilon(\theta)$ in terms of the depth and width of the principal angular well has been retained, but an additional term has been introduced to produce a secondary minimum in such a way that its depth can be fixed independently of the other potential parameters

$$\varepsilon(\theta) = \varepsilon(0^{o}) + \Delta\varepsilon_1 \; f(\theta;\lambda) + \Delta\varepsilon_2 \; g(\theta) \qquad (10)$$

where $g(\theta)$ is again the function defined following equation (7). The quantity $\Delta\varepsilon_2$ has been estimated by assuming that the long range C_6 coefficient is the same at $\theta = 90^{o}$ and 180^{o}, so that

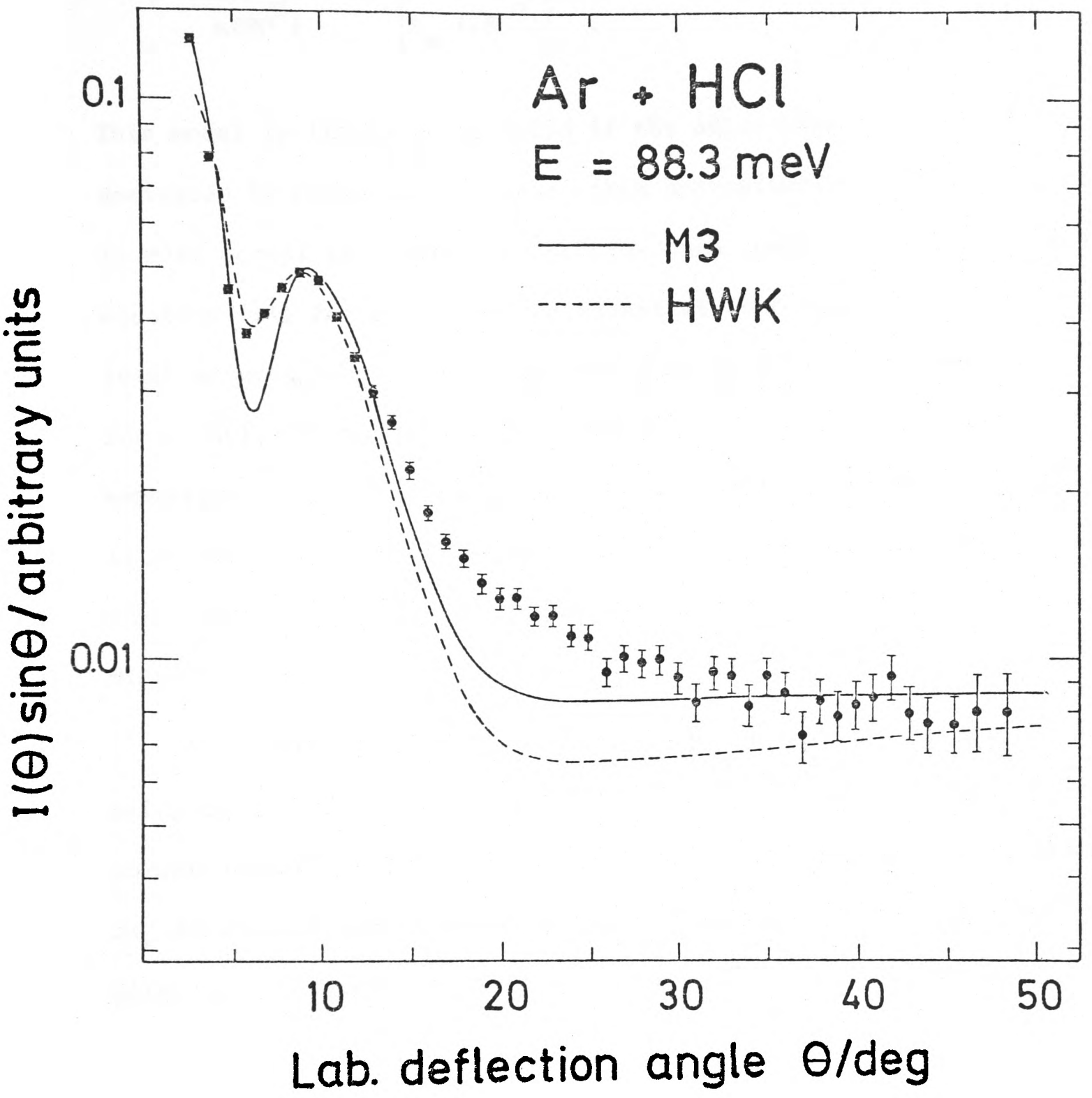

Figure 4. Comparison of experimental and calculated total differential cross sections for HCl scattered by Ar.
(Results of Buck and Schleusener)

$$\frac{\varepsilon(180^{o})}{\varepsilon(90^{o})} = \left[\frac{R_m\ (90^{o})}{R_m\ (180^{o})}\right]^6 . \qquad (11)$$

This model is likely to be valid if the attractive potential is dominated by dispersion forces; this approximation will be considered in more detail in chapter 6. $\Delta\varepsilon_2$ for each complex was determined from equation (11) for a preliminary potential, and then fixed in the final least squares fits. The values obtained by this method were 34 cm^{-1} for Ar·HCl, 39 cm^{-1} for Kr·HCl, and 43 cm^{-1} for Xe·HCl. It should be emphasised that these values are only estimates, and may very well be in error by up to 50%; however, fixing $\Delta\varepsilon_2$ at the value determined in this way is preferable to excluding the possibility of a secondary minimum altogether.

A second potential for Ne·HCl (M5 potential) has been obtained using this revised parameterisation, since this allows a more direct comparison with the Ar·HCl, Kr·HCl and Xe·HCl potentials obtained below. $\Delta\varepsilon_2$ for Ne·HCl was fixed at 14 cm^{-1}. The parameters of the resulting potential are given in table 4, and a contour plot is shown in figure 5. The quality of fit is characterised by $\chi^2 = 11.6$, which is comparable with that for the M4 potential above, and it may be seen from figures 2 and 5 that the two potentials are very similar. Nevertheless, the M4 potential is the recommended potential for Ne·HCl, since the form used for the well depth function $\varepsilon(\theta)$ was less restrictive in that case.

4.4 Ar·HCl

A least squares fit to the data for Ar·HCl has been performed using the modified parameterisation described above. The values of the

experimental observables input to the fit were exactly the same as those used in chapter 3, but the (modified) Ar·DCl rotational constant given in table 1 was also included. The parameters of the fitted potential are given in table 4, and a contour plot is shown in figure 5. The fit to the MBER spectra is summarised in table 3, and the fit to the line broadening cross sections is shown in figures 6 and 7. The fit to the second virial coefficients is very similar to that for the M3 potential (figure 9 of chapter 3). The sum of squares of weighted residual χ^2 was 31.4.

Apart from the secondary minimum at $\theta = 180^{o}$, this new Ar·HCl potential (M5 potential) is very similar to the M3 potential derived in chapter 3. The quality of fit is very similar, although the M5 potential does reproduce the high j infrared linewidths and the Raman linewidths more accurately than the M3 potential. These were the only respects in which the observed and calculated quantities for the M3 potential appeared to differ systematically.

The $\Delta\varepsilon_1$ parameter of the M5 potential is considerably larger (more negative) than $\Delta\varepsilon$ for the M3 potential, but this arises largely from the change in parameterisation rather than from a change in the shape of the potential for $0^{o} < \theta < 90^{o}$. The saddle point in the M5 potential occurs at $\theta = 100^{o}$, and is 76 cm^{-1} above the minimum; this may be compared with a barrier to internal rotation of HCl of 67.7 cm^{-1} for the M3 potential. The shape parameters κ and ξ are also significantly larger for the M5 potential, so that the functions $m(\theta)$ and $R_m(\theta)$ change more rapidly as θ increases from 0^{o}. This arises because the M5 potential has a significant repulsive anisotropy in the region $90^{o} < \theta < 180^{o}$ which was not present in the M3 potential, so that a smaller anisotropy around $\theta = 0^{o}$ is required to fit the far infrared linewidths.

Table 3. Fits to parameters from molecular beam spectroscopy

	B/MHz	D_J/kHz	$\langle P_1(\cos\theta)\rangle$	$\langle P_2(\cos\theta)\rangle$	D_θ/ppm
Ne·H^{35}Cl					
Experimental	2731.44	-	0.200	0.0812	-
M4 potential	2735.6	206.0	0.185	0.0788	14.6
M5 potential	2732.9	206.9	0.188	0.0782	12.3
Uncertainty	6.0	5.0	0.008	0.004	10.0
Ne·D^{35}Cl					
Experimental	2696.44	183.07	0.4203	0.1972	73.2
M4 potential	2694.4	182.6	0.427	0.1963	62.5
M5 potential	2695.7	183.3	0.425	0.1968	53.4
Uncertainty	6.0	5.0	0.008	0.004	10.0
Ar·H^{35}Cl					
Experimental	1678.511	20.0	0.6733	0.3406	23.7
M5 potential	1679.5	20.2	0.653	0.340	21.0
Uncertainty	2.0	0.5	0.02	0.002	2.0
Ar·D^{35}Cl					
Experimental	1656.19	17.1	0.8331	0.5370	19.0
M5 potential	1655.5	16.7	0.808	0.538	19.1
Uncertainty	2.0	0.5	0.027	0.002	3.0
Kr·H^{35}Cl					
Experimental	1200.624	7.34	0.7659	0.4324	10.8
M5 potential	1199.7	7.66	0.731	0.429	8.8
Uncertainty	3.0	0.2	0.032	0.040	1.5

Table 3 (continued)

	B/MHz	D_J/kHz	$\langle P_1(\cos\theta)\rangle$	$\langle P_2(\cos\theta)\rangle$	D_θ/ppm
Kr·D^{35}Cl					
Experimental	1182.72	6.51	0.8799	0.6055	10.7
M5 potential	1182.3	6.37	0.844	0.607	7.3
Uncertainty	3.0	0.2	0.040	0.002	3.0
Xe·H^{35}Cl					
Experimental	994.145	3.813	0.8297	0.5141	-
M5 potential	994.2	3.94	0.792	0.513	5.5
Uncertainty	1.5	0.1	0.05	0.002	2.0
Xe·D^{35}Cl					
Experimental	978.48	3.452	-	0.6650	-
M5 potential	977.6	3.31	0.872	0.666	4.6
Uncertainty	1.5	0.1	0.05	0.002	2.0

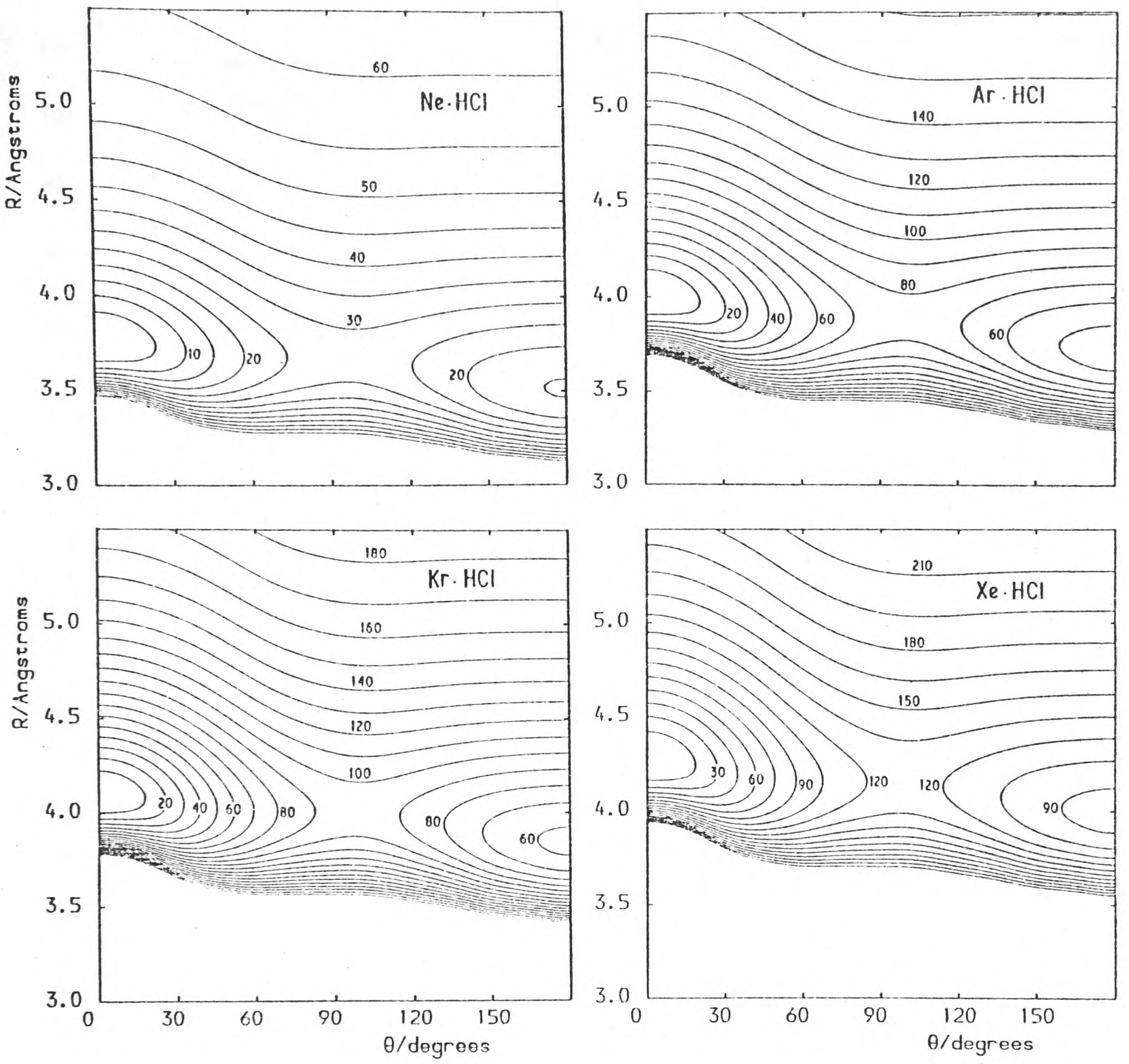

Figure 5. Contour plots of M5 potentials for rare gas - HCl systems. Contours are labelled in wavenumbers relative to the absolute minimum of each potential. Note that the interval between successive contours is not the same for the different systems.

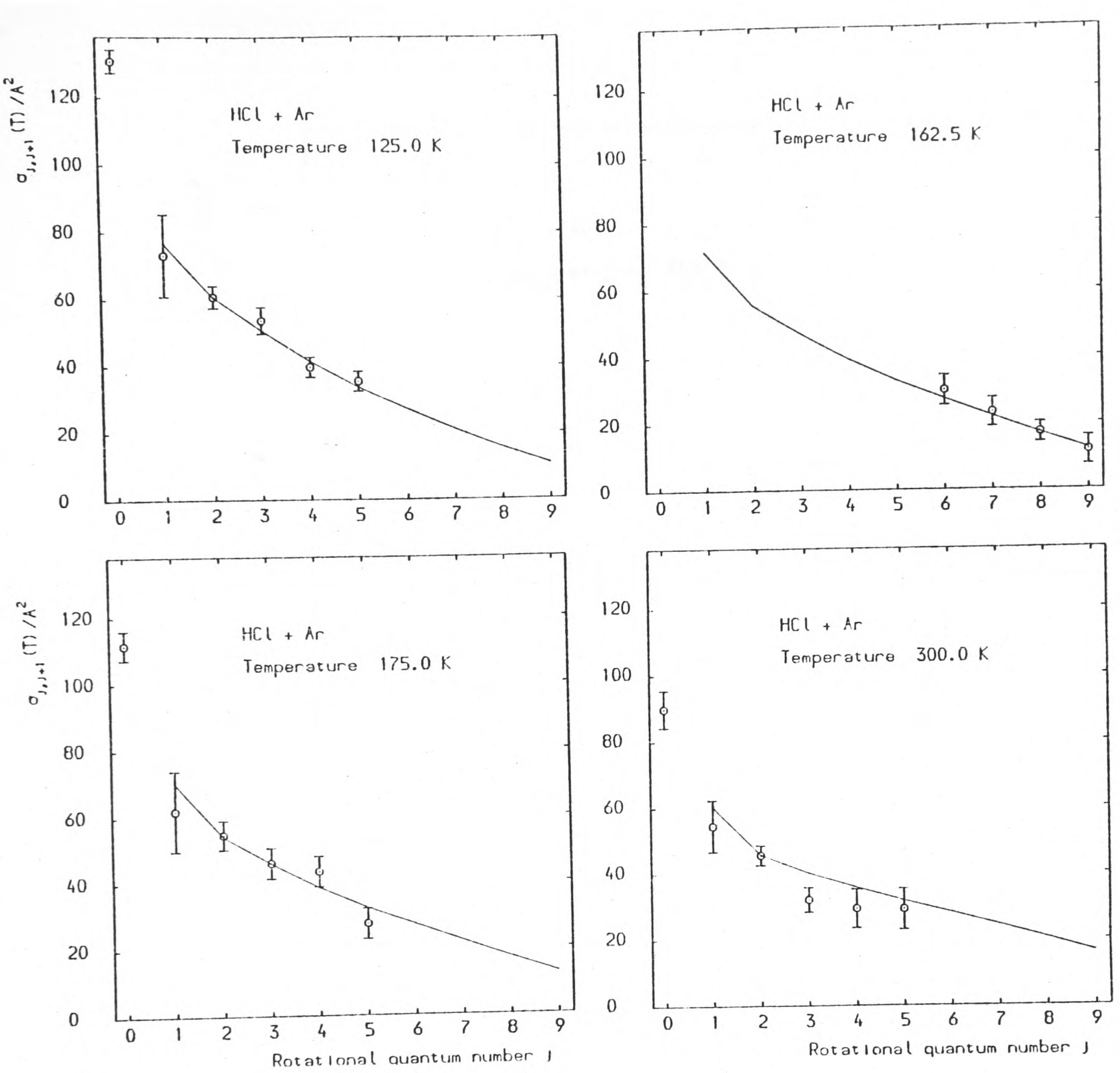

Figure 6. Comparison between experimental and calculated far infrared line broadening cross sections for HCl perturbed by Ar. The points with error bars are the experimental results, and the solid lines are calculated using the M5 potential.

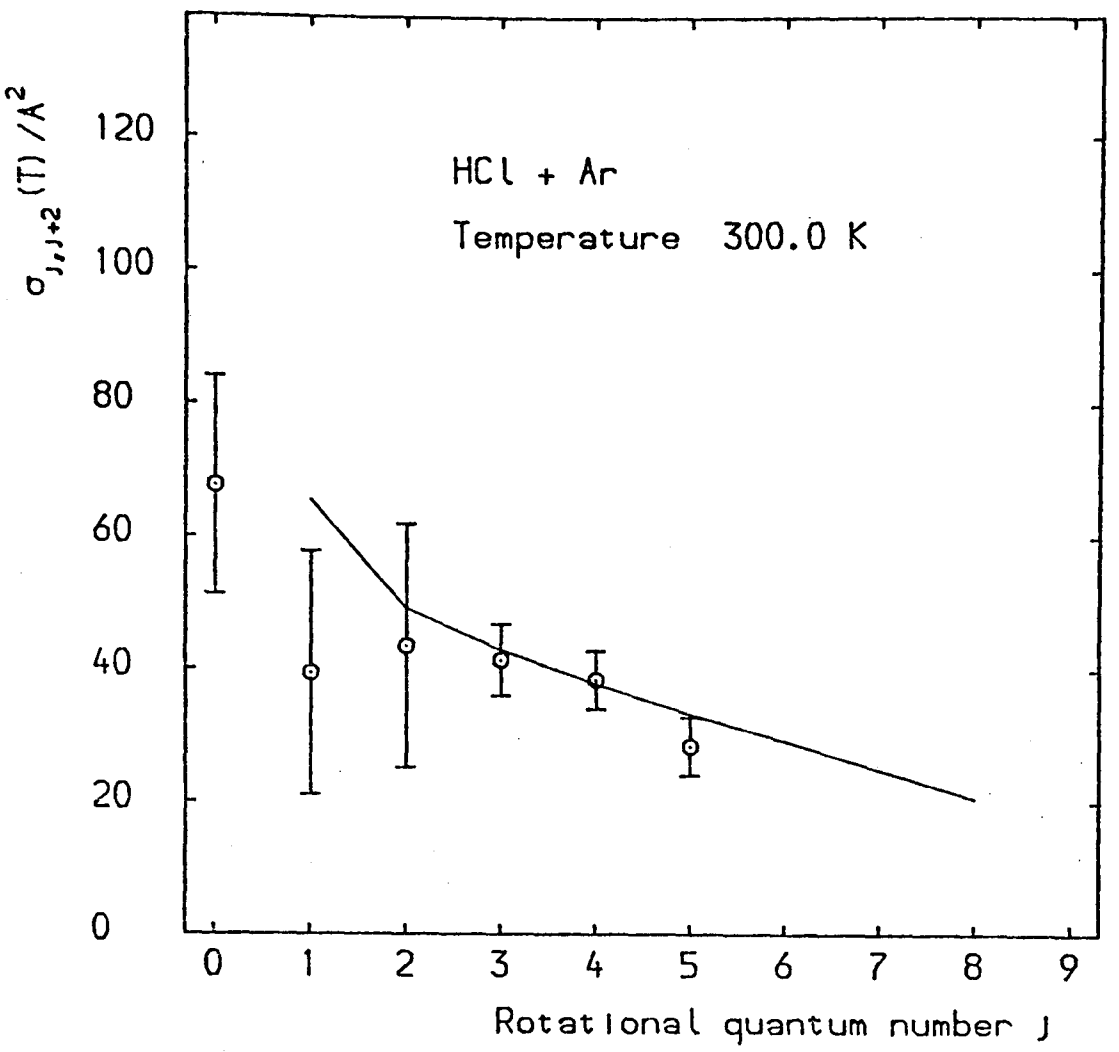

Figure 7. Comparison between experimental and calculated pure rotational Raman line broadening cross sections for HCl perturbed by Ar. The points with error bars are the experimental results, and the solid line is calculated using the M5 potential.

4.5 Kr·HCl and Xe·HCl

Microwave and radiofrequency spectra of the Kr·HCl [11,12] and Xe·HCl [13,14] van der Waals complexes have been reported, and limited data are also available for far infrared lines of HCl perturbed by Kr and Xe [4]. The data are not sufficient to determine as many potential parameters as for Ar·HCl, but nevertheless contain considerable information on the intermolecular potentials. In the least squares fits described below $\varepsilon(0^o)$, $\Delta\varepsilon_1$, λ, $R_m(0^o)$ and ΔR_1 have been floated, and the parameters $m(0^o)$, Δm, κ, ξ and ΔR_2 have been fixed at the Ar·HCl values. The values of $\Delta\varepsilon_2$ were estimated as described in section 4.3.

The parameters of the fitted potentials are given in table 4, and contour plots are shown in figure 5. The fits to the MBER data are summarised in table 3, and the fits to the line broadening cross sections are shown in figure 3. The χ^2 statistic was 45.6 for Kr·HCl (20 data points) and 34.7 for Xe·HCl (12 data points). For Kr·HCl, it may be noted that more than half of the total χ^2 arises from a single data point ($j = 3 \rightarrow 4$ far infrared linewidth at 300K), and it seems possible that this measurement is in error.

None of the data for Kr·HCl and Xe·HCl are directly sensitive to the absolute well depths $\varepsilon(0^o)$, so that these quantities are not reliably determined. They were floated in the least squares fits in order to gain the flexibility necessary to fit the spectroscopic centrifugal disortion constant D_J, which are determined by the radial curvature of the potential near the minimum. However, the curvature is also dependent on the repulsive wall parameters $m(0^o)$ and Δm, which were fixed at the values determined for Ar·HCl. There is evidence from work on the rare gas pair potentials [19] that the wall parameter is approximately independent of the rare gas involved, but the values of $\varepsilon(0^o)$

Table 4. Parameters of M5 potentials for rare gas - HCl systems. Quantities in brackets are one standard deviation.

	Ne·HCl	Ar·HCl	Kr·HCl	Xe·HCl
$\varepsilon(0^{o})/cm^{-1}$	68.22 (0.93)	180.51 (2.72)	213.86 (6.18)	263.61 (10.08)
$\Delta\varepsilon_1/cm^{-1}$	-28.72 (0.28)	-79.35 (4.56)	-97.05 (3.19)	-127.60 (7.89)
λ	4.62 (0.18)	4.04 (0.31)	4.61 (0.37)	4.66 (0.59)
$\Delta\varepsilon_2/cm^{-1}$	14.0	34.0	39.0	43.0
$R_m(0^{o})/pm$	376.38 (1.36)	400.93 (2.93)	409.90 (1.81)	427.42 (2.20)
$\Delta R_1/pm$	-8.87 (1.59)	-12.34 (2.77)	-9.40 (2.94)	-11.71 (4.06)
κ	12.7	12.11 (5.83)	12.7	12.7
$\Delta R_2/pm$	-16.0	-16.0	-16.0	-16.0
$m(0^{o})$	22.2	22.39 (2.93)	22.2	22.2
Δm	-9.6	-9.93 (2.52)	-9.6	-9.6
ξ	16.4	17.25 (9.66)	16.4	16.4
γ	9.0	9.0	9.0	9.0

determined here for Kr·HCl and Xe·HCl are nevertheless strongly correlated with the values assumed for $m(0^{o})$ and Δm. Further experiments are necessary to provide reliable information on the absolute well depths.

4.6 Comparison of potentials

The potentials obtained for the four rare gas - HCl systems may be seen from figure 5 to be very similar in form. It has been found for

the rare gas pairs that the potentials for different systems are very nearly conformal, differing only in energy and length scaling factors [24]; this gives rise to the principle of corresponding states for gas phase properties, whereby the equation of state and transport properties, in reduced units, are the same for all conformal systems. It is of interest to investigate to what extent a similar conformality principle holds in anisotropic systems. Tang and Toennies [25] have investigated the rare gas - H_2 systems from this point of view, and found that both the isotropic and anisotropic potentials were individually nearly conformal, although the ratio of the anisotropic and isotropic well depths $\varepsilon_2/\varepsilon_0$ was different for different rare gases. For the rare gas - HCl potentials obtained here, some parameters were constrained to be conformal as described above, but the most important potential parameters were determined independently for each system, so that the potentials for the different rare gases may reasonably be compared with one another.

4.6.1 The repulsive potential

The repulsive interactions are principally characterised by the value of R at which the potential passes through zero at each angle θ. This quantity is denoted σ, and is most usefully referred to the distance of the rare gas atom from the H or Cl nucleus as appropriate, rather than to the distance from the centre of mass of the HCl molecule. At the linear Rg·H-Cl geometry the repulsive forces are dominated by the Rg·H interaction; values of the quantity σ(Rg·H) are given for the M5 potentials for the four systems in table 5. Also tabulated is r_H, which is a measure of the effective radius of the

Table 5. Derived potential parameters (see section 4.6 for explanation)

	Ne.HCl	Ar.HCl	Kr.HCl	Xe.HCl
σ(Rg-H)/pm	221.9	244.7	252.8	268.9
r_H/pm	83.8	77.2	73.8	74.8
σ(Rg-Cl)/pm	326.7	345.4	356.0	369.6
r_{Cl}/pm	188.6	177.9	177.0	175.5
barrier height/cm^{-1}	27.87	76.10	94.30	124.27
barrier/$\varepsilon(0^o)$	0.41	0.42	0.44	0.47
$C_6(90^o)/10^{17} cm^{-1} pm^6$	1.00	3.66	4.98	7.28
C_6(Rg·Ar)/$10^{17} cm^{-1} pm^6$	0.99	3.26	4.56	6.84

hydrogen atom in HCl and is defined by

$$\sigma(Rg \cdot H) = r_{Rg} + r_H$$

where r_{Rg} is obtained from the appropriate rare gas pair potential [19]

$$r_{Rg} = \tfrac{1}{2}\,\sigma(Rg \cdot Rg) \,.$$

The values of r_H decrease steadily down the series from Ne to Xe, as the influence of the attractive forces increases. All the values of r_H are markedly smaller than the corresponding values for the rare gas - H_2 complexes [26]: in Ar·H_2, for example, r_H = 115 pm. The attractive forces in Ar·H_2 are similar to those in Ne·HCl, so that this reduction in r_H reflects a real decrease in the "size" of the hydrogen atom in HCl compared to that in H_2.

The repulsive forces due to the Rg·Cl interaction may similarly be characterised by σ(Rg·Cl), which is most reliably determined from the potential at $\theta = 90^{o}$. This may be partitioned in the same way as before

$$\sigma(Rg\cdot Cl) = r_{Rg} + r_{Cl}$$

and values of σ(Rg·Cl) and r_{Cl} are given in table 5. r_{Cl} again decreases steadily from Ne to Xe as the attractive forces increase in importance. It is slightly larger than r_{Ar} (167.5 pm) for all the complexes considered here, but this is partially an artefact of considering the potential at $\theta = 90^{o}$: r_{Cl} at $\theta = 180^{o}$ is approximately 20 pm lower, which accounts for most of the differences. The chlorine atom in HCl is to a reasonably good approximation the same size as an argon atom.

4.6.2 The attractive potential

The most striking feature of all the potentials is that the minimum is at $\theta = 0^{o}$, despite the repulsive forces due to hydrogen, but there is no evidence for a corresponding peak in the coefficients of the long range attractive forces near $\theta = 180^{o}$. Although there is probably a secondary minimum around $\theta = 180^{o}$, it appears to arise from a decrease in the repulsive forces there, rather than from increased attractive forces. This supports a site-site model for the attractive potential, with approximately additive Rg·H and Rg·Cl attractive forces.

On this model, the attractive potential at $\theta = 90^{o}$ would be dominated by the Rg·Cl dispersion forces, which would be expected to be similar to the near-isoelectronic Rg·Ar dispersion forces. The long range C_6 coefficients for the Rg·Ar interactions may be accurately calculated from

oscillator strength sum rules [27], and the C_6 coefficients for the Rg·HCl potentials at $\theta = 90^{o}$ may be estimated from equation (9). This relationship relies on the validity of the Maitland-Smith potential for the rare gas - HCl systems, which is not fully established. Nevertheless the prescription yields semiquantitative values of C_6(Rg·Cl), and these are compared with values of C_6(Rg·Ar) in table 5. The values obtained agree to within 15%, which supports the model of additive atom-centred dispersion forces.

The anisotropy of the attractive forces is conveniently characterised by the height of the barrier to internal rotation of HCl in the complex, defined as the energy difference between the saddle point in the potential near $\theta = 90^{o}$ and the absolute minimum. This quantity is tabulated in table 5. The ratio of the barrier height to the absolute well depth increases steadily from Ne to Xe for these potentials, although it is possible that this is due to uncertainties in the optimised values of $\varepsilon(0^{o})$. A similar result was obtained by Tang and Toennies [25] for the rare gas - H_2 potentials, where the ratio of the anisotropic and isotropic well depths $\varepsilon_2/\varepsilon_0$ increased steadily from 0.075 for He·H_2 to 0.119 for Xe·H_2. The potential surfaces for rare gas - HCl systems alone are not sufficient to establish the detailed origin of the attractive forces near $\theta = 0^{o}$, and a discussion of this will be postponed until the next chapter, where results for HF and HBr complexes are analysed.

4.7 Vibrationally excited states

Molecular beam spectra of rare gas - HCl complexes are available only for the vibrational ground state of each complex, and this limits the

region of the potentials which can be reliably determined from the spectra. However, an experiment currently being developed [28] should allow the observation of spectroscopic transitions involving excitation of the van der Waals vibrational modes at high resolution, and it is of interest to investigate how such spectra would be related to the intermolecular potential.

As discussed in chapter 2, the energy levels of rare gas - hydrogen halide complexes are characterised by three approximate quantum numbers, in addition to the total angular momentum J. These are a bending quantum number b, which correlates in the isotropic limit with the HCl rotational quantum number j; the helicity quantum number K, which is the projection of both J and j onto the molecular axis; and s, the stretching quantum number for the van der Waals bond. The most intense spectroscopic transitions between these states are expected to be those following the propensity rules

$$\Delta b = \pm 1$$

$$\Delta K = 0, \pm 1$$

$$\Delta s = 0$$

with the additional rotational selection rule $\Delta J = \pm 1$ for parallel bands ($\Delta K = 0$) and $\Delta J = 0, \pm 1$ for perpendicular bands ($\Delta K = \pm 1$).

Calculations of the energies of the lowest four vibrational states of each complex have been carried out using the artificial channel method [29], and the results are given in table 6. Energy levels of Ar·HCl on the VR and HWK potentials have been calculated previously by Kidd et al. [30]; however, the results given here for the VR potential differ slightly because we have used a different rotational constant for HCl. In the present calculations, the potentials were expanded in Legendre

polynomials including all terms up to $P_9(\cos\theta)$, and the basis set of spherical harmonics used $j_{max} = 8$. The results are converged to $0.001\ cm^{-1}$. The energy levels given in table 6 are for $J = 0$ for all states except $(b,K,s) = (1,1,0)$, where the $J = 1$ level is quoted. Quantum numbers have been assigned to the energy levels by comparison with reversed Born-Oppenheimer calculations.

Before considering the results for individual potentials, it is helpful to consider the effect of anisotropic potentials proportional to $P_1(\cos\theta)$ and $P_2(\cos\theta)$ individually on a simple hindered rotation problem. Using the hamiltonians

$$\hat{H}_1 = b\hat{j}^2 - V_1 P_1(\cos\theta)$$

and

$$\hat{H}_2 = b\hat{j}^2 - V_2 P_2(\cos\theta)$$

the dependence of the lowest energy levels on the anisotropy is as shown in figure 8. The left hand side of the figure shows the effect of a pure

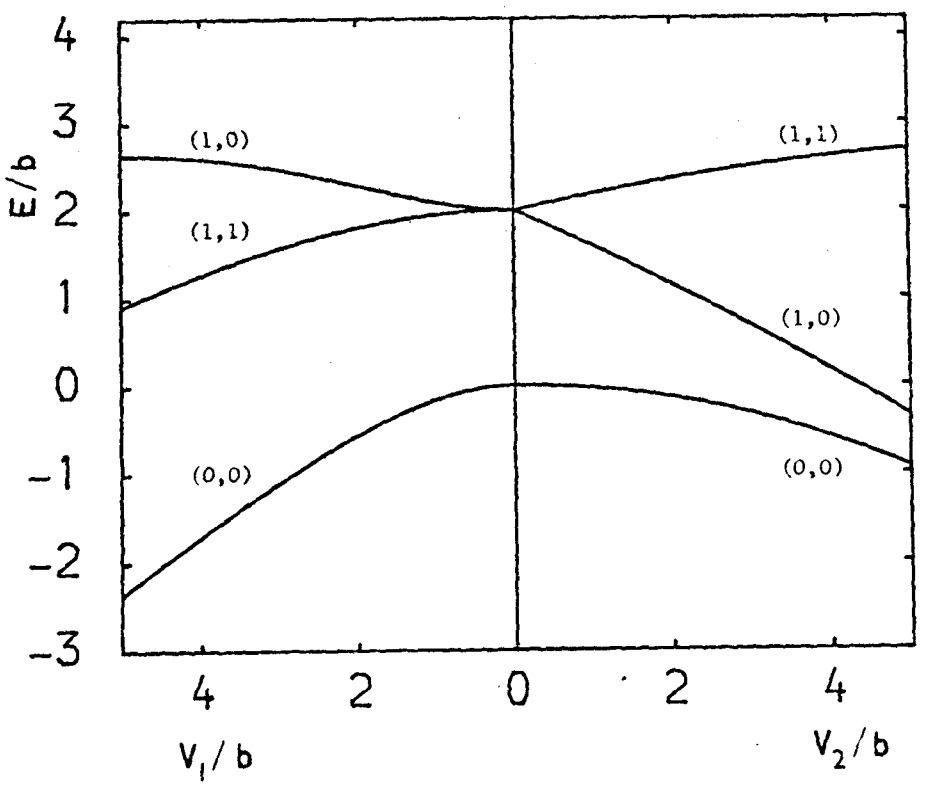

Figure 8. Effect of pure V_1 and V_2 potentials on hindered rotor. All energies are in units of the diatom rotational constant. Energy levels are labelled by (b,K) quantum numbers.

Table 6. Excited state energies and transition frequencies for rare gas - HCl complexes. States are labelled with the approximate quantum numbers (b,K,s).

Potential		State energies/cm^{-1}				Transition frequencies/cm^{-1}		
		(0,0,0)	(1,0,0)	(1,1,0)	(0,0,1)	parallel bend	perpendicular bend	stretch
Ne·HCl	M4	-35.706	-19.025	-11.973	-15.680	16.681	23.733	20.026
Ne·HCl	M5	-35.095	-18.155	-11.499	-15.366	16.940	23.596	19.729
Ar·HCl	VR	-95.430	-79.403	-66.262	-68.179	16.027	29.168	27.251
Ar·HCl	HWK	-128.354	-91.035	-92.932	-98.952	37.319	35.422	29.402
Ar·HCl	M3	-118.546	-90.180	-85.251	-84.411	28.366	33.295	34.135
Ar·HCl	M5	-117.126	-92.220	-82.034	-83.657	24.907	35.092	33.469
Kr·HCl	M5	-142.595	-112.932	-101.354	-109.305	29.663	41.241	33.290
Xe·HCl	M5	-180.862	-134.176	-129.364	-147.077	46.686	51.498	33.785

V_1 (single minimum) potential, and the right hand side that of a pure V_2 (double minimum) potential. It may be seen that for a V_1 potential the (b,K) = (1,0) state lies above the (1,1) state, whereas for a V_2 potential the order is reversed. For realistic potentials both V_1 and V_2 components are present, and the situation is further complicated by the stretching motion, but the relative excitation energies for the (1,0) and (1,1) states nevertheless provide important information on the intermolecular potentials.

This effect may be clearly seen when the transition frequencies for Ar·HCl on the VR, M5 and M3 potentials are compared. The VR potential has the strongest secondary minimum of the three, and the parallel bending frequency in this case is only just over half that for the perpendicular band. For the M5 and M3 potentials, the difference between the two excitation frequencies becomes progressively less as the depth of the secondary minimum decreases.

The HWK potential is somewhat anomalous, since the interaction between the stretch and the parallel bend is particularly strong in this case. The (1,0,0) and (0,0,1) states are strongly mixed, with the result that one energy level is displaced upwards and the other downwards; for the HWK potential, the parallel bending frequency is higher than would otherwise be expected, and the stretching frequency is lower. A similar effect occurs for Kr·HCl on the M5 potential, and it is again difficult to assign quantum numbers reliably to the (1,0,0) and (0,0,1) states. If this effect occurs for the real intermolecular potential, it will result in the stretching transition becoming more strongly allowed by borrowing intensity from the parallel bending transition.

Far infrared spectra of rare gas - HCl complexes have been observed at low resolution in bulk gas mixtures by Boom and van der Elsken [31].

Their spectra were taken under conditions where many vibrational and rotational levels of the complexes were populated, and it is not possible to assign the bands observed. However, the transition frequencies obtained experimentally are in qualitative agreement with those predicted from the fitted potentials. Higher resolution spectra are required before a more detailed analysis can be undertaken. However, it is clear that spectroscopic characterisation of the van der Waals bending states of these complexes will provide very valuable information on the intermolecular potential, and in particular will resolve the question of the depth of the secondary minimum at $\theta = 180^{o}$.

4.8 Predictions for second virial coefficients

Second virial coefficients $B_{12}(T)$ have been calculated for the Ne·HCl, Ar·HCl, Kr·HCl and Xe·HCl potentials derived above, and the results are shown in figure 9. Measurements of these quantities would provide very useful information on the absolute well depths in the Ne, Kr and Xe complexes, since the other potential parameters contributing to the second virial coefficients are quite accurately determined.

4.9 Predictions for Raman line broadening cross sections

Cross sections for broadening of HCl pure rotational Raman lines by rare gases have been carried out using the best fit potentials described above, and the results are shown in figure 10. Measurements of these quantities would provide a useful test of the potentials, although it appears that Raman linewidths are sensitive to much the same potential features as infrared linewidths, so that the additional

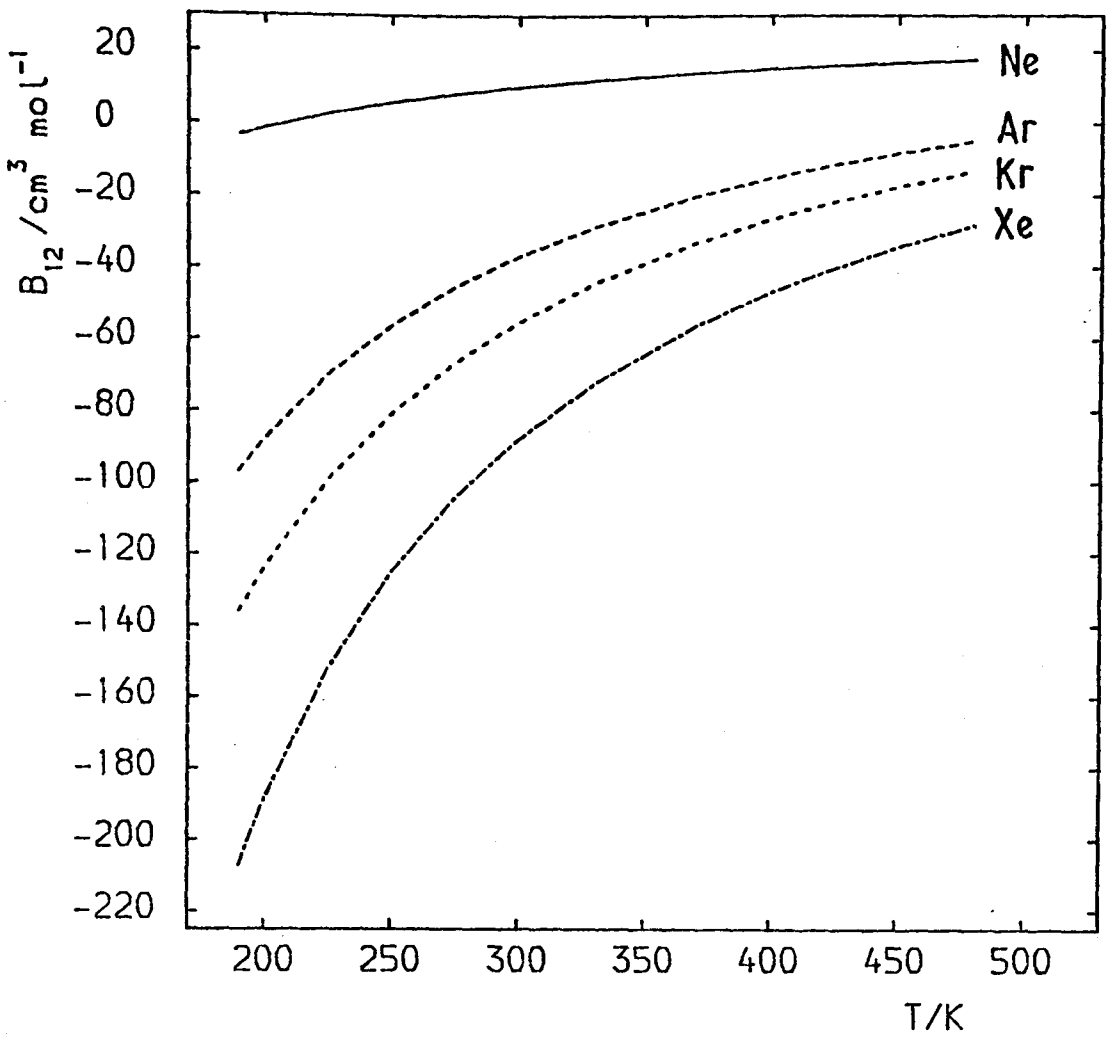

Figure 9. Predictions for second virial coefficients for mixtures of HCl with rare gases, calculated using M5 potentials.

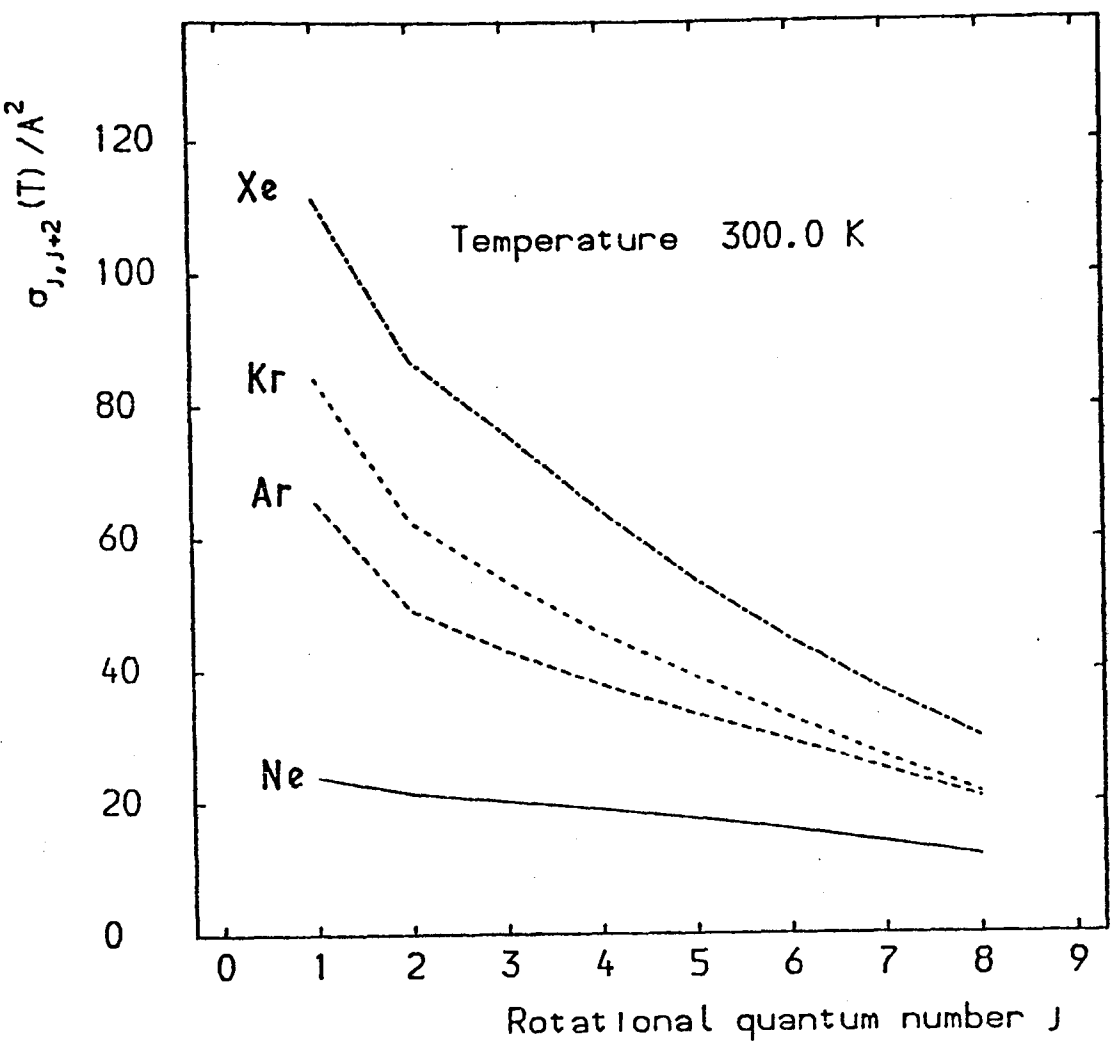

Figure 10. Predictions of pure rotational Raman line broadening cross sections for HCl perturbed by rare gases, calculated using M5 potentials.

information available from Raman measurements is limited.

Conclusion

In this chapter, potential surfaces have been derived for the systems Ne·HCl, Ar·HCl, Kr·HCl and Xe·HCl, using all available experimental data. All the potentials have their absolute minimum at the linear Rg·H-Cl geometry. The molecular beam spectra for Ne·HCl can be reproduced only by a potential with a significant secondary minimum at the linear Ne·Cl-H configuration. The available data for the more anisotropic systems Ar·HCl, Kr·HCl and Xe·HCl are relatively insensitive to the presence of this potential feature, so potentials for these have been obtained by assuming that the potential in this region behaves in a manner analogous to that found for Ne·HCl.

The potentials obtained gave satisfactory agreement with all the available data, and should be reliable near the absolute minimum and on the repulsive wall. The features which are not well determined by the data currently available are the absolute depths of the potential wells (for Ne·HCl, Kr·HCl and Xe·HCl), and the depths of the secondary minima near the linear Rg·Cl-H configurations (for Ar·HCl, Kr·HCl and Xe·HCl). Further information on the absolute well depths would be provided by measurements of molecular beam differential cross sections or mixed second virial coefficients, and on the depths of the secondary minima by spectroscopic characterisation of the excited bending states of the van der Waals complexes.

REFERENCES

1. S.E. Novick, P. Davies, S.J. Harris and W. Klemperer, J. chem. Phys. 59, 2273 (1973).

2. S.E. Novick, K.C. Janda, S.L. Holmgren, M. Waldman and W. Klemperer, J. chem. Phys. 65, 1114 (1976).

3. J.M. Hutson and B.J. Howard, J. chem. Phys. 74, 6520 (1981).

4. R.M. van Aalst, J. Schuurman and J. van der Elsken, Chem. Phys. Lett. 35, 558 (1975).

5. D. Frenkel, D.J. Gravesteyn and J. van der Elsken, Chem. Phys. Lett. 40, 9 (1976): D. Frenkel, Ph.D. thesis, Amsterdam (1977).

6. G.J.Q. van der Peijl, D. Frenkel and J. van der Elsken, Chem. Phys. Lett. 56, 602 (1978).

7. B. Schramm and U. Leuchs, Ber. Bunsenges. phys. Chem. 83, 847 (1979).

8. J.M. Farrar and Y.T. Lee, Chem. Phys. Lett. 26, 428 (1974).

9. A.E. Barton, D.J.B. Howlett and B.J. Howard, Molec. Phys. 41, 619 (1980).

10. J.M. Prout, Part II BA thesis, Oxford University (1981).

11. A.E. Barton, T.J. Henderson, P.R.R. Langridge-Smith and B.J. Howard, Chem. Phys. 45, 429 (1980).

12. T.J. Balle, E.J. Campbell, M.R. Keenan and W.H. Flygare, J. chem. Phys. 72, 922 (1980).

13. K.V. Chance, K.H. Bowen, J.S. Winn and W. Klemperer, J. chem. Phys. 70, 5157 (1979).

14. M.R. Keenan, L.W. Buxton, E.J. Campbell and W.H. Flygare, J. chem. Phys. 73, 3523 (1980).

15. H.E. Scott, Ph.D. thesis, Ohio State University (1973).

16. G.C. Maitland and E.B. Smith, Chem. Phys. Lett. 22, 443 (1973).

17. M. Waldman and R.G. Gordon, J. chem. Phys. 71, 1340 (1979).

18. P.E. Cade, R.F.W. Bader, W.H. Henneker and I. Keaveny, J. chem. Phys. 50, 5313 (1969).

19. C.A. Linse, J.J.H. van den Biesen, E.H. van Veen and C.J.N. van den Meijdenberg, Physica A 99, 166 (1979); J.J.H. van den Biesen, F.A. Stokvis, E.H. van Veen and C.J.N. van den Meijdenberg, Physica A 100, 375 (1980).

20. G. Starkschall and R.G. Gordon, J. chem. Phys. 54, 663 (1971).

21. U. Buck and J. Schleusener, J. chem. Phys. to be published.

22. R.T. Pack, Chem. Phys. Lett. 55, 197 (1978).

23. J.A. Vliegenthart and A. Rozendaal, private communication quoted in reference 30.

24. D.W. Gough, G.C. Maitland and E.B. Smith, Molec. Phys. 27, 867, (1974).

25. K.T. Tang and J.P. Toennies, J. chem. Phys. 74, 1148 (1981).

26. R.J. Le Roy, J.S. Carley and J.E. Grabenstetter, Faraday Discus. Chem. Soc. 62, 169 (1977); J.S. Carley, Ibid. 62, 303 (1977).

27. G. Starkschall and R.G. Gordon, J. chem. Phys. 54, 663 (1971).

28. J.G. Frey, N.P.C. Simmons and B.J. Howard, unpublished work.

29. M. Shapiro, J. chem. Phys. 56, 2582 (1972); M. Shapiro and G.G. Balint-Kurti, J. chem. Phys. 71, 1461 (1979).

30. I.F. Kidd, G.G. Balint-Kurti and M. Shapiro, Faraday Discus. R. Soc. Chem. 71/22 (1981).

31. E.W. Boom and J. van der Elsken, J. chem. Phys. 73, 15 (1980).

CHAPTER 5

SYSTEMS CONTAINING HF AND HBr

CHAPTER 5

SYSTEMS CONTAINING HF AND HBr

In the preceding chapter, anisotropic potential energy surfaces were obtained for the systems Ne·HCl, Ar·HCl, Kr·HCl and Xe·HCl, and the dependence of the intermolecular potential on the rare gas atom was considered. In this chapter, potentials will be obtained for the systems Ar·HF, Kr·HF and Xe·HF, allowing the dependence of the potential on the hydrogen halide molecule to be investigated. It is also possible to obtain limited information on the systems Ar·HBr and Kr·HBr.

Molecular beam rotational spectra have been measured for Ar·HF [1,2], Kr·HF [3], Xe·HF [4], Ar·HBr [5,6] and Kr·HBr [6]. There are no published far infrared line broadening data or second virial coefficients for these systems, although Barnes et al. [7] have recently reported state-to-state integral cross sections for HF colliding with Ne, Ar and Kr at high energies ($E > 1400$ cm^{-1}). These measurements undoubtedly contain useful information on the anisotropy of the repulsive wall of the Rg·HF potentials, but unfortunately became available too late to be included in the present study. There have also been theoretical calculations on the Ar·HF system [8], and Becker et al. [9] have reported total differential cross sections for scattering of HF by Xe.

5.1 Constraints on the potentials

The parameterisation of the intermolecular potential used in this chapter is exactly the same as in chapter 4, but different parameters were floated here because the information contained in the experimental results is somewhat different. The molecular beam spectra contain information primarily on the anisotropy of the well depth function $\varepsilon(\theta)$

and on the radial minimum function $R_m(\theta)$ near the linear Rg·H-X configuration. There is very little information on the absolute well depth or on the potential near $\theta = 180^o$. Nevertheless, it is possible to obtain potential energy surfaces for the Rg·HF systems if the undetermined features of the potential are fixed using information from the Rg·HCl systems. The principal features of the surfaces obtained in this way are reliably determined, and the potentials may be compared with those obtained previously for the Rg·HCl systems.

5.1.1 Absolute well depths

The absolute well depths are not well determined by the rotational spectra, although the centrifugal distortion constants D_J do contain information on the radial curvature of the well, which depends partly on the depth. However, it was found for HCl complexes that the potential at $\theta = 90^o$ was well represented by a Maitland-Smith potential with a long range C_6 coefficient the same as for the isoelectronic rare gas - rare gas interaction. If similar behaviour is assumed for the HF complexes, the well depths at $\theta = 90^o$ may be estimated, as shown in Table 1. This model allows only for the dispersion contribution to the attractive potential, but for HF complexes there is also expected to be a significant contribution from induction forces, as described in chapter 6: the values of $\varepsilon(90^o)$ for Ar·HF, Kr·HF and Xe·HF have accordingly been fixed at 67 cm^{-1}, 79 cm^{-1} and 91 cm^{-1} respectively in the least squares fits. At each step of the least squares fits described below, the parameter $\varepsilon(0^o)$ was calculated from the expression

$$\varepsilon(0^o) = \varepsilon(90^o) - \Delta\varepsilon_1 \, f(90^o;\lambda) \; .$$

Table 1. Well depths at $\theta = 90^{o}$ calculated from isoelectronic rare gas - rare gas C_6 coefficients

	Ar·HF	Kr·HF	Xe·HF	Ar·HBr	Kr·HBr
C_6 (rare gas - rare gas) /10^{17} $cm^{-1}pm^6$	0.99	1.36	2.02	4.56	6.41
R_m (90^{o})/pm	346	355	375	400	411
ε (90^{o})/cm^{-1}	57.7	67.9	72.6	111.3	133.0

5.1.2 Secondary minimum at $\theta = 180^{o}$

For the HCl complexes, and secondary minimum was modelled by assuming that the attractive forces were isotropic beyond $\theta = 90^{o}$, but that the repulsive forces at $\theta = 180^{o}$ were weaker than those at $\theta = 90^{o}$. A similar treatment is possible for the complexes of HF, for which a contour plot of the total electron density is also available [10]. The parameter ΔR_2 has been estimated from this to be -11 pm for HF complexes, relative to the HF centre of mass. The induction contribution to the attractive forces is expected to be similar at $\theta = 90^{o}$ and $\theta = 180^{o}$ (see chapter 6): if the dispersion forces are also isotropic beyond $\theta = 90^{o}$, this allows $\Delta\varepsilon_2$ for Ar·HF, Kr·HF and Xe·HF to be estimated as 16 cm^{-1}, 17 cm^{-1} and 22 cm^{-1} respectively. These secondary minima are considerably shallower than for the corresponding HCl complexes, both because the dispersion forces around $\theta = 180^{o}$ are weaker in the HF systems, and because ΔR_2 is smaller for HF.

In the case of HBr, contour plots of the electron density are not available, so that it is difficult to make reliable estimates of the parameters ΔR_2 and $\Delta\varepsilon_2$ for HBr complexes. However, the rotational spectra do contain some useful information on the potential near $\theta = 0^{o}$, and this is discussed below.

5.1.3 Repulsive anisotropy

The anisotropy of the repulsive wall near $\theta = 0^{o}$ is characterised by four potential parameters: ΔR, κ, Δm and ξ. The spectra contain enough information to determine only one of these for each system. The bond lengths of the hydrogen halides increase faster than the van der Waals radii down the periodic table, so that it is reasonable to expect ΔR_1 to change considerably between HF and HBr, although it should be relatively insensitive to the rare gas involved. In the fits described below, ΔR_1 has been floated while κ, Δm and ξ have been fixed at the same values as were used for the HCl systems in chapter 4.

These constraints give a potential form with 5 free parameters: $\Delta\epsilon_1$, λ, $m(0^{o})$, $R_m(0^{o})$ and ΔR_1. All the other potential parameters were fixed as described above in the least squares fits.

5.2 Potentials for Ar·HF, Kr·HF and Xe·HF

Klemperer and coworkers have measured the microwave and radio-frequency spectra of Ar·HF and Ar·DF [1] and of Xe·HF and Xe·DF [4], and Flygare and coworkers have obtained the microwave spectra of Ar·HF [2] and Kr·HF [3] and their deuterium analogues. Since fluorine does not have a nuclear quadrupole moment, information on the expectation value of $P_2(\cos\theta)$ is derived from the deuterium quadrupole coupling constant (for DF complexes) and from the HF nuclear spin-nuclear spin coupling constant (for HF complexes). These quantities are much smaller than the halogen quadrupole coupling constant in complexes containing Cl and Br, so that the experimental values of $\langle P_2(\cos\theta)\rangle$ are considerably less accurate than for Cl and Br complexes. For the same reason it is not possible to measure the angular centrifugal distortion constants D_θ, which were an important source of information on the angular-radial coupling terms in the potential for the HCl complexes.

Information on the angle dependence of $R_m(\theta)$ can however be obtained from the isotope dependence of the rotational constants B, since the Rg·HF complexes sample a larger angular range of the potential than the corresponding Rg·DF complexes. In order to extract this information, it is necessary to correct the experimental rotational constants for Ar·DF, Kr·DF and Xe·DF for the isotope dependence of the potential, as described for DCl complexes in section 4.1. Details of the corrections used for DF complexes are given in table 2.

Table 2. Corrections applied to rotational constants of DF and DBr complexes (MHz)

	experiment	correction	corrected value
Ar·DF	3039.8529	2.55	3037.31
^{84}Kr·DF	2353.1407	1.96	2351.19
^{129}Xe·DF	1995.469	1.22	1994.25
Ar·D^{79}Br	1087.5089	0.96	1086.55
^{84}Kr·D^{79}Br	675.8486	0.27	675.58

Least squares fits to the spectroscopic data for Ar·HF, Kr·HF and Xe·HF have been performed, and the optimised potential parameters are given in table 3. Contour plots of these potentials are shown in figure 1, and the fits to the data are given in table 4. The quality of fit is characterised by χ^2 = 7.8 for Ar·HF (8 observables), χ^2 = 2.1 for Kr·HF (6 observables), and χ^2 = 1.9 for Xe·HF (8 observables). The higher value of χ^2 for Ar·HF is largely because the experimental uncertainties are lower in this case.

5.3 Potentials for Ar·HBr and Kr·HBr

As described above, there is considerable uncertainty concerning the behaviour of the Ar·HBr and Kr·HBr potentials around the linear Rg·Br-H geometry. However, this region of the potential does not greatly affect the spectroscopic observables, so that it should nevertheless be possible to extract information on the potential around $\theta = 0^{o}$ from the spectra. Unfortunately, preliminary fits revealed that the parameter ΔR_1 for the HBr complexes is much greater than in the HF or HCl complexes, and under these circumstances neither the CBO method

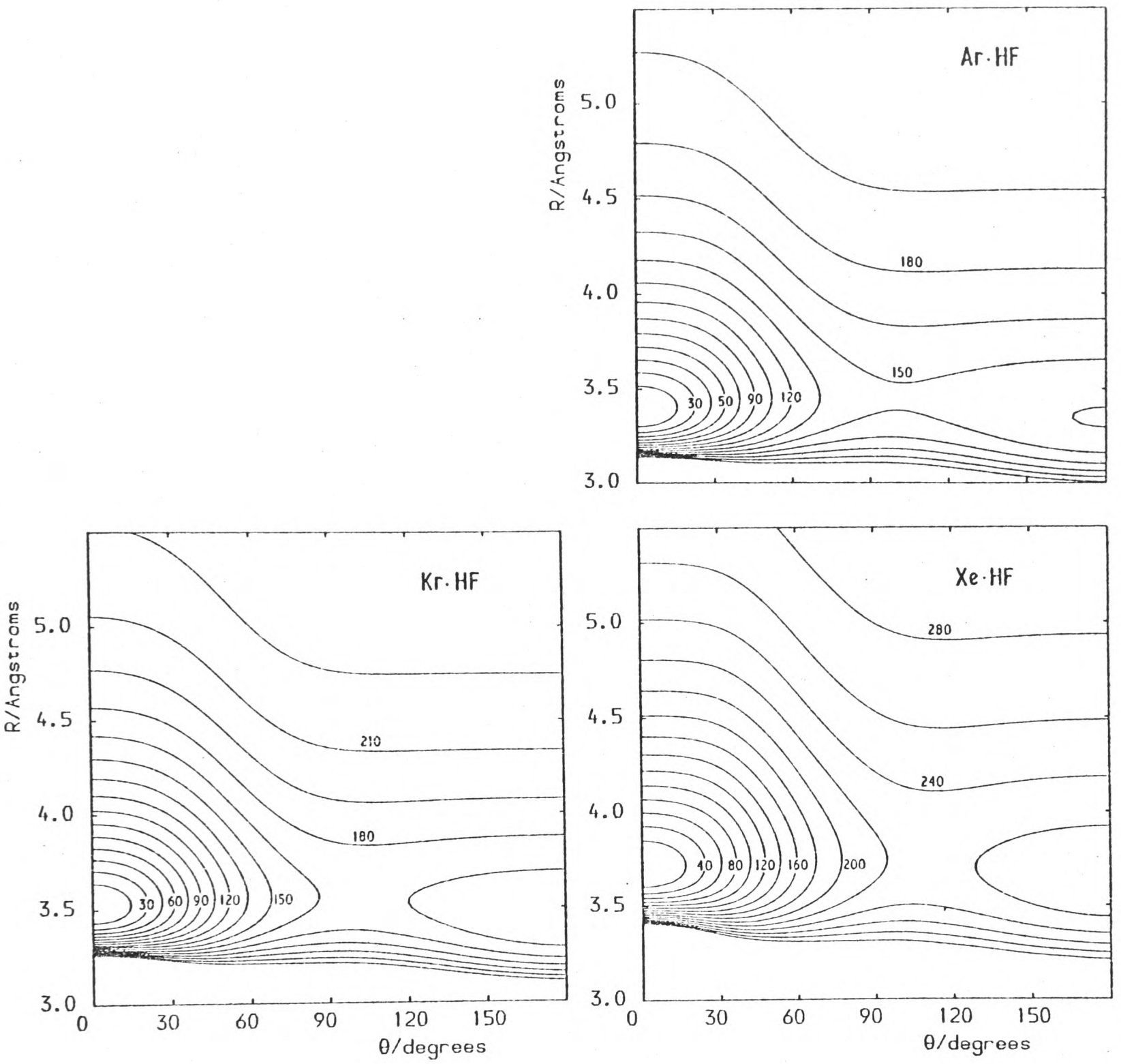

Figure 1. Contour plots of optimised potentials for rare gas - HF systems. Contours are labelled in wavenumbers relative to the absolute minimum of each potential. Note that the interval between successive contours is not the same for the different systems.

Table 3. Angle-dependent potential parameters

	Ar·HF	Kr·HF	Xe·HF	Ar·HBr	Kr·HBr
$\varepsilon(0^{\circ})/cm^{-1}$	214.19	245.49	306.56	-	-
$\Delta\varepsilon_1/cm^{-1}$	-150.18 (2.97)	-169.40 (11.20)	-228.76 (7.07)	-	-
λ	5.65 (0.61)	5.86 (3.01)	4.23 (0.48)	-	-
$\Delta\varepsilon_2/cm^{-1}$	16.00	17.00	22.00	-	-
$R_m(0^{\circ})/pm$	339.04 (1.62)	351.91 (2.11)	370.86 (1.36)	430 (5)	437 (4)
$\Delta R_1/pm$	6.53 (2.88)	4.36 (4.22)	3.65 (2.66)	-29 (7)	-26 (7)
κ	12.70	12.70	12.70	-	-
$\Delta R_2/pm$	-11.00	-11.00	-11.00	-	-
$m(0^{\circ})$	23.89 91.20)	24.51 (3.87)	20.82 (0.97)	-	-
Δm	-9.60	-9.60	-9.60	-	-
ξ	16.40	16.40	16.40	-	-
γ	9.0	9.0	9.0	-	-

Table 4. Fits to data from MBER spectroscopy for HF complexes

	B/MHz	D_J/kHz	$\langle P_1(\cos\theta)\rangle$	$\langle P_2(\cos\theta)\rangle$
Ar·HF				
Experiment	3065.7099	70.90	0.660	0.351
M5 potential	3065.1	74.1	0.663	0.351
Uncertainty	3.0	2.0	0.024	0.004
Ar·DF				
Experiment	3037.31	59.53	0.823	0.555
M5 potential	3037.8	55.1	0.814	0.553
Uncertainty	3.0	2.0	0.033	0.004
^{84}Kr·HF				
Experiment	2392.4152	31.94	-	0.400
M5 potential	2392.5	33.4	0.711	0.406
Uncertainty	3.0	2.0	0.030	0.017
^{84}Kr·DF				
Experiment	2351.19	27.31	-	0.607
M5 potential	2351.0	25.1	0.836	0.594
Uncertainty	3.0	2.0	0.030	0.023
^{129}Xe·HF				
Experiment	2039.690	18.32	0.785	0.493
M5 potential	2039.5	19.0	0.782	0.494
Uncertainty	3.0	1.0	0.055	0.006
^{129}Xe·DF				
Experiment	1994.25	15.87	0.883	0.638
M5 potential	1994.5	14.8	0.859	0.638
Uncertainty	3.0	1.0	0.064	0.004

nor the RA method is sufficiently accurate to extract quantitative information on the anisotropy of the well depth function from the spectra.

The quantities $R_m(0^o)$ and ΔR_1 for the HBr complexes are reasonably well determined from the rotational constants and angular centrifugal distortion constants D_θ, and are given in table 3. These quantities allow the repulsive part of the potential for Ar·HBr and Kr·HBr to be compared with those for HF and HCl complexes below. The height of the barrier to internal rotation of HBr in these complexes is not accurately determined, but is probably about 20% lower than the value for the corresponding HCl complex in each case.

A more accurate method of calculating spectroscopic constants for complexes with very strong angular-radial coupling is required to extract the full information content from the spectra for Ar·HBr and Kr·HBr. At present, the only theoretical methods which are sufficiently accurate are prohibitively expensive in computer time.

5.4 Comparison of potentials

Various quantities derived from the potentials for HF, HCl and HBr complexes are given in table 5: these have been defined in section 4.6. The HF potentials are considerably more anisotropic than their HCl counterparts in the well region, but are less anisotropic on the repulsive wall. The parameter ΔR_1 changes markedly with the hydrogen halide involved; for HF complexes ΔR_1 is about +6 pm (corresponding to a depression in the repulsive wall near $\theta = 0^o$), whereas for HBr complexes ΔR_1 is about -30 pm. This trend may be seen from table 5 to have two distinct contributions

1) The HX bond length increases by 50 pm from HF to HBr, while the van

Table 5. Comparison of potentials

	Ar·HF	Ar·HCl	Ar·HBr	Kr·HF	Kr·HCl	Kr·HBr	Xe·HF
σ(Rg-H)/pm	225.5	244.7	252	237.8	252.8	260	252.5
r_H/pm	58.0	77.2	85	58.8	73.8	81	58.4
σ(Rg-X)/pm	310.0	345.4	347	320.5	356.0	361	3330.0
r_X/pm	142.5	177.9	180	141.5	177.0	182	135.9
Barrier ht./cm^{-1}	148.69	76.10	-	167.94	94.30	-	224.12
Barrier/$\varepsilon(0^o)$	0.69	0.42	-	0.68	0.44	-	0.73

der Waals radius of the halogen atom r_x increases by only 36 pm.

2) A rare gas atom can approach much closer to the hydrogen atom of HF than to that of HBr. This can be attributed to the greater withdrawal of electrons from hydrogen by the more electronegative halogen atoms, but it is nevertheless a remarkably large effect; as mentioned previously, r_H in $Ar \cdot H_2$ is 115 pm.

The values of r_X for HF and HBr complexes are again similar to those for the isoelectronic rare gas atoms. Thus, r_F = 142 pm may be compared with r_{Ne} = 138 pm, and r_{Br} = 181 pm with r_{Kr} = 179 pm.

5.5 Predictions for other experiments

5.5.1 Vibrationally excited states

Calculations of the energies of vibrationally excited states of the HF complexes have been performed using the artificial channel method [11], and the results are shown in table 6. The potentials were expanded in Legendre polynomials includings all terms up to $P_9(\cos\theta)$, and the basis set of spherical harmonics used j_{max} = 8. The calculations for the K = 1 states used the helicity decoupling approximation [12], involving neglect of Coriolis coupling terms of the body-fixed frame. This approximation should move the energy levels by no more than ± 0.005 cm^{-1}.

The transition frequencies for the van der Waals stretching mode increase uniformly as the well depth increases from Ar·HF to Xe·HF, and the bending frequencies also increase as the barrier to internal rotation of HF increases. It may be noted that the perpendicular bending frequency is higher than the parallel bending frequency in Ar·HF and Kr·HF, but the order is reversed for Xe·HF. This reflects the greater accessibility of the secondary minimum around $\theta = 180^{o}$ for

Table 6. Calculated excited state energies and transition frequencies for HF complexes.

States are labelled by the approximate quantum numbers (b,κ,s)

Complex	State energies/cm^{-1}				Transition frequencies/cm^{-1}		
	(0,0,0)	(1,0,0)	(1,1,0)	(0,0,1)	parallel bend	perpendicular bend	stretch
Ar·HF	-91.959	-35.339	-24.252	-51.292	56.620	67.707	40.667
Kr·HF	-113.779	-49.880	-39.186	-71.201	63.899	74.593	42.578
Xe·HF	-167.474	-62.866	-73.045	-121.708	104.608	94.429	45.766

Ar·HF and Kr·HF, as discussed for HCl complexes in section 4.7.

5.5.2 Far infrared linewidths

Calculations of far infrared line broadening cross sections for HF + rare gas mixtures at 300K have been performed using the optimised potentials, and the results are shown in figure 2. Measurements of these linewidths would provide useful information on the potential anisotropy at both large and small intermolecular distances.

5.5.3 Second virial coefficients

Calculations of second virial coefficients for HF + rare gas mixtures have been performed using the optimised potentials, and the results are shown in figure 3. Measurements of second virial coefficients would provide valuable information on the well depths for these systems, which are not well determined by the molecular beam spectra.

Conclusion

In this chapter, intermolecular potential energy surfaces were obtained for the systems Ar·HF, Kr·HF and Xe·HF from molecular beam spectra, and some information was also obtained on the intermolecular potentials for Ar·HBr and Kr·HBr. The experimental data for these systems are sensitive only to the region around the potential minimum, and the potentials should be reliable in this region. Elsewhere, the potentials were forced to assume a particular "physically reasonable"

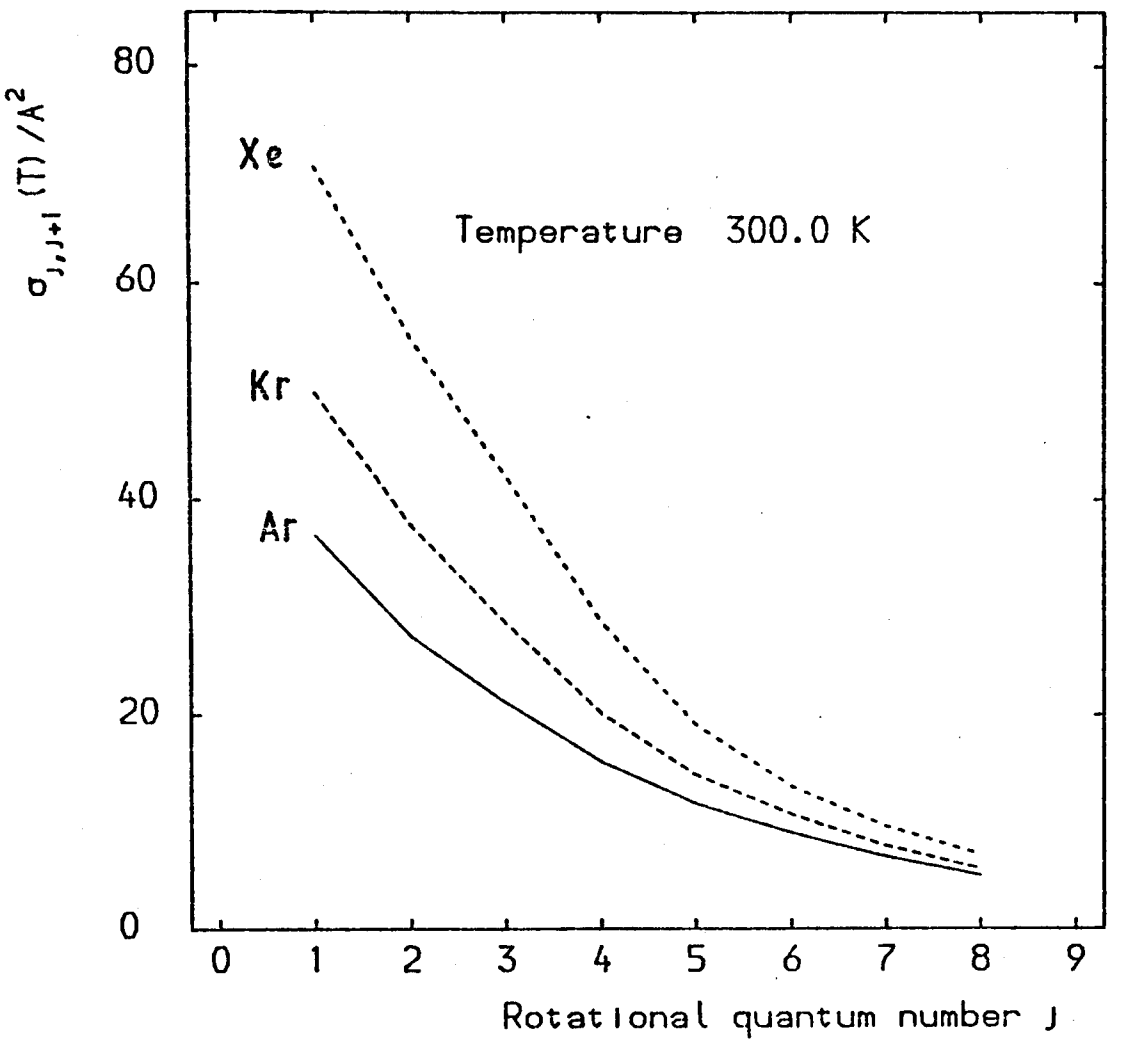

Figure 2. Predictions of far infrared line broadening cross sections for HF perturbed by rare gases, calculated using optimised potentials.

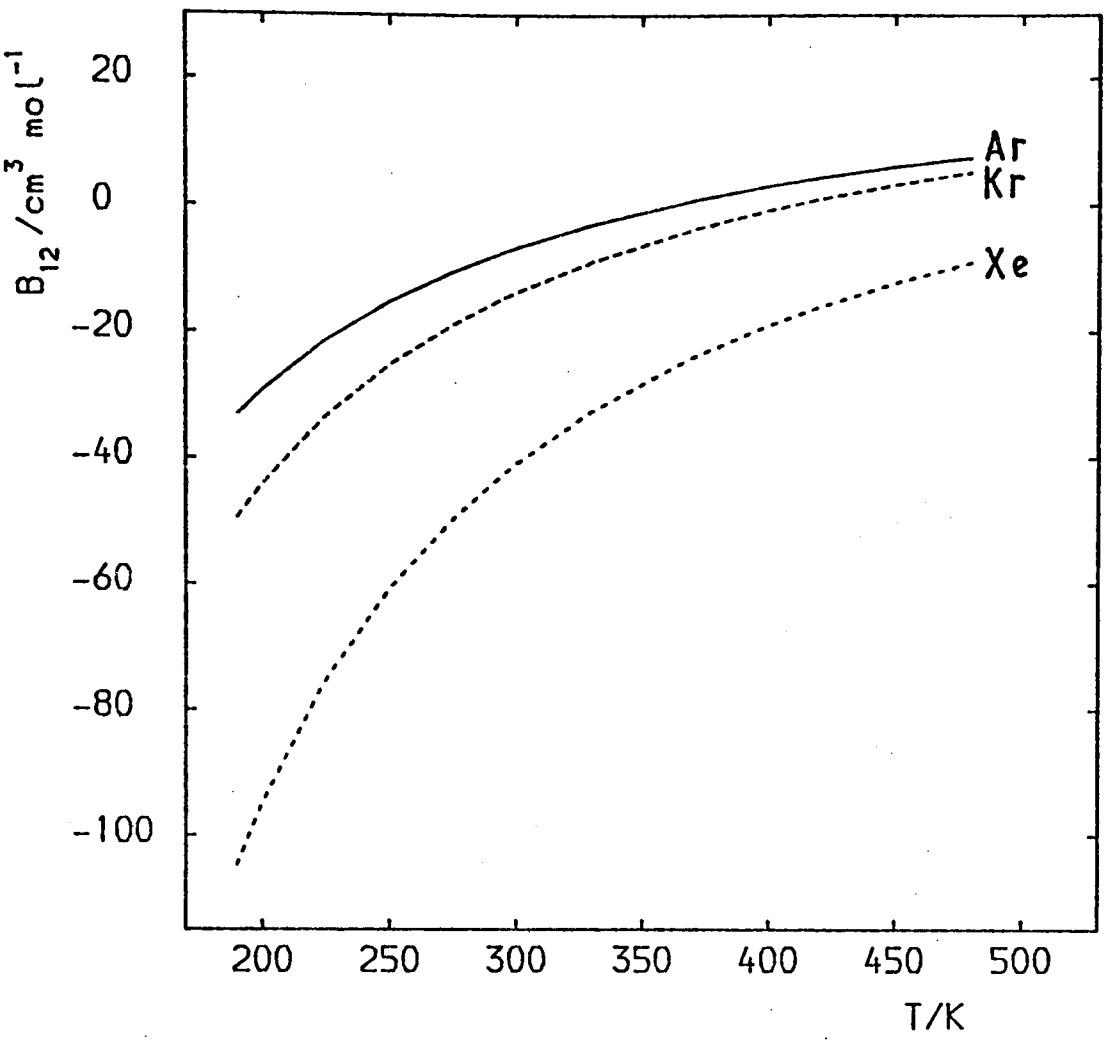

Figure 3. Predictions of second virial coefficients for mixtures of HF with rare gases, calculated using optimised potentials.

form, based on experience with the rare gas - HCl systems.

All the potentials have their absolute minimum at the linear Rg·HX geometry. The Rg-H distance at the equilibrium geometry decreases considerably down the series Br-Cl-F, and even for HBr complexes the Rg-H distances are much less than in the rare gas - H_2 series.

Further experimental data are required before the intermolecular potentials for the rare gas - HF systems can be determined reliably over a wider region of configuration space. Particularly useful would be spectroscopic measurements of excited van der Waals bending states, and measurements of far infrared linewidths and second virial coefficients for rare gas + HF mixtures. Predictions of the results of these experiments have been made, based on the current best fit potentials.

REFERENCES

1. S.J. Harris, S.E. Novick and W. Klemperer, J. chem. Phys. 60, 3208 (1974); T.A. Dixon, C.H. Joyner, F.A. Baiocchi and W. Klemperer, J. chem. Phys. 74, 6539 (1981).

2. M.R. Keenan, L.W. Buxton, T.J. Balle and W.H. Flygare, J. chem. Phys. 74, 2133 (1981).

3. L.W. Buxton, E.J. Campbell, M.R. Keenan, T.J. Balle and W.H. Flygare, Chem. Phys. 54, 173 (1981).

4. F.A. Baiocchi, T.A. Dixon, C.H. Joyner and W. Klemperer, J. chem. Phys. in press.

5. K.C. Jackson, P.R.R. Langridge-Smith and B.J. Howard, Molec. Phys. 39, 817 (1980).

6. M.R. Keenan, E.J. Campbell, T.J. Balle, L.W. Buxton, T.K. Minton, P.D. Soper and W.H. Flygare, J. chem. Phys. 72, 3070 (1980).

7. J.A. Barnes, M. Keil, R.E. Kutina and J.C. Polanyi, J. chem. Phys. 72, 6306 (1980).

8. G.A. Parker, R.L. Snow and R.T. Pack, unpublished work (1975); W. Kołos, G. Corongiu and E. Clementi, Int. J. quant. Chem. 17, 775 (1980).

9. C.H. Becker, P.W. Tiedemann, J.J. Valentini and Y.T. Lee, J. chem. Phys. 71, 481 (1979).

10. R.F.W. Bader, I. Keaveny and P.E. Cade, J. chem. Phys. 47, 3381 (1967).

11. M. Shapiro, J. chem. Phys. 56, 2582 (1972); M. Shapiro and G.G. Balint-Kurti, J. chem. Phys. 71, 1461 (1979).

12. I.F. Kidd, G.G. Balint-Kurti and M. Shapiro, Faraday Discus. R. Soc. Chem. 71/22 (1981).

CHAPTER 6

ORIGIN OF THE INTERMOLECULAR FORCES

CHAPTER 6

ORIGIN OF THE INTERMOLECULAR FORCES

Attractive intermolecular forces may contain contributions from electrostatic, induction and dispersion effects. Electrostatic forces occur only when neither of the molecules involved is spherically symmetric, and so do not contribute in atom-diatom systems. Induction and dispersion interactions may both be formulated as second order perturbation energies [1], and so necessarily lower the total energy of the system for interacting molecules in their ground states.

6.1 Induction forces

A molecule with a nonspherical charge distribution produces an electric field $\vec{F}$, which can induce multipole moments in nearby polarisable molecules; the induced dipole moment is generally the most important of these from the point of view of induction forces. For an atom of polarisability α, the induced dipole is given by

$$\vec{\mu}_{ind} = \alpha \vec{F} \tag{1}$$

and the associated energy of interaction by

$$E_{ind} = -\tfrac{1}{2} \vec{\mu}_{ind} \cdot \vec{F} = -\tfrac{1}{2} \alpha F^2 \tag{2}$$

The induction energy is conventionally calculated by expanding the charge distribution of each molecule as a multipole series, and then using these permanent multipole moments to calculate the electric field at the position of the other molecule. This approach works well for

intermolecular distances that are large compared to molecular dimensions, but may not converge quickly for intermolecular distances as small as those found in van der Waals molecules. Since only the first few multipole moments are known for most molecules, it is worthwhile to look for a more quickly convergent representation of the molecular charge distribution.

The charge distribution in a hydrogen halide molecule may be modelled semiempirically using a simple valence bond picture. The molecule can be regarded as being formed from a hydrogen atom ($1s^1$) and a halogen atom ($np_x^2 p_y^2 p_z^1$), with bonding principally due to overlap of hydrogen 1s and halogen np_z orbitals. The dipole moment is then due to transfer of electrons from H to the halogen, and can be represented by partial charges +q and -q centred on the hydrogen and halogen nuclei respectively.

This charge separation alone gives rise to a quadrupole moment smaller than the true quadrupole of the molecule. It is possible to reproduce both the dipole and quadrupole moments using a 3-charge model [2], but there is no real physical justification for placing a third charge on the molecular axis. The 3-charge models also tend to give unacceptably high values for the partial charges [3], and so have not been used in the present work. Physically, the large quadrupole moments of the hydrogen halide molecules arise because the electron distribution around the halogen is concentrated away from the molecular axis, since the halogen np_z orbital is not fully occupied. The remaining quadrupole moment is therefore most realistically modelled either by placing partial negative charges off-axis around the halogen, or by placing a point quadrupole at the halogen nucleus. The latter approach has been taken here, since it is geometrically simpler.

The "finite size" model used here for the charge distribution of a hydrogen halide molecule is thus as follows

1) The dipole moment is replaced by two point charges, $\pm q$, at the hydrogen and halogen nuclei. These are given by

$$q = \frac{\mu}{r_0} \tag{3}$$

where μ is the experimental dipole moment and r_0 is the bond length of the diatomic molecule.

2) The remainder of the quadrupole moment is represented by a point quadrupole Θ_{Hal} at the halogen nucleus. This is related to the total quadrupole moment (relative to the HX centre of mass) by

$$\Theta_{Hal} = \Theta_{tot} - q(r_1^2 - r_2^2) \tag{4}$$

where r_1 and r_2 are the distances of the hydrogen and halogen nuclei respectively from the centre of mass. The second term in equation (4) allows for the contribution to the quadrupole from the point charges.

The values of q and Θ_{Hal} required to reproduce μ and Θ_{tot} for HF, HCl and HBr are given in table 1.

Table 1. Parameters of "finite size" model

	μ/D	q/e	Θ_{tot}/DÅ	Θ_{Hal}/DÅ
HF	1.8262	0.411	2.6	1.08
HCl	1.1085	0.180	3.7	2.36
HBr	0.8266	0.121	4.0	2.85

The induced dipole moments and interaction energies obtained with this model for Ne·HF and Ne·HCl are compared with those of a conventional multipole model in table 2, for intermolecular distances approximately corresponding to the appropriate van der Waals distances. It may be seen that the multipole model gives induction energies which are much less anisotropic than those given by the "finite size" model, mainly because the partial charge on the hydrogen atom approaches much closer to the rare gas atom in the latter model. The "finite size" model is probably more realistic than the multipole model, although both neglect the effects of higher order multipoles and polarisabilities.

Table 2. Comparison of "finite size" and multipole models for induction effects. μ^{R}_{ind} is the projection of $\vec{\mu}_{ind}$ along the $\vec{R}$ axis.

		"finite size"		multipole	
R/pm	Θ	μ^{R}_{ind}/D	E_{ind}/cm^{-1}	μ^{R}_{ind}/D	E_{ind}/cm^{-1}
		Ne·HF			
320	0	0.082	-43.2	0.074	-34.4
320	30	0.058	-26.5	0.057	-24.0
320	60	0.015	-7.8	0.018	-8.6
320	90	-0.014	-3.8	-0.015	-4.5
320	120	-0.024	-3.9	-0.026	-4.5
320	150	-0.021	-2.9	-0.020	-2.5
320	180	-0.019	-2.2	-0.015	-1.4
		Ne·HCl			
380	0	0.042	-11.3	0.037	-8.7
380	30	0.028	-6.4	0.027	-5.7
380	60	0.004	-1.7	0.005	-1.8
380	90	-0.010	-1.0	-0.011	-1.1
380	120	-0.010	-0.6	-0.011	-0.7
380	150	-0.001	-0.1	-0.001	-0.2
380	180	0.003	-0.1	0.005	-0.2

The "finite size" model has been used to calculate induction energies for all the Rg·HX complexes at $R = R_m(\theta)$ and $\theta = 0^o$ and $\theta = 90^o$, and the results are given in table 3. It may be seen that the induction effect accounts for about 70% of the anisotropy in the HF complexes, but less than 40% of the anisotropy in HCl complexes. In HBr complexes the fraction is probably around 25%, but this is less well determined.

Table 3a. Induction energies at $\theta = 0^o$ and $R = R_m(0^o)$ for Rg·HX complexes, calculated using "finite size" model. All energies in wavenumbers

	Ne	Ar	Kr	Xe
HF	45.2	120.3	137.5	152.2
HCl	11.5	31.1	39.8	51.1
HBr	5.7	16.3	21.7	28.1

Table 3b. Induction energies as for table 3a, but at $\theta = 90^o$ and $R = R_m(90^o)$

	Ne	Ar	Kr	Xe
HF	3.5	10.0	12.4	14.4
HCl	1.2	3.4	4.2	5.7
HBr	0.9	2.6	3.2	4.4

6.2 Dispersion forces

The dispersion forces at short range are more difficult to model than the induction forces. For the weakly anisotropic rare gas - H_2 complexes, Tang and Toennies [4] and Rodwell and Scoles [5] have

modelled the dispersion forces using a single centre expansion about the diatom centre of mass, whereas for interactions between large organic molecules it is clear that a many centre approach is required. The rare gas - hydrogen halide systems considered here fall between these two limits. Atom-centred site-site potentials have been extensively used in computer simulations of condensed phases involving nonspherical molecules, and it is interesting to investigate to what extent such a model is valid for the rare gas - hydrogen halide systems.

Two objections to site-site models can be raised immediately:

1) If an atom-diatom potential is modelled using pure site-site potentials (eg. as the sum of two Lennard-Jones potentials centred on the nuclei of the diatom) the equilibrium geometry is necessarily nonlinear, since the attractive parts of the two potentials can then reinforce one another most effectively. However, nonlinear equilibrium geometries are often not found experimentally, even for nonpolar diatomic molecules: in $Ar \cdot H_2$, for example, the equilibrium geometry is linear, not T-shaped as predicted by a site-site model.
2) A site-site potential is anisotropic in the well region, but becomes completely isotropic in the limit of large intermolecular distance. This is not the correct behaviour: in $Ar \cdot H_2$, the long range C_6 coefficients for parallel and perpendicular approaches of Ar to H_2 differ by more than 15% [6].

The first objection above applies only if both the attractive and the repulsive forces are modelled using site-site potentials; if the repulsive forces are allowed to be less anisotropic than predicted by a site-site model, the experimental observation of linear equilibrium geometries can be accommodated while maintaining site-site dispersion forces. However, the second objection should be remembered as

illustrating the limitations of site-site models.

In a site-site model, the potentials for the rare gas - hydrogen halide systems may be decomposed

$$V(R,\theta) = V_X(R_X) + V_H(R_H) + V_{ind}(R,\theta)$$

where V_X and V_H are one dimensional potential functions centred on the X and H atoms, R_X and R_H are the corresponding atom-atom distances, and $V_{ind}(R,\theta)$ is the induction contribution to the potential. If $V_X(R_X)$ and $V_H(R_H)$ are represented by Maitland-Smith potentials, their parameters may be adjusted to reproduce the "experimental" $\varepsilon(\theta)$ and $R_m(\theta)$ at $\theta = 0^o$ and 90^o. The parameters ε_X, R_{mX}, ε_H and R_{mH} obtained in this way are shown in table 4. This representation of the potential is useful for investigating the origin of the attractive intermolecular forces, but it should be remembered that it may not be adequate at angles other than $\theta = 0^o$ and 90^o if the repulsive forces are not well represented by a site-site model.

Table 4. Parameters of site-site potentials fitted to "experimental" potentials at $\theta = 0^o$ and 90^o

	Ne·HCl	Ar·HCl	Kr·HCl	Xe·HCl	Ar·HF	Kr·HF	Xe·HF
ε_X/cm^{-1}	36.3	90.9	102.6	113.6	41.5	46.3	42.6
R_{mX}/pm	371	393	406	423	359	372	398
$C_{6X}/10^{17}cm^{-1}pm^6$	0.94	3.36	4.57	6.49	0.89	1.22	1.69
ε_H/cm^{-1}	22.3	65.5	77.6	109.5	70.1	80.6	130.1
R_{mH}/pm	262	287	296	312	265	279	295
$C_{6H}/10^{17}cm^{-1}pm^6$	0.07	0.37	0.52	1.02	0.24	0.38	0.85
$C_{6H}(H_2)/10^{17}cm^{-1}pm^6$	0.20	0.68	0.96	1.44	0.68	0.96	1.44

As discussed above, the potentials $V_X(R_X)$ are similar to those for the isoelectronic rare gas - rare gas interactions. It is clearly unrealistic to expect $V_H(R_H)$ to be the same as for the corresponding rare gas - hyrogen atom potential, but it might be expected that it could be related to the rare gas - H_2 interactions, which are the simplest comparable systems containing bonded hydrogen atoms. It has already been remarked (sections 4.6.1 and 5.4) that the values of r_H (and hence R_{mH}) are much smaller in the rare gas - hydrogen halides than in the rare gas - H_2 systems, indicating that the repulsive forces centred on hydrogen are weaker in the hydrogen halide systems. It may be seen from table 4 that values of C_{6H} obtained from the expression

$$C_{6H} = \varepsilon_H R_{mH}^6$$

are also considerably lower than the corresponding quantities for the rare gas - H_2 systems. Thus it appears that both the attractive and the repulsive forces centred on hydrogen are significantly reduced in rare gas - hydrogen halide systems as compared to the rare gas - H_2 systems. Both these effects may be attributed to withdrawal of electrons from hydrogen by the more electronegative halogen atom, but a detailed formulation of dispersion forces in a site-site representation is necessary before more quantitative conclusions can be obtained.

6.3 Conclusion

Both induction and dispersion forces make important contributions to the intermolecular forces in rare gas - hydrogen halide systems, and it seems likely that the attractive forces can be adequately explained

in terms of these forces alone. There is no experimental evidence for Klemperer's suggestion that incipient chemical bonding is important [7], and this is supported by the lack of bonding at the SCF level in ab initio calculations on Ar·HCl [8].

The results obtained here highlight deficiencies in some commonly used representations of intermolecular forces. The conventional representation in terms of an expansion in Legendre polynomials about the molecular centre of mass is not adequate even in these small systems, since the expansion converges very slowly in the region of the minimum. The dispersion forces near the minimum can be quite accurately modelled using additive site-site potentials based on the atomic positions, but the angular position of the absolute minimum cannot be correctly reproduced if the repulsive forces are also represented in this way.

Semiempirical methods which treat the dispersion energy as a series in Legendre polynomials [4,5] are thus unlikely to be adequate for the rare gas - hydrogen halide systems, and single centre expansions will certainly break down for systems involving larger molecules. It may prove possible to model the dispersion forces using an additive site-site representation, but in its simplest form such a model would give intermolecular potentials that were too isotropic at very long range. One way around this problem for atom-diatom systems would be to formulate dispersion forces explicitly in a two centre representation, although the extension of such a formulation to polyatomic systems would be very difficult.

REFERENCES

1. A.D. Buckingham, Adv. chem. Phys. 12, 107 (1967).

2. J.T. Brobjer and J.N. Murrell, Chem. Phys. Lett. 77, 601 (1981).

3. I.R. McDonald, S.F. O'Shea, D.G. Bounds and M.L. Klein, J. chem. Phys. 72, 5710 (1980).

4. K.T. Tang and J.P. Toennies, J. chem. Phys. 68, 5501 (1978); J. chem. Phys. 74, 1148 (1981).

5. W.R. Rodwell and G. Scoles, J. chem. Phys. to be published.

6. P.W. Langhoff, R.G. Gordon and M. Karplus, J. chem. Phys. 55, 2126 (1971).

7. W. Klemperer, Faraday Discus. Chem. Soc. 62, 309 (1977).

8. J.A. Vliegenthart and A. Rozendaal, private communcation.

APPENDIX 1

DIRECT SOLUTION OF

PERTURBATION EQUATIONS

APPENDIX 1

DIRECT SOLUTION OF PERTURBATION EQUATIONS

Many molecular properties are most conveniently calculated by perturbation theory, starting from an appropriate zeroth order solution. In such cases, the total hamiltonian is partitioned

$$\hat{H} = \hat{H}^{(0)} + \lambda \hat{H}' \tag{1}$$

and the total wavefunction and energy are expanded as power series in the scale parameter λ

$$\psi = \sum_{k=0}^{\infty} \lambda^k \psi^{(k)} \tag{2}$$

$$E = \sum_{k=0}^{\infty} \lambda^k E^{(k)} \quad . \tag{3}$$

Substituting these equations into the total Schrödinger equation and collection powers of λ yields equations for the wavefunction corrections

$$\left[\hat{H}^{(0)} - E^{(0)}\right] \psi^{(1)} = \left[E^{(1)} - \hat{H}'\right] \psi^{(0)} \tag{4}$$

$$\left[\hat{H}^{(0)} - E^{(0)}\right] \psi^{(2)} = \left[E^{(1)} - \hat{H}'\right] \psi^{(1)} + E^{(2)}\psi^{(0)} \quad . \tag{5}$$

In the usual formulation of perturbation theory, these equations are solved by expanding the $\{\psi^{(k)}\}$ in terms of the zeroth order eigenfunctions

$$\psi^{(k)} = \sum_{n} c_n^{(k)} \psi_n^{(0)} \tag{6}$$

yielding the well known expression for the first order correction to the

wavefunction

$$\psi^{(1)} = \sum_n \psi_n^{(0)} \frac{\langle n|\hat{H}' - E^{(1)}|0\rangle}{E^{(0)} - E_n^{(0)}} \qquad (7)$$

This approach is often successful for rotational problems, where the spacing between successive excited states increases with increasing energy, so that the basis set expansion converges rapidly. In cases involving stretching wavefunctions, however, there may be difficulties. If the zeroth order wavefunctions are solutions for a realistic potential with a dissociation limit, the basis functions are very closely spaced near the limit, and the summation of equation (7) may converge slowly. It is sometimes also necessary to include contributions from continuum levels, and this is likely to be numerically inaccurate.

Under these circumstances it is possible to avoid the basis set expansion altogether, and to solve equations (4) and (5) directly. Two distinct cases may be identified: the states being mixed in by the perturbation may be eigenfunctions either of the same effective hamiltonian as $\psi^{(0)}$ (i.e. involving the same potential curve) or of a different effective hamiltonian (i.e. perturbation off-diagonal in Born-Oppenheimer bending state, so that a different potential curve is involved). In the former case, $\hat{H}'$ and the $\{\psi^{(k)}\}$ are functions of R only, and $\hat{H}^{(0)}$ in equations (4) and (5) may be replaced by its explicit form

$$\hat{H}^{(0)} = -\frac{\hbar^2}{2\mu}\frac{d^2}{dR^2} + U(R) \qquad (8)$$

to give inhomogeneous differential equations

$$\left[-\frac{\hbar^2}{2\mu}\frac{d^2}{dR^2} + U(R) - E^{(0)}\right]\psi^{(1)}(R) = \left[E^{(1)} - \hat{H}'(R)\right]\psi^{(0)}(R) \qquad (9)$$

$$\left[-\frac{\hbar^2}{2\mu}\frac{d^2}{dR^2} + U(R) - E^{(0)}\right]\psi^{(2)}(R) = \left[E^{(1)} - H'(R)\right]\psi^{(1)}(R) + E^{(2)}\psi^{(0)}(R)\,. \qquad (10)$$

These equations may be solved for $\psi^{(1)}(R)$ and $\psi^{(2)}(R)$ using the numerical method described below. Corrections to the energy may then be calculated by one dimensional numerical integration

$$E^{(2)} = \int \psi^{(0)}(R)\left[\hat{H}'(R) - E^{(1)}\right]\psi^{(1)}(R)\,dR \qquad (11)$$

$$E^{(3)} = \int \psi^{(1)}(R)\left[\hat{H}'(R) - E^{(1)}\right]\psi^{(1)}(R)\,dR\,. \qquad (12)$$

Corrections to expectation values are also simply obtained.

This method is mathematically equivalent to the usual sum-over-states procedure. The wavefunction corrections $\{\psi^{(k)}\}$ are simply functions of R which contain contributions from all excited stretching states, so that the problem of basis set convergence is avoided.

The second case mentioned above, where the states being mixed in are eigenfunctions of a different effective zeroth order Hamiltonian, corresponds physically to breakdown of the Born-Oppenheimer approximation. The zeroth order wavefunction is written as a single product function

$$\psi_{bs}^{(0)} = \phi_b(\theta;R)\,\chi_{bs}^{(0)}(R) \qquad (13)$$

where two quantum numbers b and s have been introduced for the zeroth

order states, $\phi_b(\theta;R)$ is the bending wavefunction depending parametrically upon R, and $\chi^{(0)}_{bs}(R)$ is the stretching wavefunction. The wavefunction corrections $\{\psi^{(k)}\}$ are also expanded in terms of the bending functions

$$\psi^{(k)}_{bs} = \sum_{b'} \phi_{b'}(\theta;R)\ \chi^{(k)}_{bs;b'}(R) \tag{14}$$

This equation may be substituted into equations (4) and (5) and projected onto $\phi_{b''}(\theta;R)$ to give inhomogeneous differential equations for the functions $\{\chi^{(k)}_{bs;b''}(R)\}$. For the diagonal case $b = b''$ these are identical in form to equations (9) and (10). For $b \neq b''$, they are

$$\left[-\frac{\hbar^2}{2\mu}\frac{d^2}{dR^2} + U_{b''}(R) - E^{(0)}_{bs}\right] \chi^{(1)}_{bs;b''}(R) = -H'_{b''b}(R)\ \chi^{(0)}_{bs} \tag{15}$$

$$\left[-\frac{\hbar^2}{2\mu}\frac{d^2}{dR^2} + U_{b''}(R) - E^{(0)}_{bs}\right] \chi^{(2)}_{bs;b''}(R) = \sum_{b'} \left[E^{(1)}_{bs}\delta_{b''b'} - H'_{b''b'}(R)\right] \chi^{(1)}_{bs;b'}(R) \tag{16}$$

where $H'_{ab}(R) = \int \phi^*_a(\theta;R)\ \hat{H}'\ \phi_b(\theta;R)\ \sin\theta\ d\theta$.

These equations can then be solved for each bending state mixed in by the perturbation H'. The corrections to the energy are given by

$$E^{(2)}_{bs} = \sum_{b'} \chi^{(0)}_{bs}(R) \left[H'_{bb'}(R) - E^{(1)}_{bs}\delta_{bb'}\right] \chi^{(1)}_{bs;b'}(R)\ dR \tag{17}$$

$$E^{(3)}_{bs} = \sum_{b'b''} \chi^{(1)}_{bs;b'}(R) \left[H'_{b'b''}(R) - E^{(1)}_{bs}\delta_{b'b''}\right] \chi^{(1)}_{bs;b''}(R)\ dR\ . \tag{18}$$

These may again be evaluated by one dimensional integration, and involve

no summations over excited stretching states. The summations over bending states usually converge rapidly in problems concerning the dynamics of van der Waals molecules.

Numerical solution

The present treatment yields differential equations for the wavefunction corrections $\{\psi^{(k)}\}$. These are linear inhomogeneous differential equations of the form

$$\frac{d^2\chi}{dR^2} = V(R)\chi(R) + g(R) , \tag{19}$$

where $\chi(R)$ is the wavefunction correction to be calculated, and $g(R)$ and $V(R)$ are known functions.

The function $V(R)$ has the shape of a potential well, and $g(R)$ goes to zero as $R \to 0$ or ∞ . The equation is a boundary value problem since, if the total wavefunction is to be quadratically integrable, so too must be the perturbation corrections. Equation (19) is not an eigenvalue problem. In numerical applications, $V(R)$ and $g(R)$ are usually specified numerically as a grid of R values, and it is in this form that equation (19) is most conveniently solved.

If $V(R)$ and $g(R)$ are specified at points $R_1 \ldots R_1 \ldots R_n$, with corresponding values denoted by V_i and g_i, equation (19) may be replaced by a finite-difference approximation at each i. If h is the radial interval between successive mesh points and bracketed superscripts now represent radial differentiation, χ may be expanded about χ_i

$$\chi_{i-1} + \chi_{i+1} = \sum_{k=0}^{\infty} \frac{2h^{2k}}{(2k)!} \chi_i^{(2k)}$$

$$= 2\chi_i + h^2 \chi_i^{(2)} + \frac{h^4}{12} \chi_i^{(4)} + \cdots . \qquad (20)$$

The simplest form of solution is obtained by dropping all terms after h^2 in this equation. A better approximation, analogous to Numerov integration [1] gives a solution accurate to order h^4, and is described here. First, a set of values Y_i are defined in terms of the χ_i

$$Y_i = \chi_i - \frac{h^2}{12} \chi_i^{(2)} = \chi_i \left[1 - \frac{h^2}{12} V_i\right] - \frac{h^2}{12} g_i . \qquad (21)$$

The second part of this equation is obtained by substituting for $\chi_i^{(2)}$ from equation (19). With this choice of Y_i, equation (20) may be written

$$Y_{i-1} - 2Y_i + Y_{i+1} = h^2 \chi_i^{(2)}$$

$$= h^2 V_i \chi_i + h^2 g_i$$

$$= (V_i Y_i + g_i) \cdot h^2 \Big/ \left[1 - \frac{h^2}{12} V_i\right] \qquad (22)$$

while the boundary conditions may be imposed by setting $Y_0 = Y_{n+1} = 0$. Thus the differential equation reduces to a set of n simultaneous equations for the Y_i, which may be written in matrix form

$$\underline{AY} = \underline{G} , \qquad (23)$$

where $\underline{A}$ is an $n \times n$ tridiagonal matrix with all subdiagonal and superdiagonal matrix elements equal to unity, $\underline{Y}$ is the column vector of the Y_i

and G is the solution vector from the right-hand side of (22)

$$A_{ii} = -2 - h^2 V_i \Big/ \left(1 - \frac{h}{12} V_i\right) , \tag{24}$$

$$G_i = h^2 g_i \Big/ \left(1 - \frac{h^2}{12} V_i\right) . \tag{25}$$

The solution of such a system of equations by Gaussian elimination is computationally simple [2]. Iterative methods are not necessary, and the computer time taken is only directly proportional to n.

This simple procedure is numerically stable only if $E_{bs}^{(0)}$ is not an eigenvalue of the hamiltonian involving $U_{b'}(R)$; this is generally the case for perturbations off-diagonal in bending state, $b \neq b'$. For $b = b'$, however, there exists a solution of the homogeneous equation

$$\frac{d^2\chi}{dR^2} = V(R)\ \chi(R) \tag{26}$$

since this is just the zeroth order Schrödinger equation. The general solution of equation (19) thus contains an arbitrary component proportional to $\chi^{(0)}(R)$. However, the sixe of this component does not affect the calculated values of observables, so that it is convenient to choose $\chi(R)$ to be orthogonal to $\chi^{(0)}(R)$. This is sufficient to ensure that equation (19) has a unique solution, and has the same effect as excluding the state being perturbed from the summation in the usual formulation of perturbation theory.

Computationally, the orthogonality constraint is applied during the process of Gaussian elimination for the tridiagonal matrix. Orthogonality of $\chi(R)$ and $\chi^{(0)}(R)$ requires that

$$\sum_i \chi_i \chi_i^{(0)} = 0 = \sum_i \left[Y_i + \frac{h^2}{12} g_i \right] \chi_i^{(0)} \Big/ \left[1 - \frac{h^2}{12} V_i \right] \qquad (27)$$

Instead of simply eliminating all subdiagonal elements from the matrix $\underline{A}$, and then propagating $\underline{Y}$ backwards from R_n to R_1, a matching point R_{mid} is chosen at which the zeroth order wavefunction $\chi^{(0)}$ is non-zero. The subdiagonal elements of $\underline{A}$ are first eliminated from R_1 to R_{mid}, and the superdiagonal elements from R_n to R_{mid+1}. Equation (23) thus supplies one equation relating Y_{mid} to Y_{mid+1}, and the orthogonality condition (27) supplies a second; these two simultaneous equations may then be solved for Y_{mid} and Y_{mid+1}. Finally, the solution vector $\underline{Y}$ is propagated from R_{mid} to R_1 and R_n, and then transformed back to give the desired solution χ.

This algorithm is in principle unstable in the classically forbidden region, since it involves propagating the function $\underline{Y}$ along a path where $\underline{Y}$ is exponentially decreasing. There is thus a possibility that a spurious exponentially increasing component will develop and will quickly dominate the true decreasing function. This condition is easily detected since the true solution is always monotonically decreasing when propagated far into a classically forbidden region. If the function $\underline{Y}$ starts to increase again, it is simply set to zero beyond the point where the instability appears. There is very little contribution to any observable quantity from this region, so that this procedure does not introduce any significant error.

The method described above is not valid for calculating the effect of a perturbing state whose dissociation limit is below the state of interest (i.e. if predissociation is possible). This is because there will always exist a continuum level of the lower state which is

degenerate with the level being investigated, so that equation (19) will again not have a unique solution.

In addition to the applications described in this thesis, the differential equation method has been applied to a number of problems involving more strongly bound molecules. The formalism used is identical, except that the bending functions used above are replaced by electronic functions, and integration over angles is replaced by integration over electronic coordinates. The method has been applied to nonadiabatic effects in H_2^+ [3], and to centrifugal distortion constants [4] and Λ-doubling constants [5,6] in diatomic molecules. Numerical comparisons with the conventional method of summing over vibrational states have been given in references 3-5; agreement was essentially exact in cases where the sum-over-states results were converged.

References

1. B. Numerov, Publs. observatoire central astrophys. Russ., Vol. 2 (1933).

2. S.D. Conte and C. de Boor, Elementary Numerical Analysis, McGraw-Hill (1972), p. 122.

3. J.M. Hutson and B.J. Howard, Molec. Phys. 41, 1113 (1980).

4. J.M. Hutson, J. Phys. B 14, 851 (1981).

5. J.M. Hutson and D.L. Cooper, J. chem. Phys., in press.

6. K.C. Checkland, D.L. Cooper and W.G. Richards, J. Phys. B., in press.

APPENDIX 2

PROPERTIES OF RARE GAS ATOMS AND HYDROGEN HALIDE MOLECULES

APPENDIX 2

Maitland-Smith potentials for rare gas pairs [1]

Well depths/cm^{-1}

Ne	30.2			
Ar	46.6	98.8		
Kr	49.9	114.7	138.4	
Xe	51.8	130.2	160.6	191.3
	Ne	Ar	Kr	Xe

Equilibrium distances/pm

Ne	310			
Ar	343	376		
Kr	358	388	402	
Xe	375	406	418	436
	Ne	Ar	Kr	Xe

C_6 coefficients for rare gas pairs/$10^{17} cm^{-1} pm^6$ [2]

Ne	0.32			
Ar	0.99	3.26		
Kr	1.36	4.56	6.41	
Xe	2.02	6.84	9.59	14.51
	Ne	Ar	Kr	Xe

Spectroscopic constants of hydrogen halides (v= 0)

	b/cm^{-1}	eQq^{Hal}/MHz	eQq^{D}/kHz	d/kHz	μ/Debye
HF	20.55974			143.375	1.82618
DF	10.86034		354.238	22.170	1.81881
$H^{35}Cl$	10.44019	-67.61893	-	5.59	1.1085
$H^{37}Cl$	10.42452	-53.436	-	4.65	...
$D^{35}Cl$	5.39227	-67.39338	187.36	0.85	1.1033
$D^{37}Cl$	5.37649	-53.073	...	...	...
$H^{79}Br$	8.35106	532.30590	-	10.296	0.82657
$H^{81}Br$	8.34846	444.68066	-	11.138	0.82654
$D^{79}Br$	4.24819	530.6315	146.9	1.59	0.8235
$D^{81}Br$	4.24560	443.2799	146.1	1.74	0.8233

Structural constants of hydrogen halides

	mass	reduced mass	r_0/pm	X-cm distance/pm
HF	20.00027	0.95704	92.560	4.664
DF	21.00654	1.82099	92.326	8.852
$H^{35}Cl$	35.97667	0.97959	128.387	3.597
$H^{37}Cl$	37.97372	0.98108	128.386	3.407
$D^{35}Cl$	36.98295	1.90441	128.124	6.978
$D^{37}Cl$	38.98000	1.91003	128.123	6.620
$H^{79}Br$	79.92616	0.99512	142.426	1.796
$H^{81}Br$	81.92412	0.99543	142.426	1.752
$D^{79}Br$	80.93243	1.96398	142.144	3.537
$D^{81}Br$	82.93039	1.96519	142.144	3.452

REFERENCES

1. J.J.H. van den Biesen, F.A. Stokvis, E.H. van Veen and C.J.N. van den Meijdenberg, Physica 100 A, 375 (1980).

2. G. Starkschall and R.G. Gordon, J. chem. Phys. 54, 663 (1971).